RECORD COPY
c.1

TL0025524

SANDIA NATIONAL
LABORATORIES
TECHNICAL LIBRARY

SANDIA REPORT

SAND98–0387 • UC–704
Unlimited Release
Printed March 1998

Impact Failure and Fragmentation Properties of Metals

D. E. Grady, M. E. Kipp

Prepared by
Sandia National Laboratories
Albuquerque, New Mexico 87185 and Livermore, California 94550

Sandia is a multiprogram laboratory operated by Sandia Corporation, a Lockheed Martin Company, for the United States Department of Energy under Contract DE-AC04-94AL85000.

Approved for public release; further dissemination unlimited.

Sandia National Laboratories

126 p.

Issued by Sandia National Laboratories, operated for the United States Department of Energy by Sandia Corporation.

NOTICE: This report was prepared as an account of work sponsored by an agency of the United States Government. Neither the United States Government nor any agency thereof, nor any of their employees, nor any of their contractors, subcontractors, or their employees, makes any warranty, express or implied, or assumes any legal liability or responsibility for the accuracy, completeness, or usefulness of any information, apparatus, product, or process disclosed, or represents that its use would not infringe privately owned rights. Reference herein to any specific commercial product, process, or service by trade name, trademark, manufacturer, or otherwise, does not necessarily constitute or imply its endorsement, recommendation, or favoring by the United States Government, any agency thereof, or any of their contractors or subcontractors. The views and opinions expressed herein do not necessarily state or reflect those of the United States Government, any agency thereof, or any of their contractors.

Printed in the United States of America. This report has been reproduced directly from the best available copy.

Available to DOE and DOE contractors from
Office of Scientific and Technical Information
P.O. Box 62
Oak Ridge, TN 37831

Prices available from (615) 576-8401, FTS 626-8401

Available to the public from
National Technical Information Service
U.S. Department of Commerce
5285 Port Royal Rd
Springfield, VA 22161

NTIS price codes
Printed copy: A07
Microfiche copy: A01

SAND98-0387
Unlimited Release
Printed March 1998

Distribution
Category UC-704

Impact Failure and Fragmentation Properties of Metals

D. E. Grady
Applied Research Associates
Albuquerque, NM 87110

M. E. Kipp
Computational Physics Department
Sandia National Laboratories
P. O. Box 5800
Albuquerque, NM 87185-0820

Abstract

In the present study we describe the development of an experimental fracture material property test method specific to dynamic fragmentation. Spherical test samples of the metals of interest are subjected to controlled impulsive stress loads by acceleration to high velocities with a light-gas launcher facility and subsequent normal impact on thin plates. Motion, deformation and fragmentation of the test samples are diagnosed with multiple flash radiography methods. The impact plate materials are selected to be transparent to the x-ray method so that only test metal material is imaged. Through a systematic series of such tests both strain-to-failure and fragmentation resistance properties are determined through this experimental method. Fragmentation property data for several steels, copper, aluminum, tantalum and titanium have been obtained to date. Aspects of the dynamic data have been analyzed with computational methods to achieve a better understanding of the processes leading to failure and fragmentation, and to test an existing computational fragmentation model.

Acknowledgments

The authors would like to thank Bill Reinhart, Clint Hall and Ron Moody for performing the experiments represented in this study. A less extensive open literature version of this report has been published in the Journal of Impact Engineering with the Proceedings of the 1996 Hypervelocity Impact Symposium held in Freiburg, Germany.

Contents

Acknowledgments.....5
Contents.....7
1. Introduction and Summary.....9
2. Experimental Methods and Configuration.....11
3. Experimental Test Results.....15
4. Analysis.....33
5. Numerical Investigation.....47
6. Discussion.....53
7. References.....55
8. APPENDIX A- Summary of Fragmentation Theory.....59
9. APPENDIX B - Summary of Material Parameters.....65
10. APPENDIX C - Radiographic Records.....67

1 INTRODUCTION AND SUMMARY.

Some basic theories have emerged within the past 10 years for predicting the consequences of dynamic fragmentation brought about by high-velocity impact or explosive events. These theories have focused principally on the prediction of mean fragment size through energy and momentum balance principles (*e.g.* Grady, 1982; Kipp and Grady, 1985; Glenn and Chudnovsky, 1986; Grady, 1988), and on the statistical issues of fragment size distributions (*e.g.* Englman, *et al.*, 1984; Grady and Kipp, 1985; Brown, 1989; Grady, 1990). These theoretical bases are providing the underlying framework for a number of computational algorithms employed to analyze complex fragmentation events (*e.g.* Johnson, *et al.*, 1990; Melosh, *et al.*, 1992; Kipp, *et al.*, 1993a, 1993b).

There are, nonetheless, a number of unresolved issues within the development of statistical energy-balance theories of fragmentation. And there is a pressing need for high-resolution experimental data focused on the validation of these theories. Furthermore, implementation and validation of these theories in numerical wave propagation codes is needed so that extensions can be made to the investigation of dynamic fragmentation in complex large scale catastrophic events.

A critical issue is a need for failure and fragmentation material property data for solids of interest which characterize material behavior under intense stress-wave loading. Although static fracture data frequently exist for these materials, the current state of theoretical understanding does not provide for the confident extension of these static data into the highly dynamic regime.

In the present study we explored the possibilities of using a newly developed impact fracture and fragmentation experiment to determine dynamic failure and fragmentation properties of metals. A sample of the test material is prepared in the form of a solid sphere and launched using a light-gas gun facility. The test sphere is caused to impact a thin plate of low-density non-metallic material and to undergo catastrophic fragmentation. Flash radiography is used to image the fragmented specimen at several stations. Only the metal debris is imaged on the radiograph because of the low density of the impact plate material. From the extent of fragmentation and the velocity of debris expansion, analytic theories of the shock and fragmentation processes are pursued through which fragmentation properties of the metal are inferred. These properties include measures of the strain or deformation to failure, the energy absorbed before onset of fragmentation and the resistance or toughness of the material to fragmentation. In subsequent sections exploratory studies and the development of this work are described. Numerical analysis is used to complement and to support interpretation of the experiments. These numerical analyses also enable an existing computational fragmentation theory to be evaluated including the material parameters that are used in this theory.

2 EXPERIMENTAL METHODS AND CONFIGURATION.

2.1 Test Objectives.

In the present material property test method a sample of the metal of interest is prepared as a solid sphere. By methods to be described, the sample is subjected to a controlled impulsive load as suggested in Figure 2.1. Interest is in the mechanical response of the sample. Plastic deformation, failure and the intensity of fragmentation are features of the responses monitored within a test series.

Under modest impulsive loads the spherical sample is deformed but failure and subsequent fragmentation do not occur. By observing deformation over several tests up to the failure state a measure of the strain-to-failure for the material of interest is achieved. This distortion of the test sample is indicated in the left of Figure 2.2.

For impulsive loads which exceed the breakup threshold of the test sample, fragmentation and expansion of the resulting debris occurs as illustrated on the right in Figure 2.2. Fragment debris expansion characteristics are exploited to establish input energy levels needed to achieve failure and breakup. Statistical size characteristics are used to determine dynamic fracture resistance properties of the material.

2.2 Experimental Configuration and Parameters.

The experimental configuration for investigating the fragmentation properties of metals is shown in Figure 2.3. Solid metal spheres mounted in lexan sabots were launched at velocities between about 3 to 5 km/s with a two-stage light-gas gun system. The diameter of the launch tube used was 12 mm. Plastic sabots were separated from the metal spheres through forces produced by a rarefied atmosphere in the gun range section. Sabot segments were trapped upstream and did not reach the target impact chamber. Velocity of the

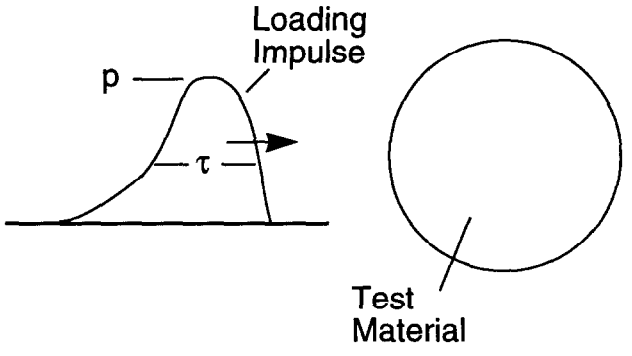

Figure 2.1 Concept for dynamic failure and fragmentation properties test.

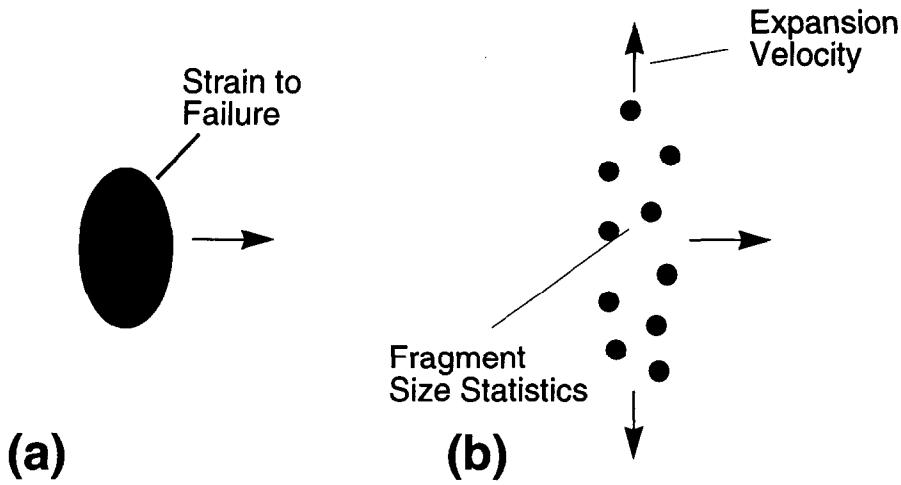

Figure 2.2 Experimental observables in radiographs of sphere-on-plate impact tests. (a) Impact velocity below breakup threshold. (b) Impact velocity above breakup threshold.

metal spheres was measured to ±1% accuracy by recording the time interval during passage between two magnetic coils of known separation. Normal impact occurred in the target chamber at the center of a thin stationary plate. In a number of the tests conducted this plate was a 75 mm by 75 mm square of PMMA (polymethyl-methacrylate) Rohm and Haas Type II UVA (density 1186 kg/m^3). In other tests where more intense impulsive loads were required similar thickness glass (GE dynasil 1000, density 2201 kg/m^3) or aluminum oxide (GE lucolax, density 3969 kg/m^3) were used as plate materials.

In all tests metal spheres approximately 6.35 mm (1/4 inch) in diameter were used as the test samples. The specific materials and initial properties are detailed later in the present section.

2.3 Radiographic Techniques.

Deformed sample spheres or fragment debris were imaged at two stations (approximately 150 mm and 300 mm) downstream from the impact position. Two 150 keV flash x-ray tubes provided shadow-graphs of the fragment debris, as shown schematically in Figure 2.3. Appropriate delay times were calculated from the predicted impact velocity and the x-ray tubes were independently triggered from the second magnetic velocity coil. The x-ray film cassette, using Kodak Direct Exposure film backed by a Quanta Fast Detail screen, was stationed about 100 mm from the centerline of the debris trajectory. A representative test result performed on 304 stainless steel is shown in Figure 2.4. A shadow of the glass barrier plate is also observed in the first station radiograph. The fragment debris subsequently impacted an aluminum witness plate which provided in some cases an independent measure of particle size and velocity statistics (Kipp, 1994)

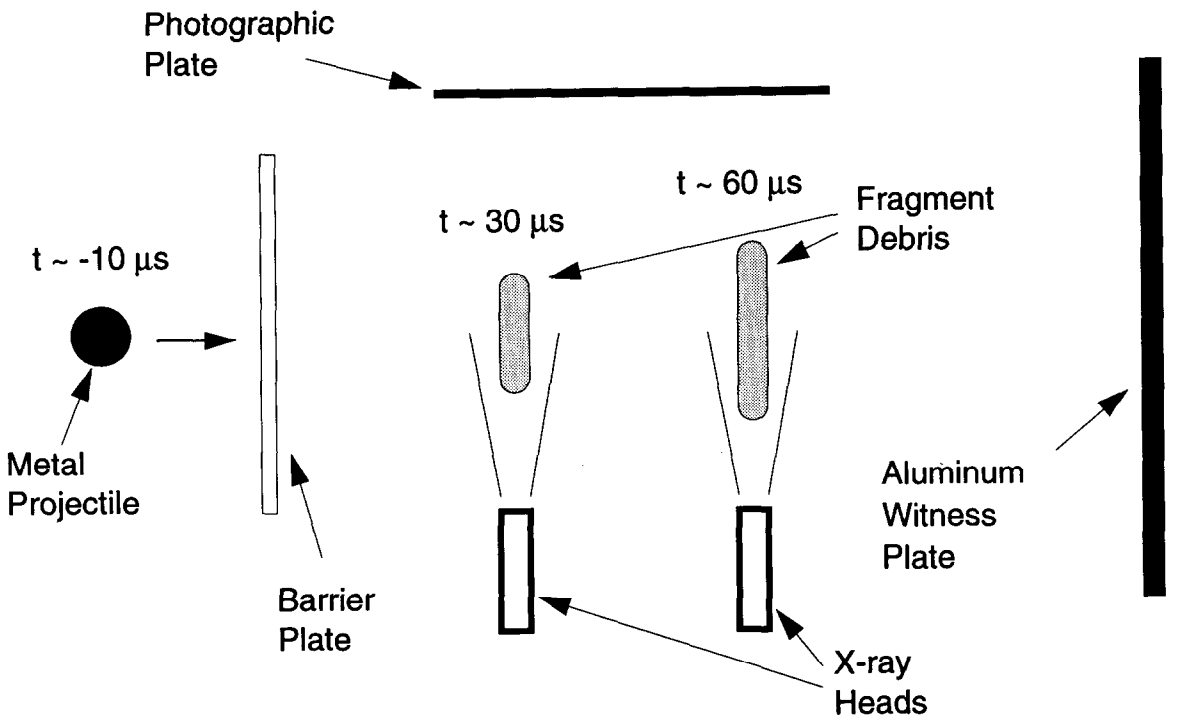

Figure 2.3 Experimental configuration for sphere-on-plate failure and fragmentation property tests.

2.4 Materials.

Elemental or alloyed metals from various sources were used in the present tests. Copper spheres were as-received OFHC material with a density of 8930 kg/m^3. Similarly, as-re-

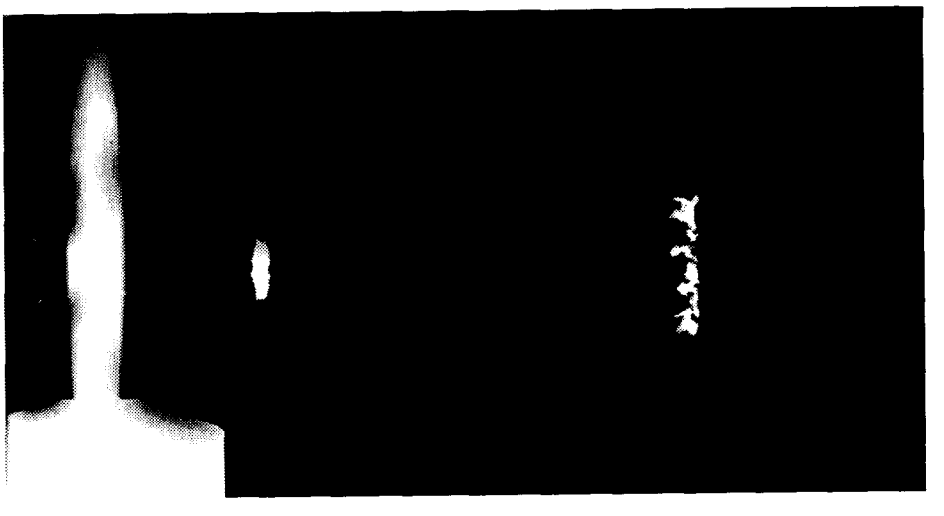

Figure 2.4 Example of radiographic images in test technique. Material is AISI Type 304 stainless steel.

ceived 7075-T6 aluminum spheres with a density of 2800 kg/m^3 were tested. Several steels were studied. One was an AISI Type 304 chromium-nickel stainless steel. AF1410 and D6AC steels were provided by Morris Dilmore, Wright Laboratory, Eglin AFB, and heat treatment on the sample spheres was performed by him. An unspecified steel extracted and prepared from 7.6 mm armor piercing projectiles was also tested. A pure tantalum material was provided by David Lassila, Lawrence Livermore National Laboratory; density of 16650 kg/m^3. Shock wave properties on this tantalum are reported by Furnish, *et al.* (1994). The titanium-6%Al-4%Va was provided by Lalit Chhabildas, Sandia National Laboratories; density of 4420 kg/m^3. Spall and fragmentation properties of this metal are reported by Chhabildas, *et al.* (1990).

3 EXPERIMENTAL TEST RESULTS.

Radiographic records resulting from the present study along with tabulated data and selected plots of fragment debris dynamics are discussed in the present section. Radiographs for all tests are found in an appendix of this report.

In the tables each test is identified. The plate material used is specified and the impact velocity selected to achieve a given level of impulsive stress load is provided. Distances d_1 and d_2 identify the position (approximate front of the sample or the debris disc) down stream from the impact plate corresponding to the first and second radiograph records, respectively. The time Δt identifies the delay between the exposures of the two radiographs. From these parameters the radial expansion velocity of the principal debris disc and the axial velocity of the debris front are calculated. The latter results are included in the tables and are also illustrated in the accompanying plots.

For subcritical impulsive loads fragmentation is not achieved. Instead, the sample projectile is observed to be significantly deformed from the initial spherical geometry after penetrating the barrier plate. An operational measure of the deformation strain is determined from the radiographic record and is included in the respective tables. This strain measure is $\varepsilon = 1 - l/2R$ where R is the initial sphere radius and l is the axial dimension of the distorted sample. Although some thickening of this dimension in the radiographic record might be expected due to sample rotation, the small amount of rotation observed plus the curvature of the surfaces is expected to make this uncertainty tolerably small. Also it should be recognized that some degree of internal cracking or void growth may compromise the strain measure. Decrement velocity plotted in the figures is the difference between the initial impact velocity and the subsequent velocity of the debris front (cloud velocity).

3.1 Copper.

Initial experiments on copper were performed with PMMA impact plates. Test CU-5 at an impact velocity slightly over 4 km/s produced insufficient impulse to shatter the sample sphere. Substantial plastic deformation of the sphere is observed. An operational deformation strain as defined earlier of 0.37 was determined in this test.

Test CU-6 on PMMA at near the maximum velocity for the projectile package mass exceeded the threshold impulse for sample fragmentation. An expanding disc of debris is characteristic of the observed behavior in an earlier study on steel [Kipp, *et al.*, 1993a, 1993b].

To achieve higher impulsive loading of the test spheres, glass barrier plates were used for the remaining experiments on copper. Tests CU-7 through CU-10 provided a systematic range of increasing impulsive loads. The observed responses ranged from breakup into several fragments with very modest debris expansion just above the threshold (CU-9) to quite intense fragmentation and debris expansion at the highest impact velocity (CU-8). In each case most of the impulsive energy causing fragmentation translates into the radial expansion of a disc of sphere debris. There is also a minor amount of fine trailing debris. The impulsive load resulted in a debris velocity reduced by about 10-15% from the initial impact velocity.

Table 3.1:
OFHC Copper

Test Number	Plate Material	Impact [c] Velocity (km/s)	d_1 (cm)	d_2 (cm)	Δt (μs)	Expans. Velocity (m/s)	Cloud Velocity (km/s)	Def. Strain
CU-5	PMMA[a]	4.05	16.5	28.8	35.1	0	3.50	0.37
CU-6	PMMA[a]	4.65	18.8	32.8	35.1	57	3.99	—
CU-7	Glass[b]	4.65	18.7	31.8	35.0	357	3.74	—
CU-8	Glass[b]	4.70	18.3	31.7	35.0	386	3.83	—
CU-9	Glass[b]	3.67	15.5	29.2	46.0	54	2.98	—
CU-10	Glass[b]	4.21	15.6	28.6	38.0	211	3.42	—

[a] Polymethyl-methacrylate, Rohm and Haas Type II UVA (thickness = 3.14 mm).
[b] GE dynasil 1000 (thickness = 3.17 mm).
[c] Projectile mass = 1.20 g.

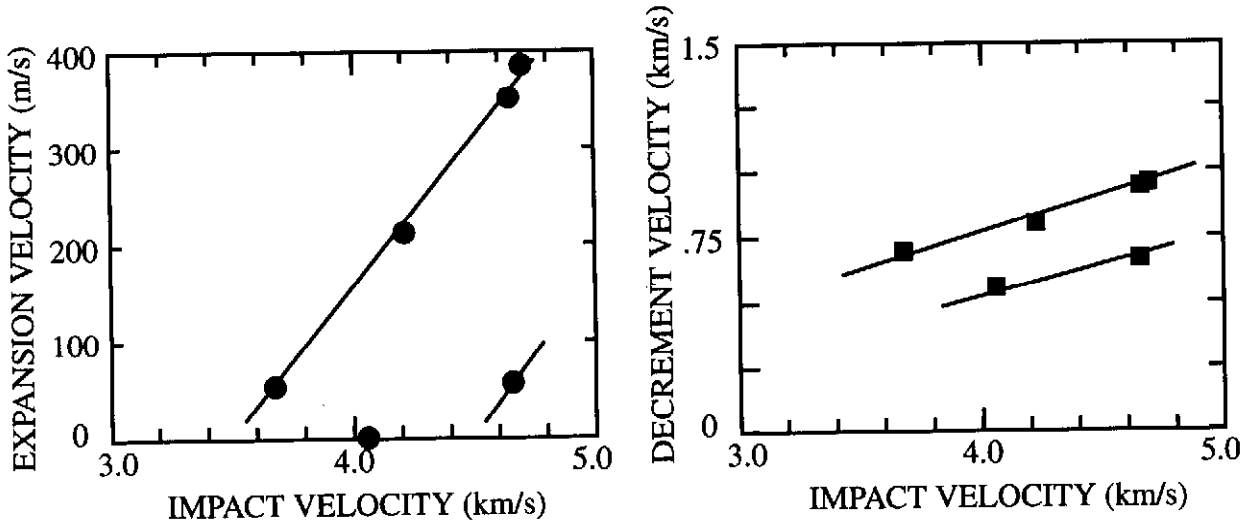

Figure 3.1 OFHC copper debris cloud expansion and decrement velocity dependence on impact velocity.

3.2 Aluminum

For the 7075-T6 aluminum spheres PMMA impact barriers were sufficient to exercise a wide range of breakup and fragmentation behavior. Test AL-17 at an impact velocity of 2.23 km/s was subcritical and exhibited impact deformation characteristics similar to copper. Tests AL-13 and AL-18 demonstrated behaviors at or near incipient fragmentation. At higher impact velocities the characteristic debris disc constituting the majority of the sample material begins to emerge. Expansion velocities of this disc constitute the values reported in the Table.

The radiographic images of the fragment debris appear to show a proportionally larger component of finer trailing fragment debris than did the copper. The origins of this finer debris appear to differ from that of the primary central disc but its source remains uncertain. The distribution of this debris appears to be that of a conical plume which expands more rapidly but falls behind the central fragment disc. Our current thought is that these fragments originate from material at the impact interface during the last stages of sphere-plate contact (see numerical section). Noting the radiograph for the subcritical test on aluminum (AL-17) and the similar radiograph for copper (CU-5), we refer to the extreme radial lip of material which, under more intense loading, might be expected to detach and undergo circumferential fragmentation creating the observed debris.

Table 3.2:
7075 Aluminum

Test Number	Plate Material	Impact[d] Velocity (km/s)	d_1 (cm)	d_2 (cm)	Δt (μs)	Expans. Velocity (m/s)	Cloud Velocity (km/s)	Def. Strain
AL-12	PMMA[a]	3.51	13.2	26.7	46.1	130	2.93	—
AL-13	PMMA[a]	2.97	15.9	31.8	64.1	23	2.48	—
AL-14	PMMA[a]	3.92	17.7	33.6	48.1	281	3.31	—
AL-15	PMMA[a]	4.67	19.5	35.5	42.0	417	3.81	—
AL-16	PMMA[a]	3.17	16.2	30.2	52.1	96	2.69	—
AL-17	PMMA[a]	2.23	16.0	30.3	76.1	0	1.88	0.26
AL-18	PMMA[a]	2.59	—[b]	—[b]	—[b]	0[c]		0.32[c]

[a] Polymethyl-methacrylate, Rohm and Haas Type II UVA (thickness = 2.92 mm)
[b] Only one exposure and position is uncertain
[c] Incipient breakup occurs although deformation sufficient to estimate strain is observed.
[d] Projectile mass = 0.372 g.

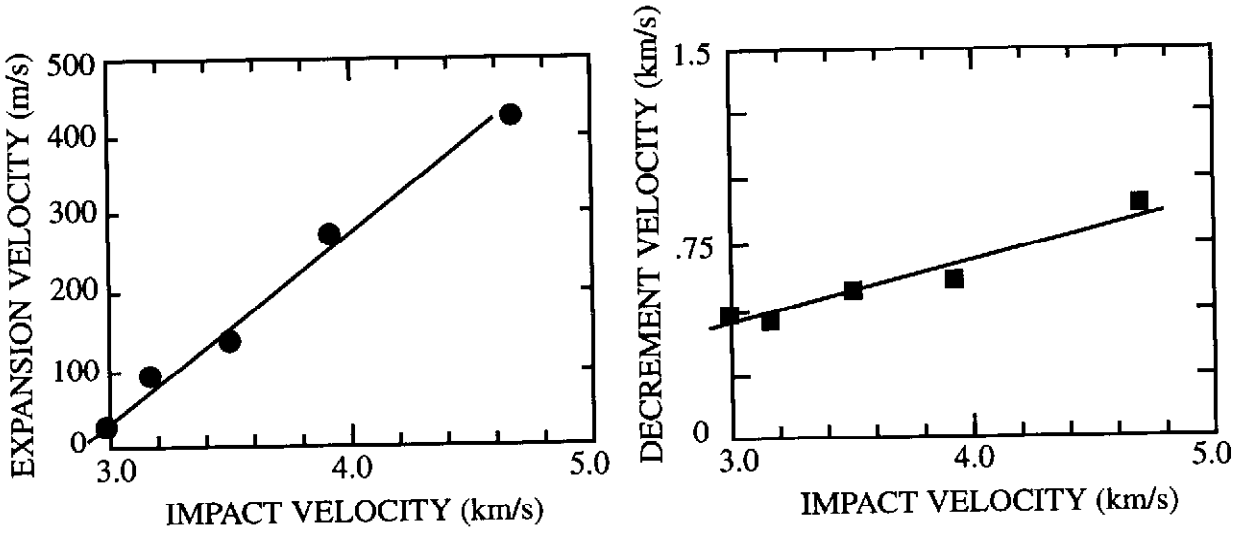

Figure 3.2 7075 aluminum debris cloud expansion and decrement velocity dependence on impact velocity.

3.3 Steel AF1410.

For AF1410 steel it was found that glass impact plates were necessary to achieve adequate fragmentation for the present study. Impulse loading conditions insufficient to cause fragmentation were achieved in only one experiment (AF-1). The more symmetric lens shape of the deformed sphere in the radiographic record contrasts with that observed for copper and aluminum. This may reflect the higher strength properties of this steel. It may also be a consequence of a glass versus a PMMA barrier plate.

The resulting debris again takes on the pattern of an expanding disc of fragments. There is perhaps a tendency to exhibit more axial dispersion than observed for copper or aluminum. There is little evidence of a trailing plume of fine debris, again in contrast to copper or aluminum.

Table 3.3:
AF1410 Steel

Test Number	Plate Material	Impact[b] Velocity (km/s)	d_1 (cm)	d_2 (cm)	Δt (μs)	Expans. Velocity (m/s)	Cloud Velocity (km/s)	Def. Strain
AF-1	Glass[a]	3.54	6.7	20.1	42.2	0	3.18	0.28
AF-2	Glass[a]	4.22	7.2	23.2	43.2	186	3.70	—
AF-3	Glass[a]	3.79	7.2	22.4	46.2	11	3.29	—
AF-4	Glass[a]	4.63	7.1	22.6	38.2	340	4.06	—
AF-5	Glass[a]	4.30	7.3	22.2	40.2	224	3.71	—
AF-6	Glass[a]	3.79	7.6	22.0	43.2	80	3.33	—
AF-7	Glass[a]	4.20	7.9	23.8	43.1	208	3.69	—

[a] GE dynasil 1000 (thickness = 3.15 mm)
[b] Projectile mass = 1.10 g.

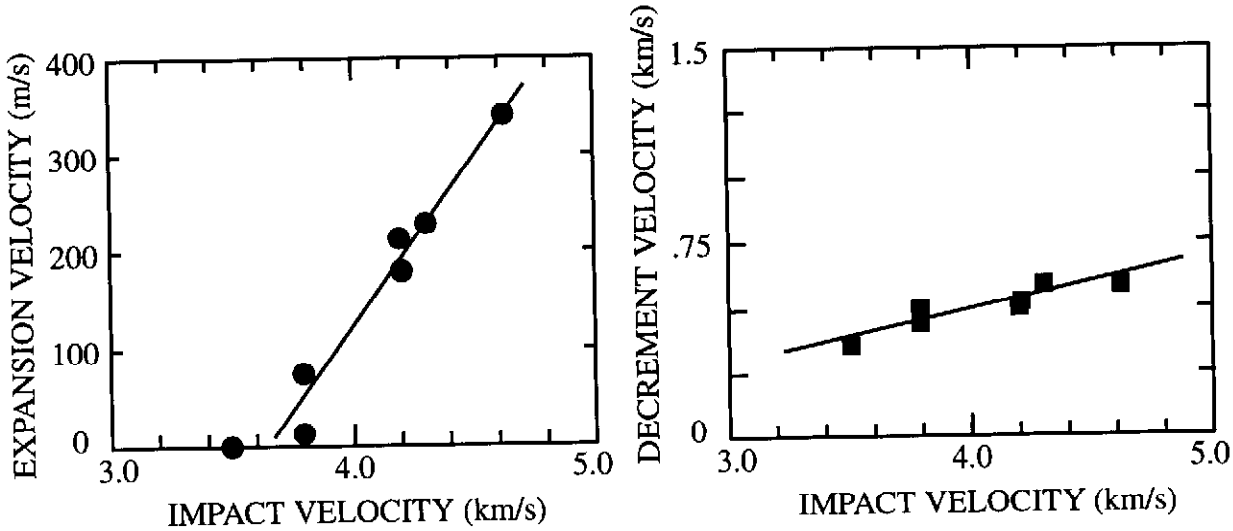

Figure 3.3 AF 1410 steel debris cloud expansion and decrement velocity dependence on impact velocity.

3.4 Steel D6AC.

Impact conditions for experiments on D6AC steel closely duplicate those for AF1410 steel. Glass plates were again used as the barrier material in all tests. Several experiments in this series did not achieve the fragmentation threshold (D-4, D-5 and D-7). Increasing levels of deformation strain were observed over the three subcritical tests. The observed deformation shape induced by the impact was qualitatively similar to that of AF1410 steel. Note that the decremental velocity is almost independent of impact velocity for this material.

The spatial domain of the fragment debris disc is less distinct than for AF1410 steel. At the highest impact velocity of 4.82 km/s there is evidence of trailing debris and onset of the responsible fragmentation mechanism for this debris.

Table 3.4:
D6AC Steel

Test Number	Plate Material	Impact[b] Velocity (km/s)	d_1 (cm)	d_2 (cm)	Δt (μs)	Expans. Velocity (m/s)	Cloud Velocity (km/s)	Def. Strain
D-1	Glass[a]	3.76	10.3	26.2	49.1	51	3.24	—
D-3	Glass[a]	4.20	6.8	22.5	42.2	190	3.72	—
D-4	Glass[a]	3.02	7.0	20.9	54.1	0	2.57	0.22
D-5	Glass[a]	3.30	6.7	21.8	53.1	0	2.84	0.27
D-6	Glass[a]	4.82	7.0	23.2	38.1	375	4.25	—
D-7	Glass[a]	3.60	7.3	23.7	52.1	0	3.15	0.31
D-8	Glass[a]	4.18	6.8	23.3	45.1	189	3.66	—
D-9	Glass[a]	4.56	6.9	22.6	39.0	288	4.03	—

[a] GE dynasil 1000 (thickness = 3.15 mm).
[b] Projectile mass = 1.07 g.

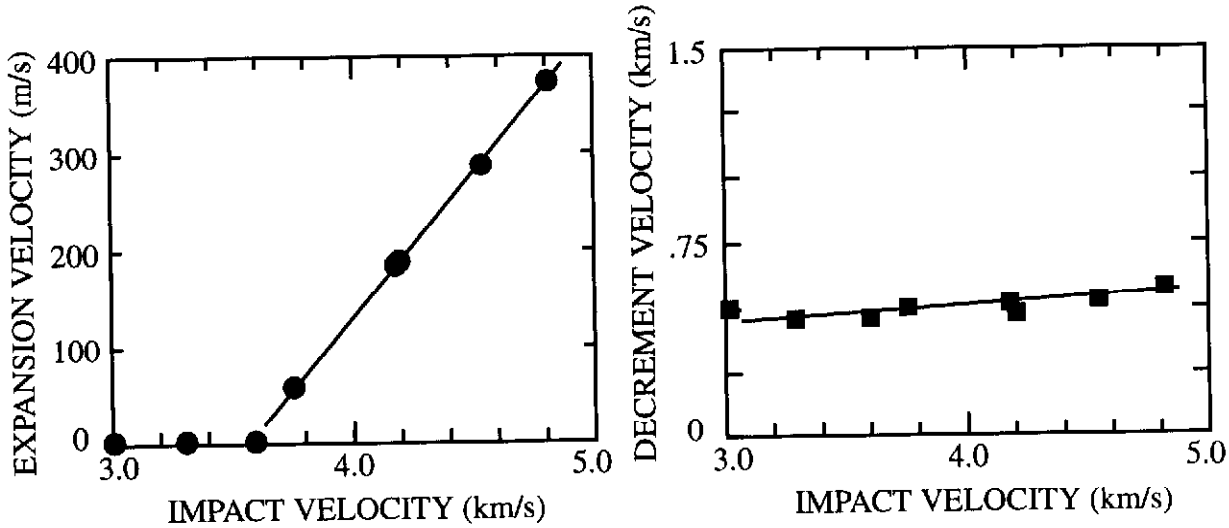

Figure 3.4 D6AC steel debris cloud expansion and decrement velocity dependence on impact velocity.

3.5 Steel (APR).

A series of the present fragmentation tests was performed on an unspecified steel extracted from 7.6 mm armor piercing rounds (APR). The primary purpose of these tests was to calibrate fragment models in computational codes. These data are included for completeness.

The breakup threshold for this steel was significantly less than was observed for AF1410 and D6AC steels. Again a characteristic debris disc was observed, although substantial trailing fragment debris occurred in the highest impact velocity experiment (AP-3).

Table 3.5:
APR Steel

Test Number	Plate Material	Impact[c] Velocity (km/s)	d_1 (cm)	d_2 (cm)	Δt (μs)	Expans. Velocity (m/s)	Cloud Velocity (km/s)	Def. Strain
AP-1	PMMA[a]	4.07	12.8	26.5	36.1	42	3.80	—
AP-3	Glass[b]	4.00	15.6	27.7	35.0	214	3.46	—
AP-4	Glass[b]	3.43	14.5	28.0	46.1	94	2.93	—
AP-6	Glass[b]	3.01	12.6	26.4	55.1	18	2.50	—
AP-7	Glass[b]	3.73	14.5	29.8	48.1	130	3.18	—

[a] Polymethyl-methacrylate, Rohm and Haas Type II UVA (thickness = 3.14 mm).
[b] GE dynasil 1000 (thickness = 3.17 mm).
[c] Projectile mass = 0.88 g (sphere diameters were 6.0 mm diameter).

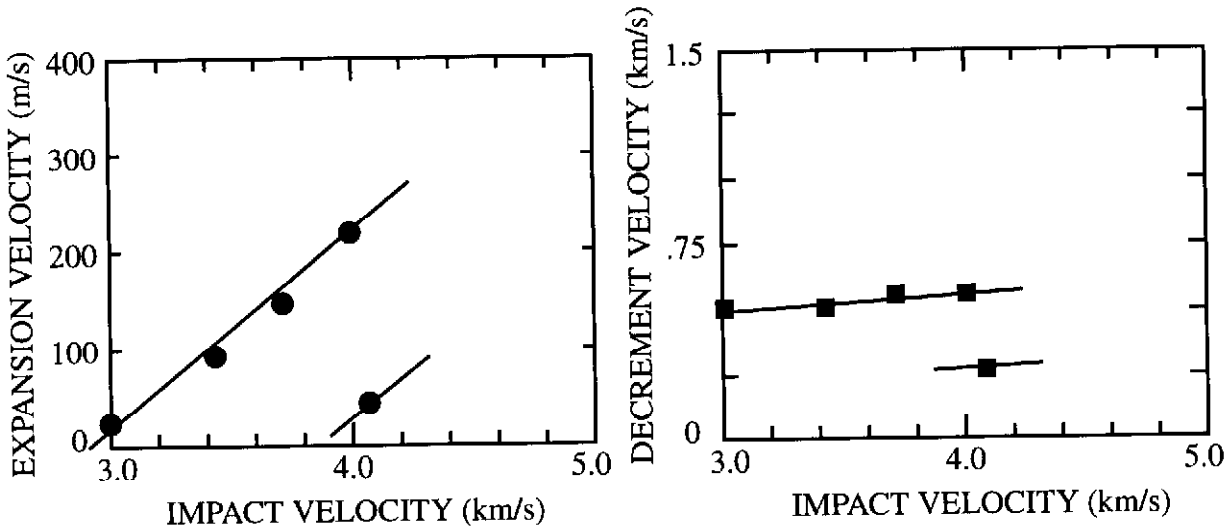

Figure 3.5 APR steel debris cloud expansion and decrement velocity dependence on impact velocity.

3.6 Steel (SS304).

One test (SS-1) of the series of experiments on a stainless steel appears to not have achieved the break up threshold. Only the second (later time) radiograph was successful in this test. The angularity of the sample deformation profile in this radiograph suggests that some degree of incipient rupture may have occurred. Extrapolation of the expansion velocity data to a threshold impact velocity is suspect because the three tests in which expansion velocity measurements were made did not adequately span the range of interest.

The experiments at higher velocity did provide clear evidence of fragmentation and uniform expansion of the debris disc.

Table 3.6:
SS304 Steel

Test Number	Plate Material	Impact[b] Velocity (km/s)	d_1 (cm)	d_2 (cm)	Δt (μs)	Expans. Velocity (m/s)	Cloud Velocity (km/s)	Def. Strain
SS-1	Glass[a]	3.58	—[c]	22.1	71.8	0	3.08	0.37[d]
SS-2	Glass[a]	4.22	2.4	16.2	37.9	230	3.64	—
SS-4	Glass[a]	4.53	4.7	16.6	31.0	350	3.84	—
SS-6	Glass[a]	4.11	3.7	17.0	38.2	220	3.48	—

[a] GE dynasil 1000 (thickness = 3.17 mm).
[b] Projectile mass = 1.10 g.
[c] Only one exposure. Cloud velocity determined from time and distance from target.
[d] Incipient breakup may have occurred.

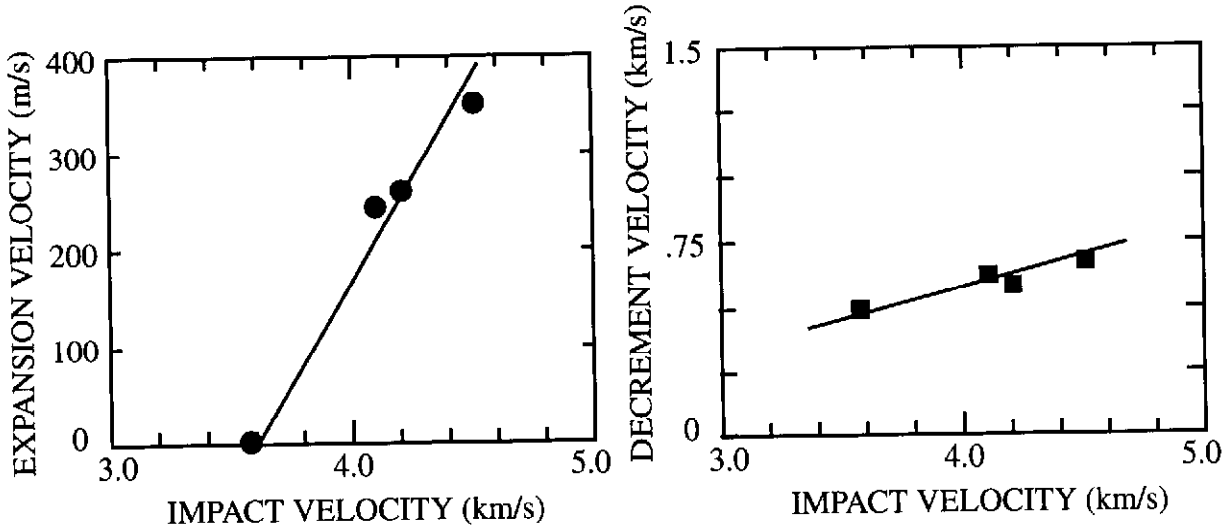

Figure 3.6 SS-304 stainless steel debris cloud expansion and decrement velocity dependence on impact velocity.

3.7 Tantalum.

Pure tantalum was the most difficult metal to exceed the fragmentation threshold under the current range of test conditions. Barrier plates of glass did not provide sufficient impulse to induce fragmentation and recourse to alumina plates was necessary to achieve fragmentation. In only one test, TA6, was a clear fragmentation and expansion of the primary central disc observed. Test TA4 showed severe distortion of this central disc region but lack of expansion between the early and late radiographs indicated that fragmentation did not occur. A distortional strain close to unity was observed in this test.

In several tests an appreciable amount of more dispersed trailing debris was observed. This debris presumably originates from the periphery of the contact between sphere and plate (see numerical simulation).

Table 3.7:
Tantalum

Test Number	Plate Material	Impact[c] Velocity (km/s)	d_1 (cm)	d_2 (cm)	Δt (μs)	Expans. Velocity (m/s)	Cloud Velocity (km/s)	Def. Strain
TA-1	Glass[a]	3.43	7.4	—[d]	—[d]	0	3.33	0.35
TA-3	Glass[a]	2.12	6.1	13.3	36.1	0	1.99	0.2
TA-4	Alumina[b]	3.00	5.2	18.1	50.0	0-10	2.58	1.0
TA-5	Alumina[b]	2.41	5.4	17.0	57.1	0	2.03	—
TA-6	Alumina[b]	3.43	4.6	17.4	43.0	130	2.98	0.6

[a] GE dynasil 1000 (thickness = 3.20 mm).
[b] GE lucolax (thickness = 3.80 mm).
[c] Projectile mass = 2.30 g.
[d] Only one exposure. Cloud velocity determined from time and distance from target.

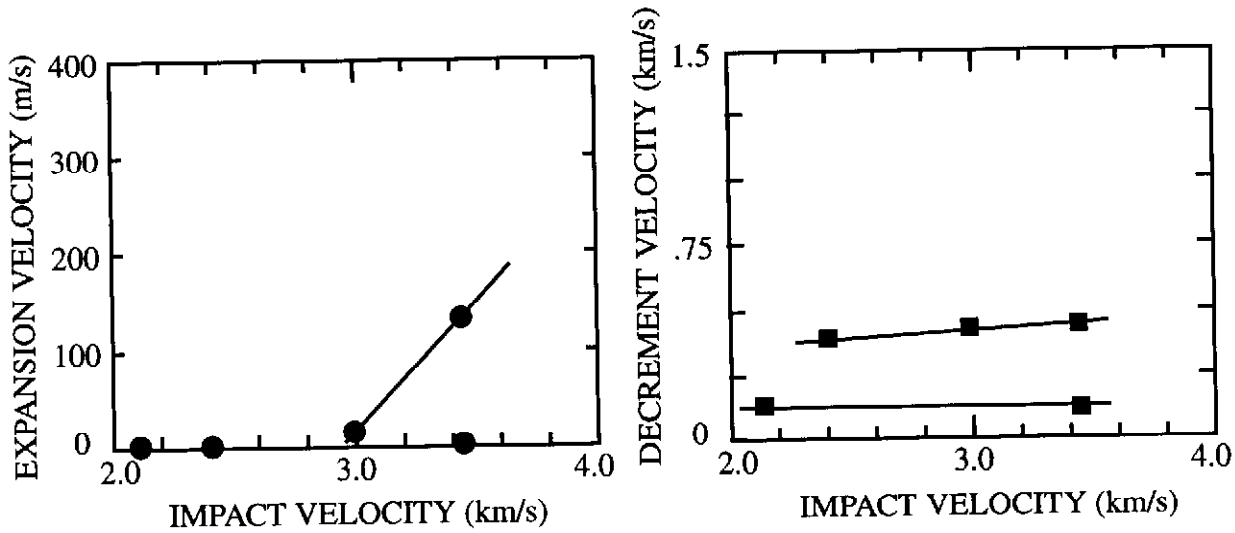

Figure 3.7 Tantalum debris cloud expansion and decrement velocity dependence on impact velocity.

3.8 Titanium.

This titanium alloy was adequately fragmented with glass barrier plates. This material exhibited more pronounced axial dispersion than did fragment debris from the other metals tested. Lower amplitude tests (TI2, TI3) only moderately exceeding breakup threshold actually showed more significant axial spreading than radial spreading. Test TI1 is visually comparable to data for earlier metals. Tests TI5, however, under the highest impact conditions indicates a severe trailing debris problem, making titanium alloy one of the least satisfactory metals for conducting the present fragmentation properties test method.

Table 3.8:
Titanium 6Al4Va

Test Number	Plate Material	Impact[c] Velocity (km/s)	d_1 (cm)	d_2 (cm)	Δt (μs)	Expans. Velocity (m/s)	Cloud Velocity (km/s)	Def. Strain
TI-1	Glass[a]	3.64	3.8	15.0	40.4	220	2.77	—
TI-2	Glass[a]	2.82	4.5	16.2	58.0	40	2.02	—
TI-3	Glass[a]	2.71	4.6	17.0	68.2	0-5[d]	1.82	—
TI-5	Glass[a]	4.05	5.4	18.1	40.8	360	3.11	—
TI-6	PMMA[b]	3.42	5.3	21.6	55.2	0	2.95	0.23

[a] GE dynasil 1000 (thickness = 3.20 mm).
[b] Polymethyl-methacrylate, Rohm and Haas Type II UVA (thickness = 3.10 mm).
[c] Projectile mass = 0.60 g.
[d] Middle of two fragments.

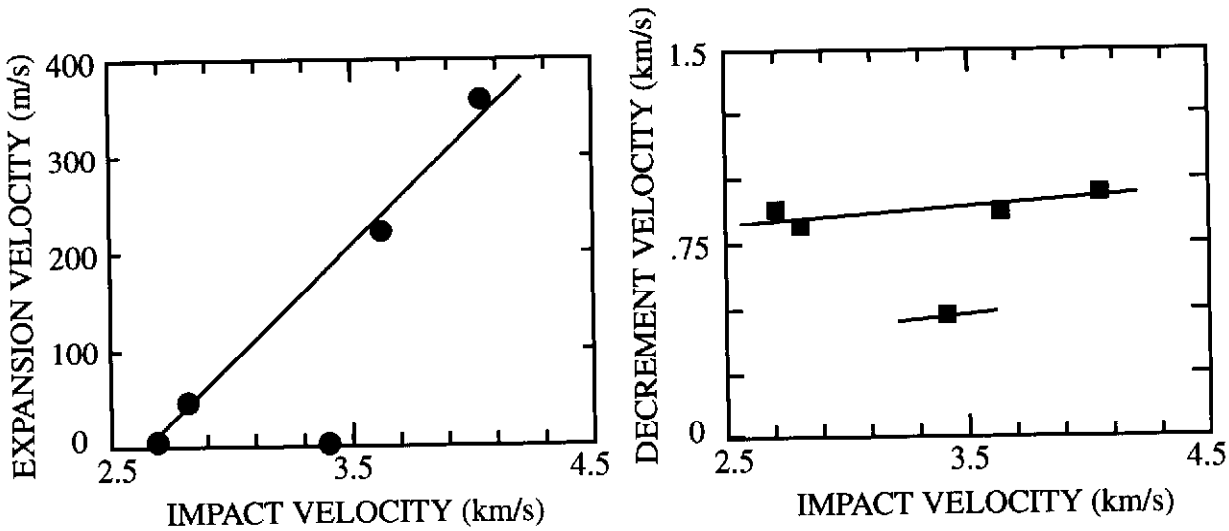

Figure 3.8 6Al4Va titanium debris cloud expansion and decrement velocity dependence on impact velocity.

4 ANALYSIS.

For an experimental method to be a viable material properties test it is necessary to be able to monitor the load on the sample and measure the response of the sample to that load. The observed relationship between load and response mirrors the constitutive representation of that material and provides the material property behavior sought.

4.1 Characteristics of the Impact-Induced Stress Load.

The transient stress loading of a spherical projectile undergoing normal impact on a thin plate has received attention by numerous previous authors. The evolution of stress waves in this nonlinear and nonplanar impact event is complex. A fully intuitive understanding of such an event is probably not achievable.

Computational simulations of the impact event can shed some light on the progression of effects. In some cases, however, such simulations only serve to further emphasize the complexities of the event.

4.2 The Sphere-on-Plate Impact Event.

A degree of intuitive understanding is achieved through consideration of the stress history at the first point of contact of the sphere and the plate on the central axis of impact. After some reflection one is led to recognize that the pressure (or axial stress) must look qualitatively as shown in Figure 4.1.

Characteristic pressure amplitudes and times in the profile are reasonably calculated from the geometry and kinematics of the event. The initial shock pressure p_h (the Hugoniot pressure) at the interface, before curvature of the spherical interface is realized, is gov-

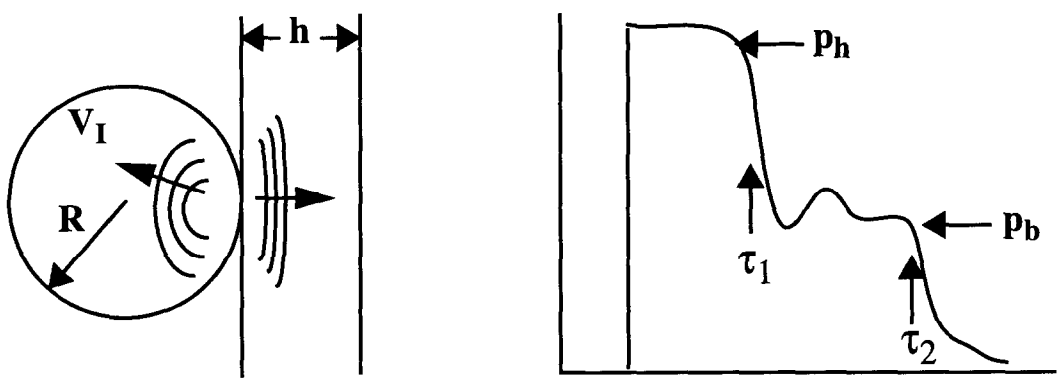

Figure 4.1 The qualitative pressure history at the central-axis impact interface identifying characteristic pressure amplitudes and times in the sphere-on-plate impact event.

erned by the Hugoniot shock-wave conditions for the planar impact of the two solids, and is given by,

$$p_h = \frac{Z_S Z_T}{Z_S + Z_T} V_I, \tag{4.1}$$

where V_I is the impact velocity while Z_S and Z_T are the mechanical shock impedances of sample and target materials, respectively. The mechanical impedance, $Z = \rho c$, is the product of the density and a wave speed which is, to first order, the acoustic wave velocity, and for more accurate estimates the amplitude dependent shock velocity.

The Hugoniot pressure is maintained at this interface through a time duration τ_1 which is governed by the arrival of pressure release waves from the diverging spherical surface of the sphere. This assumes that the impacted plate is sufficiently thick that shock release is not first realized from the back of the plate.

The subsequent central interface pressure drops rapidly to a value approximated by the Bernoulli pressure,

$$p_b = \frac{1}{2}\rho_T V_I^2. \tag{4.2}$$

Equation 4.2 is reasonable if the density of the target plate is significantly less than the projectile. Further release of the pressure occurs at time τ_2 when pressure waves experience the back free surface of the target plate either through the reflected shock or through emergence of the stagnation pressure profile for somewhat thicker plates. Note for very thin plates τ_2 can be less than τ_1.

4.3 Coupling of the Impact Shock Energy.

Early in the impact event shock energy is coupled into the spherical sample. The shock pressure does work on the sphere from the instant of impact up to time τ_1 which completes the shock coupling phase. There is reasonably compelling evidence that this shock energy is solely responsible for fragmentation of the spherical sample [Kipp, *et al.*, 1993a, 1993b; Grady and Kipp, 1995].

The magnitude of this energy can be estimated through consideration of a model of the shock coupling process during the normal impact of a spherical projectile on a planar surface. The model was originally pursued by Ang (1990) to evaluate jetting at the impact interface. It was subsequently extended to processes of shock energy coupling and fragmentation [Kipp, *et al.*, 1993a, 1993b; Grady and Kipp, 1995]. The present discussion extracts further results important to the shock energy coupling process.

The contact process during impact is illustrated in Figure 4.2. The sphere of radius R impacts a surface at a velocity V_I. A circular line of contact at radius a propagates outward from the initial point of impact and is initially supersonic but slows rapidly as the spherical surface curves away from the target plane. This contact circle transitions from supersonic to subsonic velocity at a radius a_c which determines the maximum area of shock coupling into the sphere. Release waves then propagate toward the central axis quenching the shock coupling phase (τ_1 in Figure 4.1).

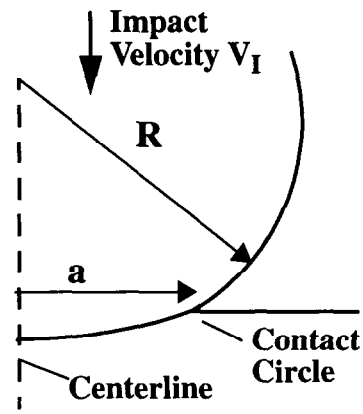

Figure 4.2 Contact process in the normal impact of a sphere on a planar surface.

From the geometry of the event it has been shown that [Kipp, *et al.*, 1993a, 1993b; Grady and Kipp, 1995],

$$a_c = V_I t_c \sqrt{\frac{2R}{V_I t_c} - 1}, \tag{4.3}$$

$$c = \frac{V_I\left(\frac{R}{V_I t_c} - 1\right)}{\sqrt{\frac{2R}{V_I t_c} - 1}}, \tag{4.4}$$

provide conditions for the radius a_c of the shock coupling disc and the time of its development t_c. Equations 4.3 and 4.4 represent a linear (sonic) approximation. Generally, under conditions of large amplitude shock waves the wave velocity c would be replaced by the shock velocity U_s [Kipp, *et al.*, 1993a, 1993b; Grady and Kipp, 1995].

Identifying the nondimensional parameters $U = V_I/c$, $A_c = a_c/R$ and $T_c = ct_c/R$ one obtains the solutions,

$$A_c = \frac{a_c}{R} = \frac{U}{\sqrt{U^2 + 1}}, \tag{4.5}$$

$$T_c = \frac{ct_c}{R} = \frac{1}{U}\left(1 - \frac{1}{\sqrt{U^2 + 1}}\right). \tag{4.6}$$

The time t_c (or T_c) determines the time of propagation of the contact circle to the maximum radius of supersonic motion. Shock coupling continues through the duration of lateral release wave propagation to the central axis which requires an additional time $t_r = a_c/c$. The total shock coupling duration $t_{sc} = t_c + t_r$ is found to be,

$$T_{sc} = \frac{c}{R}(t_c + t_r) = \frac{1}{U}\left(1 + \frac{U^2 - 1}{\sqrt{U^2 + 1}}\right). \tag{4.7}$$

Shock energy is coupled into the spherical sample during the period of growth of the contact disc and is completed when lateral release waves reach the central axis. The coupled shock energy can be calculated from the work on the contact interface over the coupling time t_{sc} and is generally,

$$E_s = 2\pi \int_0^{a_c t_{sc}} \int_0 \frac{p^2}{\rho c} \xi d\xi dt. \tag{4.8}$$

This will be approximated by,

$$E_s = \alpha \frac{p^2}{\rho c} a_c^2 t_{sc}, \tag{4.9}$$

where α is a constant which accounts for the loading time variation with radius over the contact disc. It is reasonable to assume an ellipsoidal shock volume [Kipp, *et al.*, 1993a, 1993b; Grady and Kipp, 1995] in which case $\alpha = 2\pi/3$.

The previous equations show that total shock energy coupled into the sphere as impact velocity increases depends on both the shock amplitude and on the extent of the shock coupling disc. Figure 4.3 illustrates the increase in contact disc radius, shock coupling

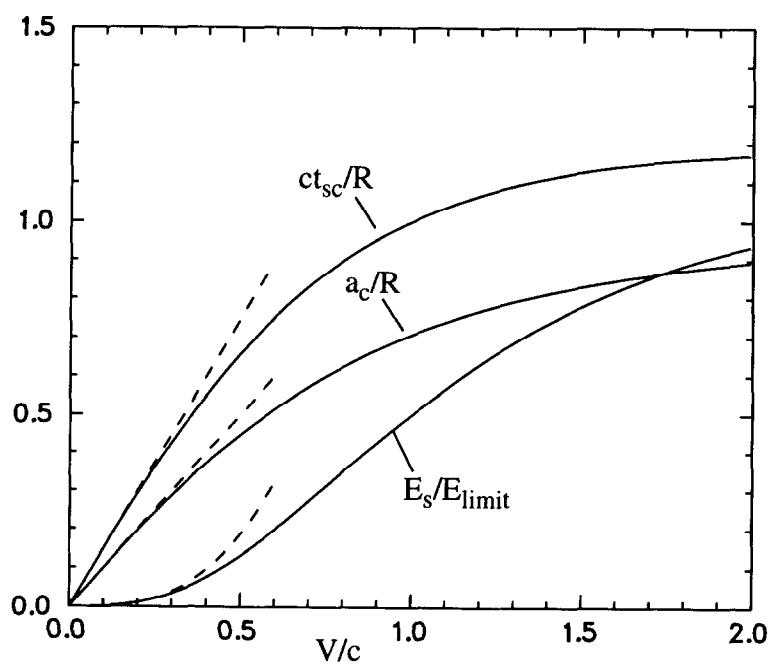

Figure 4.3 Variation of coupled shock energy and coupling parameters with the impact velocity.

duration and shock energy. Shock energy is normalized by the limiting shock energy as $V/c \rightarrow \infty$; namely,

$$E_{limit} = \frac{2\pi}{3}\frac{p^2}{\rho c^2}R^3 . \tag{4.10}$$

Dashed lines indicate the small V/c limit in which both a_c and t_{sc} increase linearly with impact velocity and the coupled shock volume, $\sim a_c^2 t_{sc}$, increases as the cube of the velocity. Since energy density increases with the square of the impact velocity the total shock energy in the low velocity limit will increase as the fifth power of the velocity.

Several changes to the relation for the shock energy coupled into the spherical sample in Equation 4.9 can be made to improve the estimate. First, at impact velocities sufficient to fail and fracture metal samples shock pressure amplitudes in the range of tens of GPa are achieved. The nonlinear compression of solids at these stresses are better accounted for by replacing the wave speed c in Equation 4.9 with the shock velocity U_s [Kipp, *et al.*, 1993a, 1993b; Grady and Kipp, 1995]. Second, when the circle of contact between the planar and spherical surfaces slows to sonic velocities, stress release waves originate and propagate radially inward decoupling the shock loading process. In the earlier analysis leading to Equation 4.9 it was tacitly assumed that this transition and release is controlled by the wave speed in the sphere material. If the sphere and plate materials are different it is more likely that decoupling will be controlled by the higher wave speed material. Again, Equation 4.9 applies provided care is taken to use the correct wave speeds for the decoupling and the energy density portions of the estimate [Kipp, *et al.*, 1993a, 1993b; Grady and Kipp, 1995].

Earlier studies [Kipp, *et al.*, 1993a, 1993b; Grady and Kipp, 1995] have indicated that this prompt shock energy is principally responsible for the fragmentation and radial dispersal of the spherical sample. Thus estimates of the coupled shock energy at an impact velocity corresponding to the breakup threshold should provide a measure of the energy requirement to achieve failure under the present mode of deformation. This estimate has been made for the present data using Equation 4.9 accounting for finite amplitude shock compression as discussed earlier. These data are provided in Table 4.1. The shock energy E_s at threshold which is absorbed in the spherical sample without fracture will be identified as W_p. In Table 4.1 $w_p = W_p/m$ where m is the mass of the sphere. The threshold impact velocity V_c is obtained from the expansion velocity versus impact velocity plots from the previous section and the threshold shock pressure p_c from the normal shock impedance solution (Equation 4.1). Shock velocities under the threshold impact conditions for both sphere and target plate material are provided in Table 4.1. Shock energy estimates based on shock decoupling controlled by each wave velocity are provided in the last column (sphere material left - plate material right). It is expected that the lower value based on decoupling governed by the higher wave speed material would be preferred.

Table 4.1:
Failure Energies Based on Analytic Solution

Material (Sphere)	Material (Plate)	Density (kg/m^3)	V_c (m/s)	p_c (GPa)	U_s(m/s) (Sphere)	U_s (m/s) (Plate)	w_p[2] (J/g)
Copper	Glass	8930	3500	34	5060	5530	75-56
Aluminum	PMMA	2800	2800	14	6260	5670	32-48
Steel (1)[1]	PMMA	7900	3100	21	5300	6570	23-12
Steel (2)[1]	Glass	"	3650	36	5750	5690	70-66
Steel (3)[1]	Glass	"	3600	35	5730	5640	66-63
Steel (4)[1]	Glass	"	2900	25	5440	4840	25-38
Steel (5)[1]	Glass	"	3600	35	5730	5640	66-63
Titanium	Glass	4520	2650	19	5850	4260	25-75
Tantalum	Alumina	16700	2950	80	4640	10300	124-9

[1] Steels are respectively (1) E51200; (2) AF1410; (3) D6AC; (4) APR; (5) SS304.
[2] Estimates on the left and the right are based on shock coupling time controlled by shock (and release) velocities in sphere and plate material, respectively. $w_p = W_p/m$ where W_p is the threshold value of E_s.

4.4 Critical Failure Energy from an Energy Balance Approach

An alternative method for evaluating the critical energy needed to induce incipient sample (projectile) breakup has also been pursued. The method works directly with the expansion velocity data plotted for each material in the earlier section. The viability of this critical energy as a material failure property will be explored.

With reasonable generality it can be stated that the shock energy input to the spherical specimen on impact can be decomposed into the kinetic energy T imparted to the sphere (here we regard the sphere initially at rest subject to impact by the plate at velocity V_I) and the energy of dissipation W absorbed by the sphere through several processes,

$$E = T + W. \tag{4.11}$$

The kinetic energy readily decomposes into the center-of-mass kinetic energy and the longitudinal and radial expansion components relative to the center of mass,

$$T = T_{cm} + T_{long} + T_{rad}. \tag{4.12}$$

It is experimentally observed that the longitudinal expansion component is small — hence the pancake shape assumed by the resulting debris clouds in the radiographic records. The center of mass kinetic energy imparted to the samples is not small as is evidenced by the axial velocity change plotted with the data in the previous section. However it can be shown that the axial impulse (and kinetic energy) imparted to the sphere during shock coupling is small. Most of the momentum exchange occurs during the later Bernoulli penetration.

The important dissipative terms appear to be those due to plasticity, shock heating and new fracture surface,

$$W = W_p + W_h + W_f. \tag{4.13}$$

Within the range of interest dissipation due to shock heating W_h and fracture W_f are small enough to be neglected relative to the plastic work W_p.

Thus to a reasonable approximation, in the sphere-on-plate impact experiment, the impact shock energy is assumed to be distributed between the plastic work expended in achieving the failure state and the radial expansion kinetic energy of the resulting debris fragments.

$$E_s = W_p + T_{rad}. \tag{4.14}$$

At this point it is necessary to make an assumption relating the input shock energy to the impact intensity. Namely, we assume that the input energy E_s is proportional to the square of the shock pressure p. In the previous analysis detailed assumptions regarding the shock coupling process led to the $E_s \propto p^2\tau$ illustrated in Equation 4.9. Here we are ignoring possible variations in coupling time — assuming instead that the coupling time is governed by the intrinsic characteristic time of the spherical sample $\tau \propto R/c$. As partial justification for this assumption expansion velocity data for copper and one steel in which two different barrier materials (PMMA and glass) were used are plotted in Figure 4.4 against the calculated shock pressure (Equation 4.1). (Compare with Figures 3.1 and 3.5 for these materials.) The shock pressure is seen to provide a reasonable normalization of these data.

We then write this proportionality as $E_s = A(p/p_c)^2$ and Equation 4.14 becomes,

$$T_{rad} = A\left(\frac{p}{p_c}\right)^2 - W_p. \tag{4.15}$$

A is the proportionality constant and since $T_{rad} = 0$ at $p = p_c$,

$$T_{rad} = W_p\left[\left(\frac{p}{p_c}\right)^2 - 1\right]. \tag{4.16}$$

Experimental evidence indicates that the debris in a sphere-on-plate impact expands as a reasonably uniform disc of fragments in which case the radial kinetic energy is related to

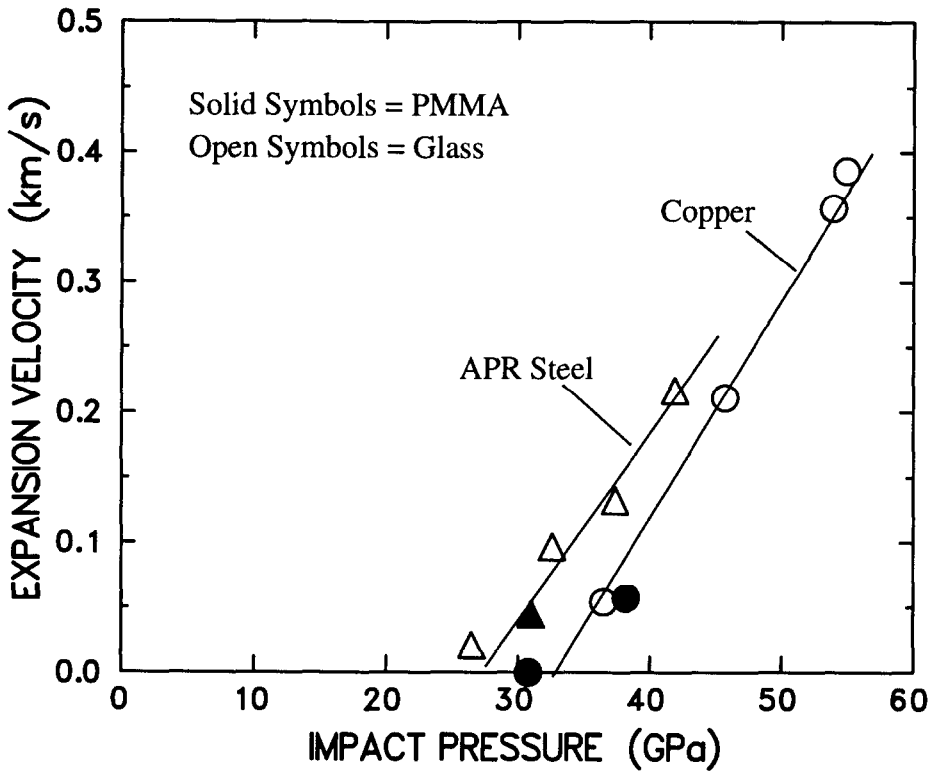

Figure 4.4 Expansion velocity plotted against impact shock pressure comparing impacts on PMMA and glass barrier plates.

the expansion velocity through $T_{rad} = mv_{ex}^2/4$. If a material constant v_c is defined through $W_p = mv_c^2/2$, then Equation 4.16 can be written,

$$\frac{v_{ex}}{v_c} = \sqrt{2}\sqrt{\left(\frac{p}{p_c}\right)^2 - 1}. \tag{4.17}$$

Equation 4.17, based on reasonable assumptions regarding partitioning of energy in the present sphere-on-plate impact experiments, provides an expression for normalizing the expansion velocity data for all of the materials tested to a single plot. The two constants v_c and p_c, within this representation, are sufficient to characterize a specific material. The constant v_c, or its equivalent W_p, is believed to be a useful material constant. The latter provides the magnitude of plastic work that the test sample can absorb before incipient fragmentation occurs. (v_c is conceptually useful in identifying the impact velocity at which, on impacting a rigid barrier, the kinetic energy will be absorbed in plastic work without fragmentation.) The parameter p_c appears to relate to the shock impedance of the test material and to the materials ability to couple in a given magnitude of shock energy at a specific impact velocity.

Experimental data for the metals tested to date have been fit to the functional expression provided in Equation 4.17. Relevant parameters are provided in Table 4.2 and representa-

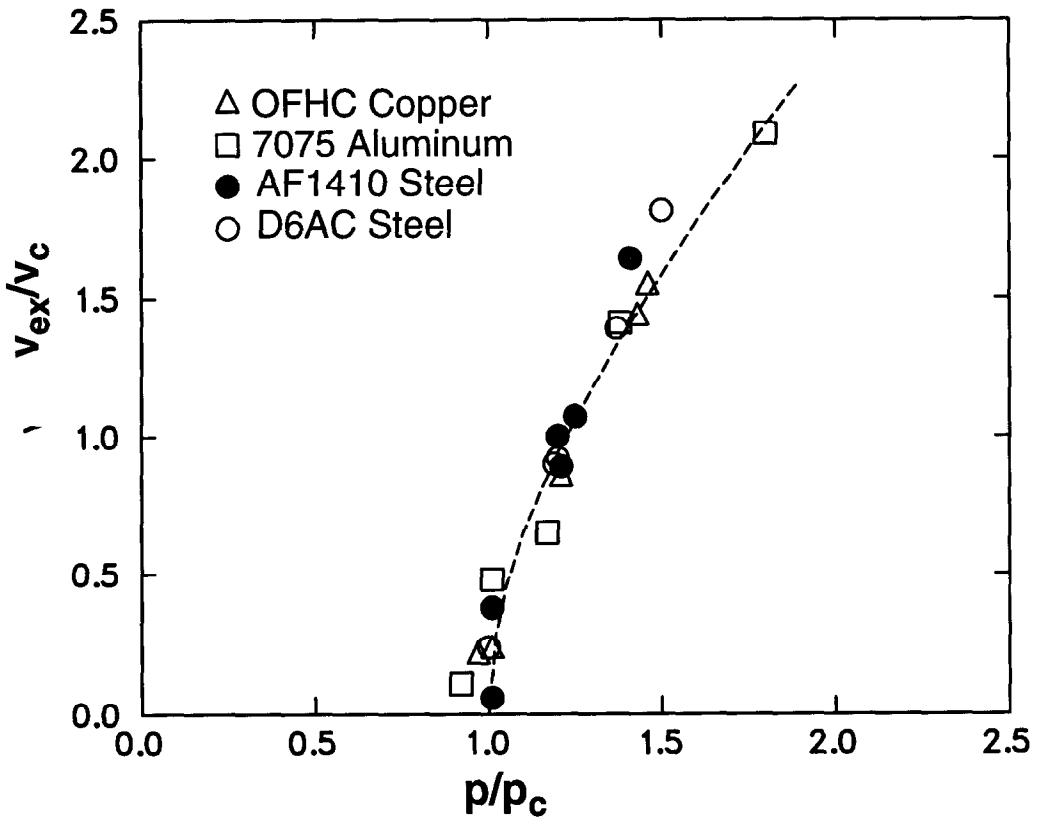

Figure 4.5 Expansion velocity data normalized by parameters resulting from an energy balance assessment of the data (Equation 4.17).

tive data for several of the materials are plotted in Figure 4.5 to examine the universality of Equation 4.17. Critical pressures in Table 4.2 differ slightly from those in Table 4.1 because of the different methods of curve fitting the data.

4.5 Assessment of the Two Methods for Determining Threshold Failure Energy.

The impulse applied to the sample sphere, in addition to slowing the projectile, imparts a dynamic distortional motion which flattens and radially expands the test sphere. Under sufficiently low velocity impact this distortional motion is absorbed as plastic work. At a threshold impact velocity the sample is no longer capable of completely absorbing the distortional energy and failure occurs. It is reasonable to identify this threshold energy as a material property representative of the induced load path (distortional shear at nominally zero confining pressure). Such material data could constrain dynamic failure models.

Two methods for estimating this threshold energy from the experimental data have been explored. In the first a model of the shock coupling process is developed and the threshold impact velocity is used to calculate the threshold energy from the resulting relations. Threshold energies are provided in Table 4.2. The lower value based on the fastest release wave velocity is believed to be the most reasonable.

Table 4.2:
Failure Energies Based on Energy Balance.

Material	p_c (GPa)	v_c (m/s)	w_c [1] (J/g)	ε_c
7075 Aluminum	16	199	19.8	0.42
OFHC Copper	38	250	31.7	0.45
ES51200 Steel	23	129	8.2	0.08
APR Steel	28	124	7.7	—
AF1410 Steel	38	208	21.6	0.31
D6AC Steel	38	208	21.6	0.33
SS304 Steel	36	222	24.6	0.38
Tantalum	81	145	10.5	1.00
Titanium	21	160	12.8	0.23

1 The reported energy is per unit gram. $w_c = W_p/m$ where W_p is defined in the text.

Threshold energy values based on a second method assuming a specific relationship between the energy and the impact shock pressure are provided in Table 4.2. In general the trends are in agreement although discrepancies of as much as a factor of three are noted — the second method providing the lower values

The linear plot of the squared expansion velocity and shock pressure expected from Equation 4.17 is reasonably observed in some cases but not as well in others. The trend when there is a discrepancy is to achieve a higher expansion velocity at a given impact pressure indicating that the assumption of a constant shock coupling time may not be appropriate. This behavior was suspected from the analysis in the first method.

Threshold energies determined by the first method are believed to be the most representative. At present the most useful approach may be to work directly with the models and computational codes to adjust failure model properties.

4.6 Strain to Failure Data.

Experiments performed at impact amplitudes below the breakup threshold lead to test samples that are severely strained but not fragmented. Examples are shown in the later radiograph records. The spherical samples are flattened and radially expanded due to the impact-induced impulse. For the softer metals (aluminum, copper, tantalum, titanium) substantially more flattening is occurring on the impact side. For the steels a more symmetric (elliptic) distortion is observed.

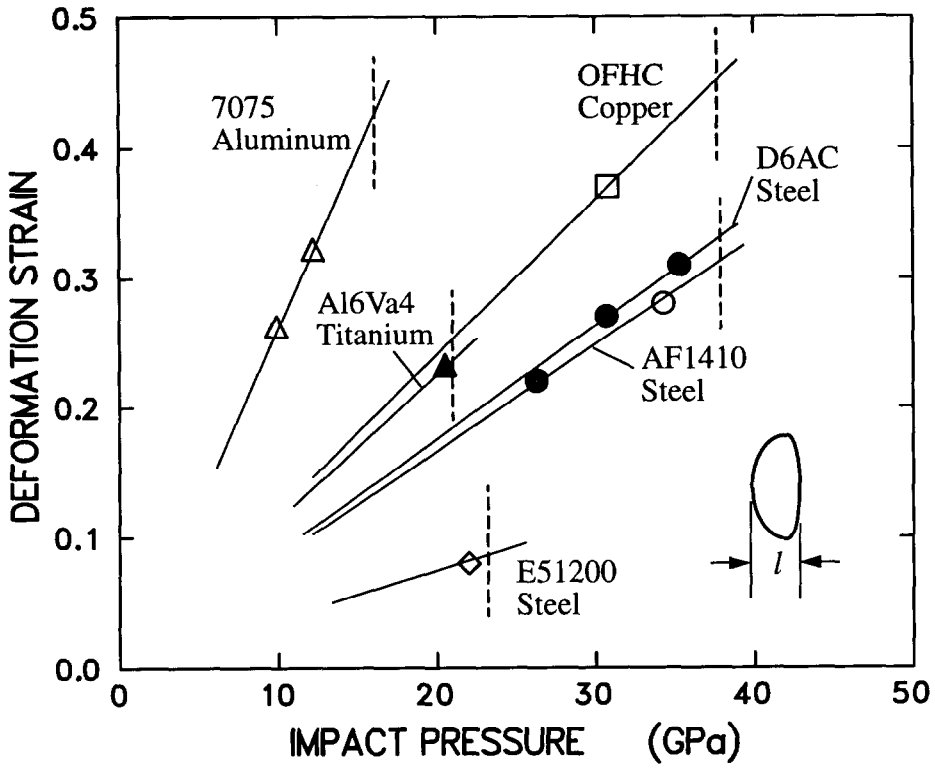

Figure 4.6 Strain-to-failure data for selected metals based on the sphere-on-plate impact tests. Dashed lines indicate failure threshold.

As an operational measure of the induced strain the fractional change in the axial dimension was determined. Namely, $\varepsilon = 1 - l/2R$ where l is the reduced dimension of the sphere of initial radius R (see Figure 4.6). To provide a measure of the critical strain ε_c that the sample can sustain before breakup strain, values are plotted against impact pressure and linearly extrapolated to the threshold pressure at fragmentation as shown in Figure 4.6. Although there is not theoretical justification for this particular extrapolation, strain values are sufficiently close to critical conditions in most cases that large uncertainties are not expected. The data for D6AC steel in which three tests at different subcritical pressures provide an indication of the trend.

Data in the plot of Figure 4.6 show strain-to-failure values ranging from about 0.08 for the ball bearing steel to greater than 0.40 for aluminum and copper. Tantalum, which is not shown in the plot, sustained a deformation strain close to 1.0 without fragmentation. Strain-to-failure data for the metals tested are provided in Table 4.2.

4.7 Fragmentation Properties.

As observed in the radiographic data, an indication of the extent of fragmentation (fragment number or statistical fragment size) can be obtained, in addition to the kinematic state of the fragment debris when impact conditions exceed the breakup threshold. Methods for quantifying the the statistical fragment size and extracting fragmentation resis-

tance material property data have been described in previous reports [Kipp, *et al.*, 1993a, 1993b; Grady and Kipp, 1995]. These methods are described here with some additional analysis and used to provide fragmentation resistance property data for the metals tested in this work.

The method used for extracting fragment number and average fragment size data from radiographs of reasonable tightly packed fragment debris clouds is based on a statistical formula for randomly positioned areas [Johnson and Mehl, 1939]. The approach can be conceptualized by imagining coins of various sizes which are tossed and land at random positions on a table of a specified area A_{reg}. After N coins have been thrown the total area of interest A will be the sum of the areas of the N coins. The area of the table that is covered, however, will be less because of overlapping due to the random placement of the coins. If the area covered is A_{obs}, then the statistical theory leads to a relation between the observed area A_{obs} and the actual area A of the N coins randomly distributed on the region A_{reg},

$$A = A_{obs}\ln(1-f)^{-1/f}, \tag{4.18}$$

where $f = A_{obs}/A_{reg}$ is the fraction of the region (table) covered by coins. A Taylor expansion of Equation 4.18,

$$A = A_{obs}\left(1 + \frac{f}{2} + \frac{f^2}{3} + \cdots\right), \tag{4.19}$$

reveals that A is always greater than A_{obs} and approaches A_{obs} as f becomes small.

Application of the statistical relation in Equation 4.18 or Equation 4.19 to radiographs of fragment debris is reasonably clear. Because of shadowing and overlap of fragments in the relatively dense debris cloud, the fragment area projected on the radiographic image will be less than the projected area of the same fragments if shadowing and overlap does not occur — the latter being the desired property. Thus, image processing of the radiographic record requires two measured properties — the total observed projected fragment area A_{obs}, and an estimate of the area fraction of the debris cloud region masked by the debris fragments. Assuming a random distribution of fragments through the region, Equation 4.18 provides the required projected fragment area. Note that if f is reasonably small the expression for A is relatively insensitive to inaccuracies in f.

Knowing the total volume of fragmented material within the debris cloud from the mass and density of the initial sample, the number of fragments N and a statistical measure of the fragment size S can be determined. The method to be described differs from that used in earlier reports [Kipp, *et al.*, 1993a, 1993b; Grady and Kipp, 1995] and is believed to be an improved use of the data. The new technique leads to somewhat larger statistical fragment sizes than the earlier method.

The assumption is made that fragments in the collection of particles are nominally spherical in shape and that the distribution in size is described by the exponential distribution,

$$N = N_o e^{-m/\mu}. \tag{4.20}$$

The exponential distribution is based on a uniform strain rate random fragmentation of the sphere of mass M into N_o fragments of average fragment mass μ [Grady and Kipp, 1985]. The number of fragments of mass m within a differential range dm is

$$dN = \frac{N_o}{\mu} e^{-m/\mu} dm. \tag{4.21}$$

If the projected area (radiograph sillouette) of a fragment is a then the total projected area of fragments in this size range is $dA = adN$ or,

$$dA = \frac{N_o}{\mu}\left(\frac{3\sqrt{\pi}}{4\rho}\right)^{2/3} m^{2/3} e^{-m/\mu} dm. \tag{4.22}$$

Equation 4.22 can be integrated over the full range of particles sizes. The normalized integral is a gamma function very close to unity and consequently,

$$A = N_o\left(\frac{3\sqrt{\pi}\mu}{4\rho}\right)^{2/3}. \tag{4.23}$$

The mass of the initial spherical sample, the total number of fragments and the mean fragment mass are related through $M = N_o\mu$. Relating size and mass of the average fragment through $\mu = \pi\rho S^3/6$ one obtains the result for the average fragment size,

$$S = \frac{3}{2}\frac{M}{\rho A} \tag{4.24}$$

From an individual radiograph of the fragment debris the projected fragment area A is determined from the record and Equation 4.18 and then the statistical fragment size S through Equation 4.24. A strain rate at failure is calculated by dividing the radial expansion velocity by the initial radius of the sphere, $\dot{\varepsilon} = v_{ex}/R$. A dynamic toughness is then calculated based on the strain rate and the average fragment size through the relation,

$$K_f = \frac{\rho c \dot{\varepsilon} S^{3/2}}{\sqrt{24}}. \tag{4.25}$$

Equation 4.25, which relates a measure of the dynamic fragmentation toughness to fragment size and expansion strain rate, has been developed in an energy-based theory of dynamic fragmentation of solids [Grady, 1988].

The technique outlined above has been used to provide values for the dynamic fragmentation toughness for the metals investigated in the present study. These results are provided in Table 4.3

Table 4.3:
Fragmentation Toughness Properties of Metals

Material	K_f (MPa $m^{1/2}$)	Material	K_f (MPa $m^{1/2}$)
E52100 Steel	25-45	OFHC Copper	50-80
D6AC Steel	85-105	7075 Aluminum	15-35
AF1410 Steel	85-105	4Al6Va Titanium	60-90
SS304 Steel	80-100	Tantalum	10-30
APR Steel	55-75		

5 NUMERICAL INVESTIGATION.

Numerical techniques to model fracture and fragmentation have been reported by Kipp, *et al.* (1993a, 1993b) and Grady and Kipp (1994) for Eulerian code applications and by Johnson, *et al.* (1990) for Lagrangian code applications. In these cases, the primary theory of fragmentation is that described by Grady (1988), in which the average fragment dimension is related to the strain rate and temperature at the time of tensile fracture. If the measure of fragment size calculated for each locality in an inhomogeneous region is assumed to represent the average of a Poisson distribution, then the sum of these distributions provides an overall fragment size distribution for the fragmented solid (Kipp, *et al.*, 1993a, 1993b). To date, the fragmentation is uncoupled from the fracture process in the code; rather, a fracture model defines the material fracture, and is assumed to be prompt, so that the fragmentation does not significantly influence the course of the fracture process. The spatial extent of fragmentation is assumed to be sufficiently comprehensive that relatively large numbers of fragments are formed. Cases where a single spall forms are practical to be examined in the code, but a few large pieces are not so readily discriminated. If the majority of a region is extensively fractured, leaving behind isolated undamaged regions, we can expect that these undamaged regions will constitute discrete fragments. Other approaches to numerically simulate impact fragmentation of materials with damage models have been reported by Melosh, *et al.* (1992) and Fahrenthold and Yew (1995). Smoothed particle hydrodynamics has also been used to model fragmentation (*e.g.*, Stellingwerf and Wingate, 1993; Randles, *et al.*, 1995; Mandell, 1996).

The conditions for fragmentation are influenced by the fracture model used in the codes; some regions may experience release wave interactions that lead to traditional spall (large confining pressure, high strain rates), and other regions expand more slowly to fail in unconfined expansion. The sphere impacts described in this report have contributions to failure by both mechanisms. Consequently, the fracture model must be able to accommodate a spectrum of failure situations, with a goal to accurately define the failure conditions to be used in the fragmentation theory for local average fragment size.

The code used for the analyses reported here is CTH (McGlaun, *et al.*, 1990; Hertel, *et al.*, 1993), an Eulerian wave propagation code. The fracture model used here is that of Johnson and Cook (1985), in which a failure strain, ε^f, is accumulated whereby both spall and extensional fracture can be represented. During a calculation, an ancillary file is written that contains the strain rate, temperature, and mass at the time of fracture for each cell; this file is evaluated in a post-processing mode to define the fragment size characteristics of an event. We have assumed equiaxed fragments; hence certain explosive events, such as expanding cylindrical shells under axial detonation conditions, are not very well described by this method, since two distinctly different amplitudes of strain rate are present, a large circumferential one (small fragment dimension) and a smaller axial one (large fragment dimension), leading to the strip-like configuration observed in naturally fragmenting rounds, copper tube explosive tests, etc. These latter events can be analyzed with a discrete approach, where the deformation history of the shell is interrogated to obtain strain rates that can be used to estimate average fragment sizes as a function of position in the shell.

The fragment model as it is currently employed in CTH is summarized in Appendix A. The shock, fracture, and fragmentation material properties used in the calculations are tabulated in Appendix B. The sources of these properties are primarily Steinberg (1994; 1996), Grady (1995), and Marsh (1980).

The numerical simulations described in this section are intended to provide both insight into the impact experiments documented earlier in this report, and an evaluation of the code in these fracture and fragmentation applications. Five areas are addressed, selecting appropriate experiments from a selection of the materials tested: (1) determine projectile shape after a subcritical impact with a target plate; (2) obtain a mass weighted average plastic strain, also for the subcritical cases, to compare with the technique used in Section 4 to estimate deformational strain; (3) obtain mass vs. strain rate for the fragmented sphere, and compare this with the global average strain rate estimated from the expansion rates; (4) determine average fragment size for impact events, and compare with estimates from Section 4; and (5) calculate axial velocity decrement, radial expansion rates, and fragment debris trajectories resulting from impact. Where appropriate, related observations pertaining to the nature of the pulses transmitted to the sphere and the underlying mechanisms of the trailing debris observed in some of the experiments will be interjected.

Several of the tests on 7075-T6 aluminum were selected for computational analysis. An extensive series of experiments and accompanying analyses were reported for a hardened steel by Kipp, *et al.* (1993a, 1993b). An additional study should be made to explore the properties and behavior that characterize all the steel data reported in this report. Copper impacts have been previously considered by Grady and Kipp (1994) in which the copper sphere was made to impact a hardened steel target plate of thickness comparable to the copper ball diameter. The impulse sustained by the copper at incident velocities of approximately 4 km/s in that configuration was sufficient to form a hollow debris shell containing both steel and copper materials. Extensive experimental results, particularly high quality radiography and witness plate data, have also been reported by Horz, *et al.* (1995) and Piekutowski (1995) for these kinds of debris clouds. Debris clouds comprised of such finely comminuted material are in contrast to the impulse imparted by the present relatively thin low impedance targets which cause the fragments to be distributed rather uniformly throughout the region typically characterized by an expanding cylindrical disk.

The experiments that were numerically simulated were chosen on the basis of threshold responses to impact conditions:

5.1 Sub-Threshold Deformation Profiles.

Two aluminum sphere impact cases are used to illustrate the approach taken in the numerical analyses: a non-fragmenting (subcritical) impact (2230 m/s onto 2.92 mm PMMA), and a fragmenting impact (3920 m/s onto 2.92 mm PMMA). The calculated velocity decrement for the subcritical impact was 310 m/s resulting in a residual velocity of 1920 m/s, which is within 2% of the experimentally determined residual velocity of 1880 m/s. For this impact, the pressure at the contact point is 9 GPa, which decays nearly linearly in tran-

sit through the sphere to an amplitude of 1 GPa near the trailing surface of the sphere; the transit time is about 1.2 μs. The calculated velocity decrement for the fragmenting impact was 650 m/s, resulting in a residual velocity of 3270 m/s, which is within 1% of the experimentally determined residual velocity of 3310 m/s. For this higher velocity impact, the pressure at the contact point is nearly 20 GPa, which also decays nearly linearly during transit through the sphere to an amplitude of 1 GPa near the trailing surface of the sphere; the transit time is about 1 μs.

The final deformation of the aluminum sphere calculated for the subcritical impact velocity (2230 m/s) is shown in Figure 5.1a, accompanied by the experimental result, Figure 5.1b. (The diameter of the deformed experimental sphere is 7.7 mm.) Fringes have formed on the periphery of the simulation that do not appear in the experimental radiograph.

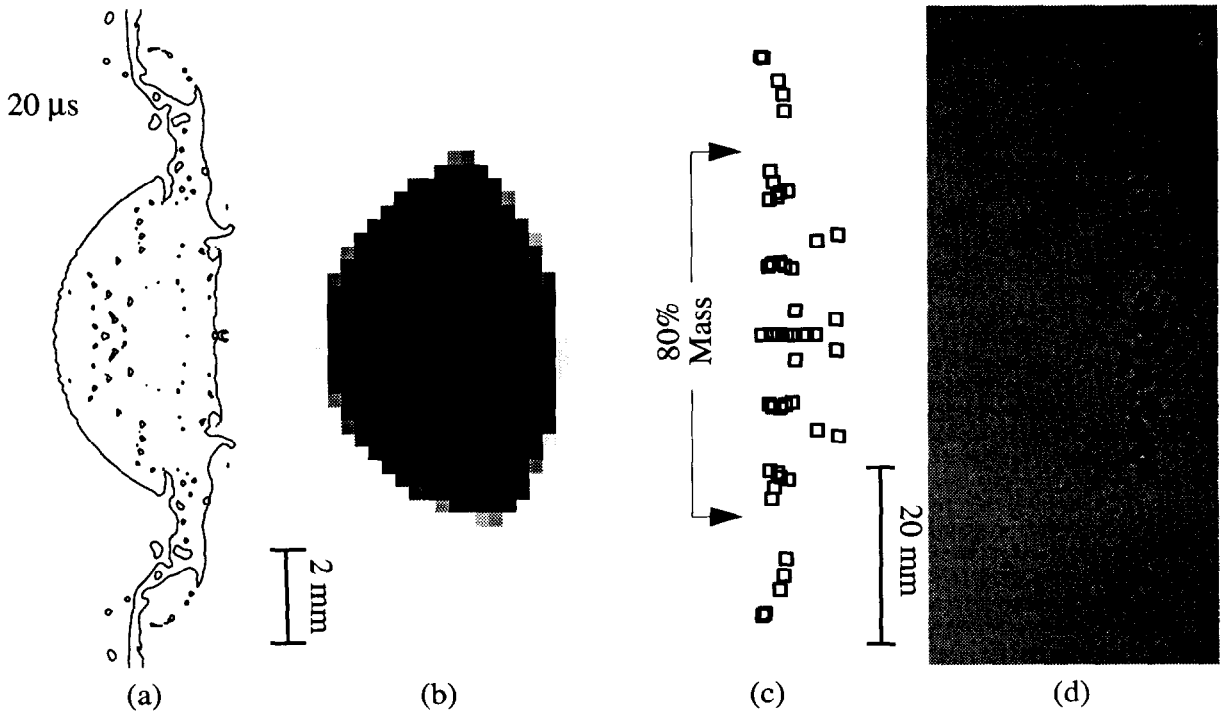

Figure 5.1. Comparison of numerical (a) and experimental (b) deformed aluminum spheres for 2230 m/s impact onto 2.92 mm PMMA. Comparison of extrapolated fragments (c) and experimental (d) debris cloud for 3920 m/s impact onto 2.92 mm PMMA.

5.2 Average Plastic Deformational Strain.

The average plastic strain undergone by the sphere during a subcritical impact can be determined from the calculation integrating the mass-weighted local plastic strain over the volume of the metal sphere after the loads from the impact event have decayed to elastic amplitudes.

Note that internal spall and cracking can influence the apparent plastic strain measure, and would not be visible in radiographs of the event. A calculated value of the strain measure,

$\varepsilon = 1 - l/2R$, is 0.47, which is considerably larger than the strain value of 0.22 obtained from the radiograph for this particular experiment (Figure 5.1b), but quite close to the critical experimental value of 0.42 (Tables 4.1 and 4.2). The calculation required an elapsed time of 20 μs before the total equivalent plastic strain for the aluminum reached a steady amplitude of about 0.9 (obtained by mass weighting the equivalent plastic strain summed over all aluminum cells). Although this value is much larger than the experimental value, there is a substantial plastic strain in the fringe material; when the total equivalent plastic strain is determined from the main part of the deformed sphere, the value is about 0.52, which is consistent with the calculated value using the strain measure based on the permanent axial deformation. In contrast to the long time to equilibrium for the plastic strain, the change in axial (average) velocity is complete by about 4 μs after impact. It should also be noted that the calculation indicates the formation of damage within the deformed aluminum sphere (Figure 5.1a), structure not discernible in the radiograph; hence the threshold impact velocity needs to be primarily associated with the onset of fragmentation, since the sphere in a subcritical impact may in fact sustain severe internal damage, but retain sufficient overall integrity to hold all its mass together in a unit that has no radial expansion velocity.

5.3 Fragment Size Estimates.

The calculation for the aluminum sphere impact at the higher velocity (3920 m/s) results in nearly complete fragmentation of the aluminum. The velocity attributes of tracer particles located in the aluminum are utilized to convect their locations from 9 μs, the time at which the calculation was terminated, to 53 μs (Figure 5.1c), a time corresponding to an experimental radiograph at the first image position (Figure 5.1d). The diameter of the primary cloud of fragments in the radiograph (Figure 5.1d) is about 37 mm. The tracer locations appear to be more dispersed both radially and axially than the radiographic image indicates, although the central five main clusters of tracers, which comprise 80% of the aluminum sphere mass, have a radial dimension which is similar to the experiment (Figure 5.1c and Figure 5.1d); the calculated radial expansion velocity of this envelope is about 290 m/s, which compares well with the measured expansion velocity of 281 m/s. The calculated radial expansion velocity of the outer dispersed material is well in excess of 500 m/s.

Fragment size characteristics were determined from a cell-by-cell fragmentation analysis using a quasistatic fracture toughness value of 30 MPa $m^{1/2}$ [Kobayashi, 1973], which is within the range obtained for aluminum from the current fragmentation experiments, as listed in Table 4.3. The resulting fragment size distributions are shown in Figure 5.2, where the bar graph represents the mass distribution of fragments summed from all the cells, and the smooth curve has Poisson statistics applied to the bar distribution [Kipp, *et al.* 1993a, 1993b]. The average fragment size determined from this statistical fragmentation analysis is about 0.8 mm. The extremes of the measured fracture toughness, 15 and 35 MPa $m^{1/2}$ (Table 4.3), yield average fragment sizes of 0.5 and 0.8 mm, respectively, from the numerical simulations. The average calculated strain rate (determined by mass weighting the strain rate at the time of fracture summed over all aluminum cells) is about 6×10^5 s^{-1}. In the particular experiment considered here for

aluminum impact at 3920 m/s onto 2.92 mm PMMA, the measured expansion strain rate, $\dot{\varepsilon} = v_{ex}/R$, was 9×10^4 s^{-1}. Characteristic fragment sizes discernible on the radiographic images ranged from a minimum of 0.4 mm to a maximum of about 1.5 mm. The numerical simulation includes fractures that have occurred by spallation as well as circumferential expansion. Consequently, as spallation strain rates tend to be much larger than circumferential strain rates, the average strain rate in the aluminum determined numerically is expected to be larger than that obtained based on expansion alone, and the calculated average fragment sizes will be smaller.

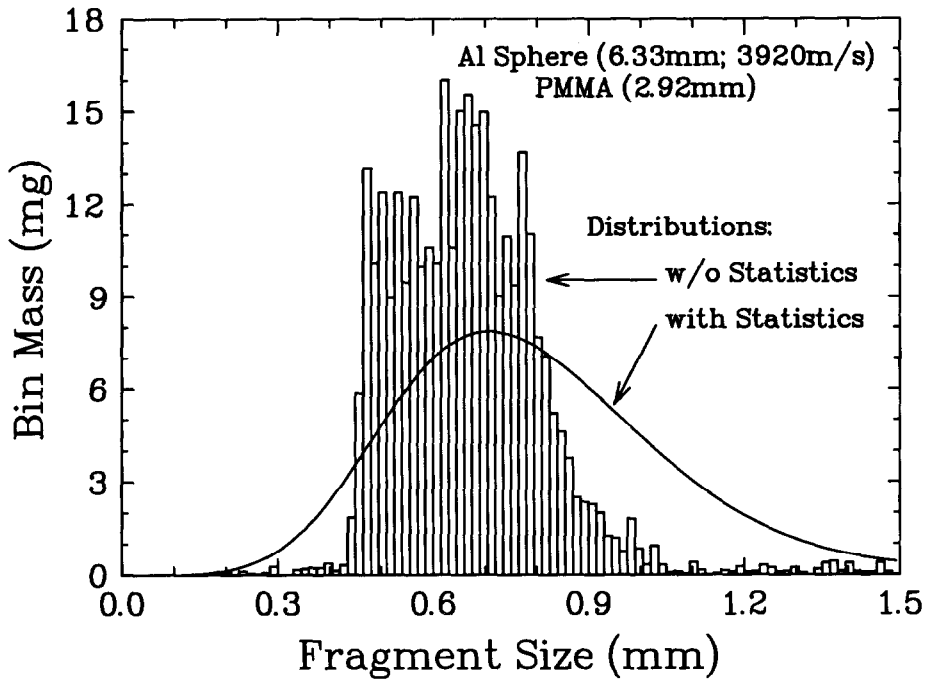

Figure 5.2. Fragment size distributions of aluminum sphere after impact with a PMMA target (from numerical simulation).

6 DISCUSSION.

The impact-induced fragmentation of materials involved in ballistic events has become a recognized concern in a range of applications and there has been a concerted effort to develop analytic and computational models capable of predicting the features of dynamic fragmentation events. These models are in need of the underlying material properties which control the failure and fragmentation of matter within the intense deformation environment of a high-velocity impact event. These models are still tentative and a clear understanding of the necessary material properties is still emerging.

Dynamic fracture data and corresponding properties can be obtained from reasonable mature test methods such as planar impact spall tests or tensile Hopkinson bar tests. Application of these properties is uncertain, however, due to the relatively youthful state of dynamic fragmentation models. When models are uncertain it is best to use material testing methods which exercise the material as closely as possible to the applications of interest. That was the goal of the present test method.

Considerable progress in development of the sphere-on-plate fracture, failure and fragmentation material property test has been made. Heightened understanding of the impact loading that leads to failure and fragmentation of the sample has been made through analytic and computational analysis.

One objective was an attempt to extract model independent material property data from the test data. This was only partially successful and further study here is required. Several methods were investigated to extract the energy that the sample could absorb before failure onset. This was accomplished but with a fairly strong dependence on the method of analyzing the data and an uncomfortable difference between the two methods which were developed. Useful strain-to-failure data was provided by the test method and beneficial fragmentation resistance property data within the context of an energy-based theory of fragmentation was obtained.

Although a study of scale dependence, in which spherical samples of different sizes are tested, was not undertaken in this program, past experience suggests that some scale dependence of the strain-to-failure and fragmentation character would be expected. In the present dynamic tests size scale is not independent of strain rate. With other parameters remaining constant, a decrease in sample size will lead to a corresponding increase in strain rate. From other dynamic failure studies an agreement with energy scaling in which failure proportional to an inverse square root of sample size would not be unexpected.

This experimental fracture material property test method to evaluate dynamic fragmentation provides a means for discerning fragmentation thresholds and determining an average measure of the fracture toughness. These experimental data also provide a standard for numerical simulation evaluation. The current simulations capture the axial velocity changes accurately, but overpredict both the deformation of the unfragmented sphere and the dispersion of the debris for the fragmention cases discussed. Average fragment sizes determined with the simulations appear to be smaller than the dominant size observed in

the radiographs, but further detailed analysis of the radiographic data and comparisons with computations need to be pursued.

7 REFERENCES

Ang, J. A., (1990) Impact Flash Jet Initiation Phenomenology, *Int. J. Impact Engng*, 10, 23-33.

Brown, W. K. (1989) Fragmentation of the Universe, *J. Astrophys. Astr.*, 10, 89-112.

Chhabildas, L. C., L. M. Barker, J. R. Asay and T. G. Trucano, (1990) Spall Strength Measurements on Shock-Loaded Refactory Metals, Shock Compression of Condensed Matter — 1989, edited by Schmidt et al., Elsevier Science Publishers, p. 429-432.

Englman, R., Z. Jaeger, and A. Levi (1984) Percolation Theoretical Treatment of Two-Dimensional Fragmentation in Solids. *Phil. Mag. B*, 50, 307-315.

Fahrenthold, E. P. and C. H. Yew (1995) Hydrocode Simulation of Hypervelocity Impact Fragmentation, *Int. J. Impact Engng*, 17, 303-310.

Furnish, M. D., L. C. Chhabildas and D. J. Steinberg (1994) Dynamic Behavior of Tantalum, High Pressure Science and Technology — 1993, edited by S. C. Schmidt et al., Am. Inst. Phys., p. 1849-1852.

Glenn, L. A. and A. Chudnovsky (1986) Strain Energy Effects on Dynamic Fragmentation. *J. Appl. Phys.*, 59, 1379-1380.

Grady, D. E. (1982) Local Inertia Effects in Dynamic Fragmentation. *J. Appl. Phys.*, 53, 322-325.

Grady, D. E. (1988) The Spall Strength of Condensed Matter. *J. Mech. Phys. Solids*, 36, 353-384.

Grady, D. E. (1990) Particle Size Statistics in Dynamic Fragmentation. *J. Appl. Phys.*, 68, 6099-6105.

Grady, D. E. (1993) Spall and Fragmentation in High-Temperature Metals, Sandia National Laboratories Report SAND93-3266, February.

Grady, D. E. (1995) Dynamic Properties of Ceramic Materials, Sandia National Laboratories Report SAND94-3266, February.

Grady, D. E. and M. E. Kipp (1985) Geometric Statistics and Dynamic Fragmentation, *J. Appl. Phys.*, 58, 1210-1222.

Grady, D. E. and M. E. Kipp (1994) Experimental and Computational Simulation of the High Velocity Impact of Copper Spheres on Steel Plates, *Int. J. Impact Engng*, 15, 645-660.

Grady, D. E. and M. E. Kipp (1995) Experimental Measurement of Dynamic Failure and Fragmentation Properties of Metals, *Int. J. Solids Structures*, 32, 2779-2792.

Hertel, E. S., *et al.* (1993) CTH: A software Family for Multi-Dimensional Shock Physics Analysis, Proceedings of the 19th International Symposium on Shock Waves, Volume 1, 377-382, Edited by R. Brun and L. D. Dumitrescu, Marseille, France 26-30 July 1993.

Horz, F., *et al.* (1995) Penetration Experiments in Aluminum 1100 Targets Using Soda-Lime Glass Projectiles, NASA Technical Memorandum 104813, June 1995.

Johnson, W. A. and R. F. Mehl (1939) Reaction Kinetics in Processes of Nucleation and Growth. *Trans. A. I. M. M. E.*, 135, 416-458.

Johnson, G. R. and W. H. Cook (1985) Fracture Characteristics of Three Metals Subjected to Various Strains, Strain Rates, Temperatures, and Pressures, *Engineering Fracture Mechanics*, 21, 31-48.

Johnson, G. R., R. A. Stryk, T. J. Holmquist, and O. A. Souka (1990) Recent EPIC Code Developments for High Velocity Impact: 3D Element Arrangements and 2D Fragment Distributions. *Int. J. Impact Engng.*, 10, 281-294.

Kerley, G. I. and T. L. Christian-Frear (1993) Sandia Equation of State Data Base: seslan File, Sandia National Laboratories Report SAND93-1206, June.

Kipp, M. E. and D. E. Grady (1985) Dynamic Fracture Growth and Interaction in One Dimension. *J. Mech. Phys. Solids*, 33, 399-415.

Kipp, M. E., D. E. Grady and J. W. Swegle (1993a) Experimental and Numerical Studies of High-Velocity Impact Fragmentation, Sandia National Laboratories Technical Report SAND93-0773, August.

Kipp, M. E., D. E. Grady, and J. W. Swegle (1993b) Numerical and Experimental Studies of High-Velocity Impact Fragmentation, *Int. J. Impact Engng*, 14, 427-438.

Kipp, M. E. (1994) Target Response to Debris Cloud Incidence, High Pressure Science and Technology — 1993, edited by S. C. Schmidt et al., Am. Inst. Phys., p. 1849-1852.

Kobayoshi, A. J. (1993) Experimental Techniques in Fracture Mechanics, SESA.

Mandell, D. A. (1996) Personal communication.

Marsh, S. P. (1980) LASL Shock Hugoniot Data, University of California Press, Berkeley.

McGlaun, J. M., S. L. Thompson, and M. G. Elrick (1990) CTH: a Three-Dimensional Shock Wave Physics Code, *Int. J. Impact Engng*, 10, 351-360.

Melosh, H. J., E. V. Ryan, and E. Asphaug (1992) Dynamic Fragmentation in Impacts: Hydrocode Simulation of Laboratory Impacts, *J. Geophys. Res. - Planets*, 97, No. E9, 14,735-14,759.

Piekutowski, A. J. (1995) Formation and Description of Debris Clouds Produced by Hypervelocity Impact, University of Dayton Research Institute Report UDR-TR-95-46, May.

Randles, P. W., T. C. Carney, L. D. Libersky, J. D. Renick, and A. G. Petschek (1995) Calculation of Oblique Impact and Fracture of Tungsten Cubes Using Smoothed Particle Hydrodynamics, *Int. J. Impact Engng*, 17, 661-672.

Steinberg, D. L. (1994) Computer Studies of the Dynamic Strength of Ceramics (II), Proceedings of EURODYMAT 94, Oxford, U.K., September 26-30, 1994.

Steinberg, D. L. (1996) Equation of State and Strength Properties of Selected Materials, Lawrence Livermore National Laboratories Report UCRL-MA-106439 (Change 1), February.

Stellingwerf, R. F. and C. A. Wingate (1993) Impact Modeling with Smooth Particle Hydrodynamics, *Int. J. Impact Engng*, 14, 707-718.

8 APPENDIX A- Summary of Fragmentation Theory

A capability has been developed to produce fragment size predictions from calculations using wave propagation codes that solve the equations expressing conservation of mass, momentum, and energy for a continuum. Although plots produced from standard wavecode calculations sometimes appear to depict a collection of discrete fragments, the physical mechanisms that control these processes, such as surface tension or real physical heterogeneities and microstructure, are not currently included in the codes. Previous work (Grady, 1988) has produced dynamic fragmentation theories that are based on the assumption that strain rate and temperature at the time of failure control subsequent fragmentation.

The wavecode from which strain rate and temperature are extracted at the time of fracture is the Eulerian finite-difference shock wave propagation code CTH (McGlaun, *et al.*, 1990). This code has a general internal state variable capability which allows information to be saved in variables that are advected with the material as it crosses the cell boundaries. Significant modifications were made to the fracture algorithm in the code to locate each time and position at which the tensile stress criterion for a single material, rather than a mixed-material cell, was exceeded and material fracture was judged to occur. All diagonal components of the strain-rate tensor,

$$\dot{\varepsilon}_i = \frac{\partial v_i}{\partial x_i}, \tag{A1}$$

including the hoop component in cylindrical coordinates,

$$\dot{\varepsilon}_R = \frac{v_R}{R}, \tag{A2}$$

where v_i and x_i are velocity and position components and R refers to radius, were then calculated and the maximum value was stored as an internal state variable. While the internal state variables provide storage locations for the strain rate and temperature information that must be saved from the calculation, there is a problem with diffusion of these quantities as material motion occurs. For instance, even though a calculation may be performed in which only a single fracture of a material cell takes place during the entire calculation, subsequent material motion may result in spurious values of strain rate appearing in all cells through which the material has passed. Fortunately, these values typically have a very small magnitude except in the region of the mesh containing the bulk of the fractured material. However, diffusion does result in some spreading and loss of localization of the fractured material, so extreme care was taken to assess such effects and ensure that reasonable fragment size distributions were obtained. Since most fractures occurred at high strain rates on the order of 10^3 to 10^6 per second, it was possible to discard significantly lower strain rates as having been produced by diffusion. Mass fraction weighting was used to maintain the proper convected amplitudes of the strain rates and temperatures. Files containing strain rate and temperature at the time of fracture are saved periodically during the simulation of the impact, and these are examined to determine the extent of the fractured regions as time progressed. When the fracture process is complete, the data are

post-processed outside the wavecode to produce fragment size distributions. Dynamic fragmentation theories predict an average local fragment size at a given strain rate and temperature, and the number of fragments with this average size is determined by the local mass of the material that fractures.

The dynamic fragmentation theories that were used to process the strain rate and temperature information have been described in detail elsewhere (Grady, 1988; Kipp, *et al.*, 1993a; Kipp, *et al.*, 1993b), and they will only be summarized here. Various types of fragmentation mechanisms have been identified, depending on the strain rate and temperature at fracture. The temperature and density data can also be evaluated with the equation of state to determine the mass distribution of fractured material in the solid, liquid, and vapor phases.

For the present purposes, the average fragment size S will be determined in three different fragmentation regimes. These are:

(1) solid spall dominated by fracture toughness, for which

$$S = \left(\frac{\sqrt{24}K_c}{\rho c \dot{\varepsilon}}\right)^{2/3}, \tag{A3}$$

(2) solid spall dominated by the flow stress, for which

$$S = \left(\frac{8Y\varepsilon_C}{\rho \dot{\varepsilon}^2}\right)^{1/2}, \tag{A4}$$

and (3) liquid spall above the melt temperature, for which

$$S = \left(\frac{48\gamma}{\rho \dot{\varepsilon}^2}\right)^{1/3}. \tag{A5}$$

In these equations, ρ is the density, $\dot{\varepsilon}$ is the strain rate, c is the sound speed, ε_C is a critical strain, usually taken to be 0.15. The temperature and strain rate dependent yield strength, Y, is given by

$$Y = Y_0\left(1 - \frac{T - T_{ref}}{T_m - T_{ref}}\right)^{n_Y}\left(\frac{\dot{\varepsilon}}{\dot{\varepsilon}_0}\right)^{m_Y}, \tag{A6}$$

the temperature dependent fracture toughness, K_c, is given by

$$K_c = K_{c0}\left(1 - \frac{T - T_{ref}}{T_m - T_{ref}}\right)^{n_K}, \tag{A7}$$

and the temperature dependent surface tension, γ, is given by [Grady, 1993],

$$\gamma = \sigma_0\left(1 - \frac{T}{T_C}\right)^{n_\sigma - 1}\left(1 + (n_\sigma - 1)\frac{T}{T_C}\right), \tag{A8}$$

where Y_0 is the reference yield strength, K_{c0} is the reference fracture toughness, σ_0 is the reference surface tension, T is the temperature, T_m is the melt temperature, T_{ref} is the reference temperature, $\dot{\varepsilon}_0$ is a reference value of the strain rate (one per second), T_C is the critical temperature, and n_Y, m_Y, n_K, and n_σ are constants. In the solid regime, the transition from fracture toughness to flow stress dominated spall occurs at a strain rate given by

$$\dot{\varepsilon}_t = \sqrt{\frac{0.003\rho c^4 Y^3}{K_c^4}}. \tag{A9}$$

Material properties are required for the fragmentation regimes of brittle, ductile, and liquid spall. Application of the above formulas allows each point in the strain rate - temperature plane to be mapped into a fragment size for a given material.

The fragmentation theories described above are derived assuming spall induced by uniform volumetric dilatation, so they are most applicable to cases of prompt fragmentation. The possibility of fracture at lower strain rates is included in the fracture model, however, where the material may fail after extended strain at stresses much lower than the spall stress, particularly in region at the periphery of a sphere, for example.

To obtain the fragment size distribution from the analysis, files are generated by the wavecode calculations that contain the strain rate and temperature at the time of fracture for each cell containing fractured material. There is thus a mass associated with each strain rate - temperature pair, which is just the total mass, m, of the material in the cell. The simplest assumption to make when determining fragment size distributions is that all of the mass in the cell produces particles of equal size S, determined from equations 3, 4, or 5. Thus, letting i be the cell index, where $i = 1, \ldots N$ and N is the total number of cells containing fractured material, the cell data consist of N pairs m_i, S_i where m_i is the mass of material in cell i and S_i is the size of all the particles in the cell. If the data are arranged in order of increasing fragment size, so that $S_i \leq S_{i+1}$, then the cumulative mass of fragments less than or equal to size S_i is

$$M(S_i) = \sum_{j=1}^{i} m_j \tag{A10}$$

However, as previously described (Grady and Kipp, 1985), statistical considerations indicate that a distribution of fragment sizes should be determined about the mean fragment size calculated for each cell, S_i. The form of the distribution is obtained by assuming that fragments in the mass m_i are Poisson-distributed. This leads to a probability distribution of finding a fragment of mass μ in the cell within a tolerance $d\mu$ given by

$$dP(\mu) = \frac{1}{\mu_a} e^{-\mu/\mu_a} d\mu \,, \tag{A11}$$

where μ_a is the average, or mean, value of the fragment mass in the cell. Integrating from 0 to μ and multiplying by the total mass m_i of the cell gives the cumulative mass of fragments of mass less than or equal to μ in the cell

$$M(\mu) = m_i[1 - e^{-\mu/\mu_a}] \,. \tag{A12}$$

Now, assuming that the mass of the fragment is related to the cube of the fragment size (such as for cubic or spherical particles) and noting that the average mass μ_a corresponds to a fragment having the average size S_i,

$$\frac{\mu}{\mu_a} = \left(\frac{S}{S_i}\right)^3 \,. \tag{A13}$$

Therefore, the cumulative mass of fragments in cell i having a size less than or equal to S is

$$M(S) = m_i[1 - e^{-(S/S_i)^3}] \,. \tag{A14}$$

Finally, the total cumulative mass of all fragments in all cells having a size less than or equal to S is

$$M_T(S) = \sum_{i=1}^{N} m_i[1 - e^{-(S/S_i)^3}] \,. \tag{A15}$$

It was found that if the original distribution (10) is sharply peaked, a large spread is generated by the statistical relations. However, if the original distribution already contains a large range of fragment sizes, the additional statistical spread is minimal. The statistical distributions do show the addition of a tail at small, possibly aerosol-sized, fragments, but the total additional mass in the aerosol source term so generated is negligible. In application, the cell data is grouped into "bins" of a chosen fragment size increment.

The spectral distribution in size, corresponding to Equation 11, is

$$dP(S) = 3\frac{S^2}{S_i^3} e^{-(S/S_i)^3} dS \,. \tag{A16}$$

The original distribution of average sizes can be depicted as in Figure A1a, where each bin contains the number of fragments, N_i, of an average fragment size, S_i. These parameters are used in Figure A1b to define the associated statistical distribution for that particular bin, as represented in Figure A1b. All of these statistical distributions are summed to obtain the final statistical distribution of fragment sizes for the event. Note that although the distribution is exponential in mass, it is exponential in the cube of the size, and the result-

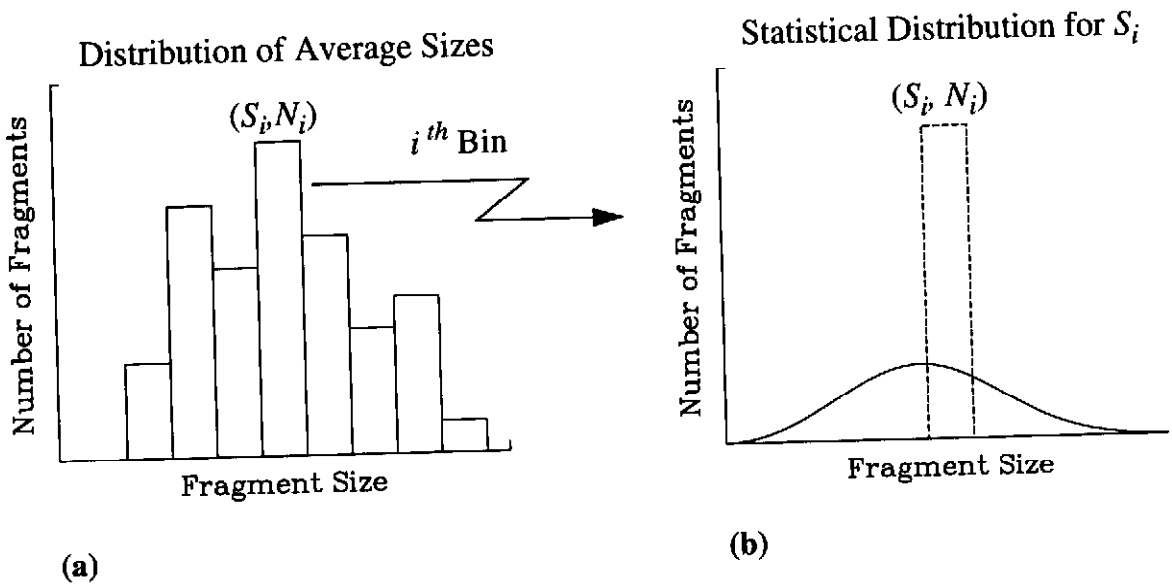

Figure A1. Process of transforming the original fragment size distribution to a statistical fragment size distribution.

ing coefficient in 16 contains the square of the size, leading to the character of the statistical distribution in Figure A1b.

9 APPENDIX B - Summary of Material Parameters

This appendix contains a summary of the equation of state, deviatoric model, and fracture parameters used in the wavecode calculations, and the parameters used in the fragmentation analyses.

Table B1: Material Parameters Used For Calculations (Projectiles)

	7075-T6 Aluminum	OFHC Copper	304SS	Tantalum
Density (kg/m^3)	2804	8930	7900	16654
Bulk sound speed (m/s)	5200	3940	4569	3414
Linear shock velocity - particle velocity slope	1.360	1.489	1.490	1.201
Gruneisen coefficient	2.20	1.99	1.93	1.60
Yield strength (GPa)	0.42	0.12	0.34	0.77
Poisson ratio	0.33	0.290	0.298	0.34
Johnson-Cook, D2	0.10	3.10	0.632	2.71
Johnson-Cook, D3	-0.46	-0.27	-0.275	-0.67
Fracture stress (GPa)	1.5	2.3	4.0	5.3
Specific Heat (ergs/g-eV)	1.1×10^{11}	4.6×10^{10}	5.2×10^{10}	1.6×10^{10}
Tmelt (eV)	0.11	0.12	0.16	0.28

Table B2: Material Parameters Used For Calculations (Targets)

	PMMA	Fused Silica	Alumina Al_2O_3
Density (kg/m^3)	1186	2201	3.948
Bulk sound speed (m/s)	2598	5060	7970
Linear shock velocity - particle velocity slope	1.516	-	1.27
Gruneisen coefficient	0.97	-	1.31
Yield strength (GPa)	0.42	7.9	8.0
Poisson ratio	0.37	0.08	0.236
Fracture stress (GPa)	0.15	4.0	5.0
Specific Heat (ergs/g-eV)	1.0×10^{10}	1.0×10^{10}	1.0×10^{10}
Tmelt (eV)	0.04	0.25	0.25

Note that for fused silica, a tabular equation of state was used (Kerley and Christian-Frear, 1993) in order to accomodate the complexities of this material; there is no adequate linear shock-velocity particle-velocity representation of the glass over the pressure regime that occurs in the present experiments.

Table B3: Fragmentation Material Properties

	7075-T6 Aluminum	OFHC Copper	304SS	Tantalum
Density ρ (kg/m^3)	2804	8930	7900	16654
Sound Speed c (m/s)	5200	3940	4569	3414
Melt Temperature T_m (K)	1220	1356	2380	3269
Fracture Toughness K_{c0} (MPa m$^{1/2}$)	23	300	100	100
n_K	-1	0	-1	0
Yield Strength Y_0 (GPa)	0.42	0.12	0.34	0.77
n_Y	1.5	1	1	1
m_Y	0.02	0	0.1	0
ε_C	0.15	0.15	0.15	0.15
Surface Tension σ_0 (N/m)	1.188	1.975	2.94	3.658
Critical Temperature T_C (K)	5220	5330	6330	11080
n_σ	1.33	1.27	1.34	1.52

10 APPENDIX C - Radiographic Records

Radiographs for all of the tests performed in the current series of experiments are found in the present appendix. For each test series (material) a calibration radiograph was taken of a horizontal and vertical leaded ruler placed in the plane of the projectile subsequent fragment debris trajectory. X-ray and film position were maintained constant through the test series. The calibration records combined with the test parameters provided in the tables of Section 3 are sufficient to orient the two fragment debris images in time and space.

NOTE: In all of the following radiographs, motion proceeds from the bottom of the page towards the top of the page.

TEST CU-5

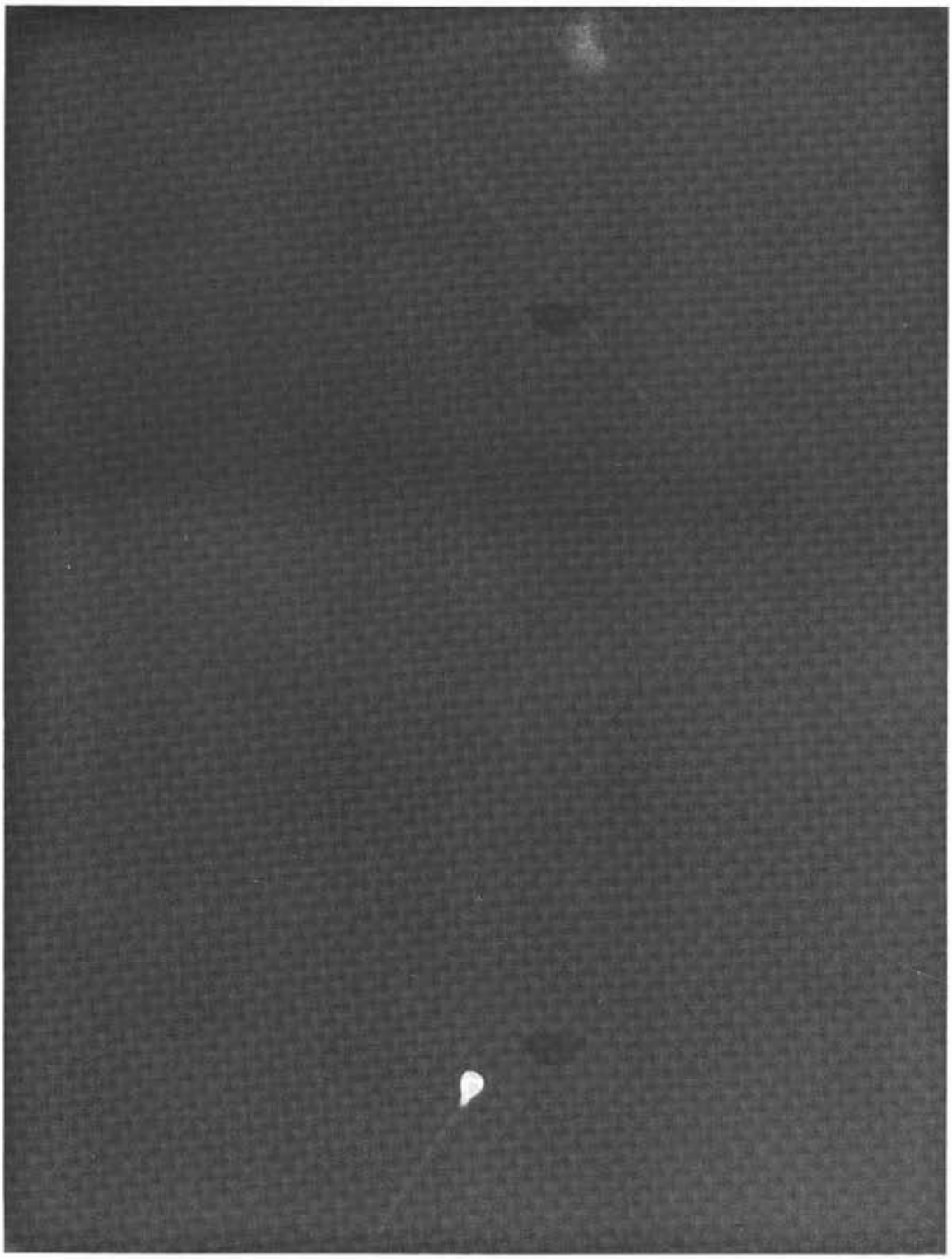

TEST CU-6

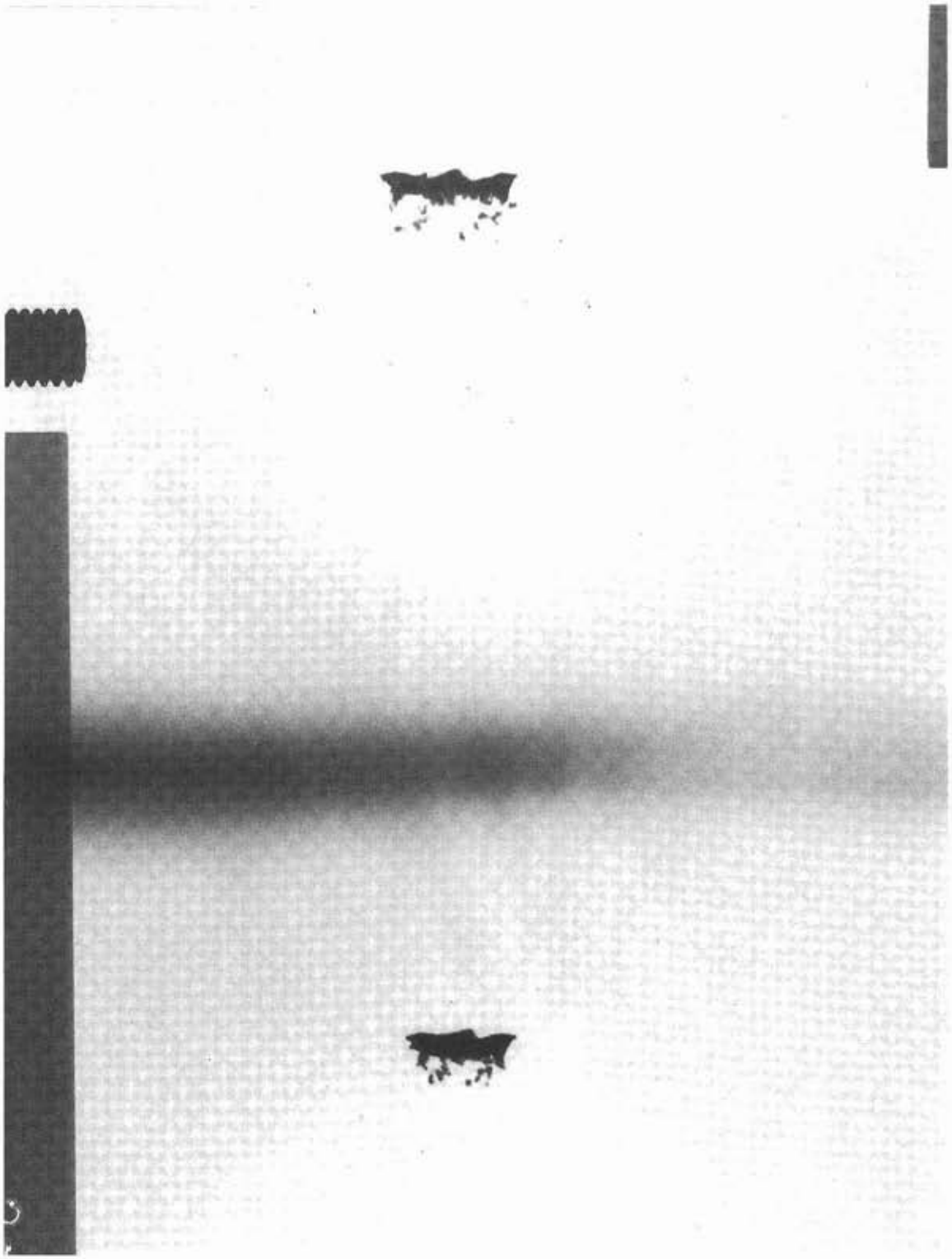

TEST CU-7

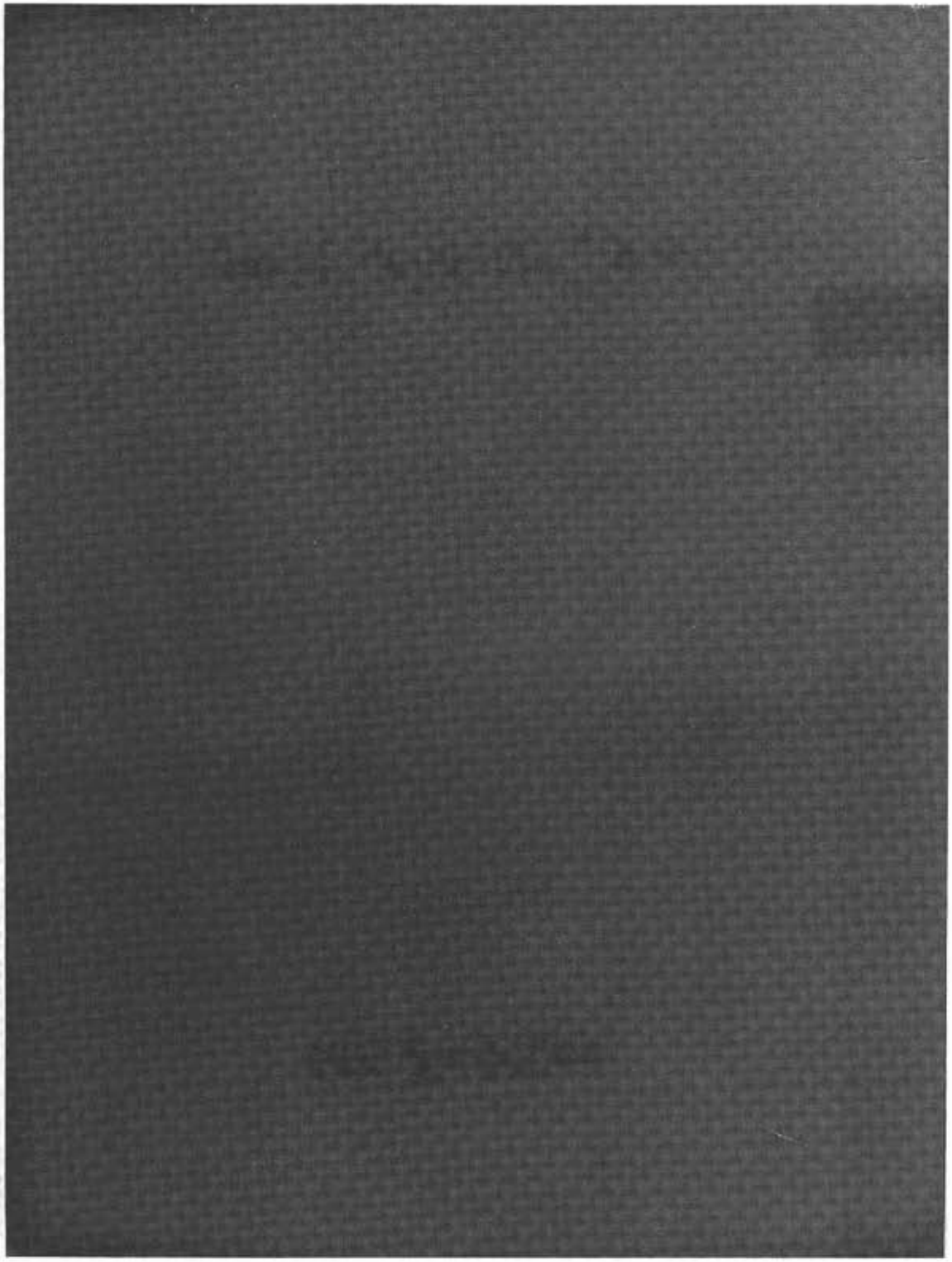

TEST CU-8

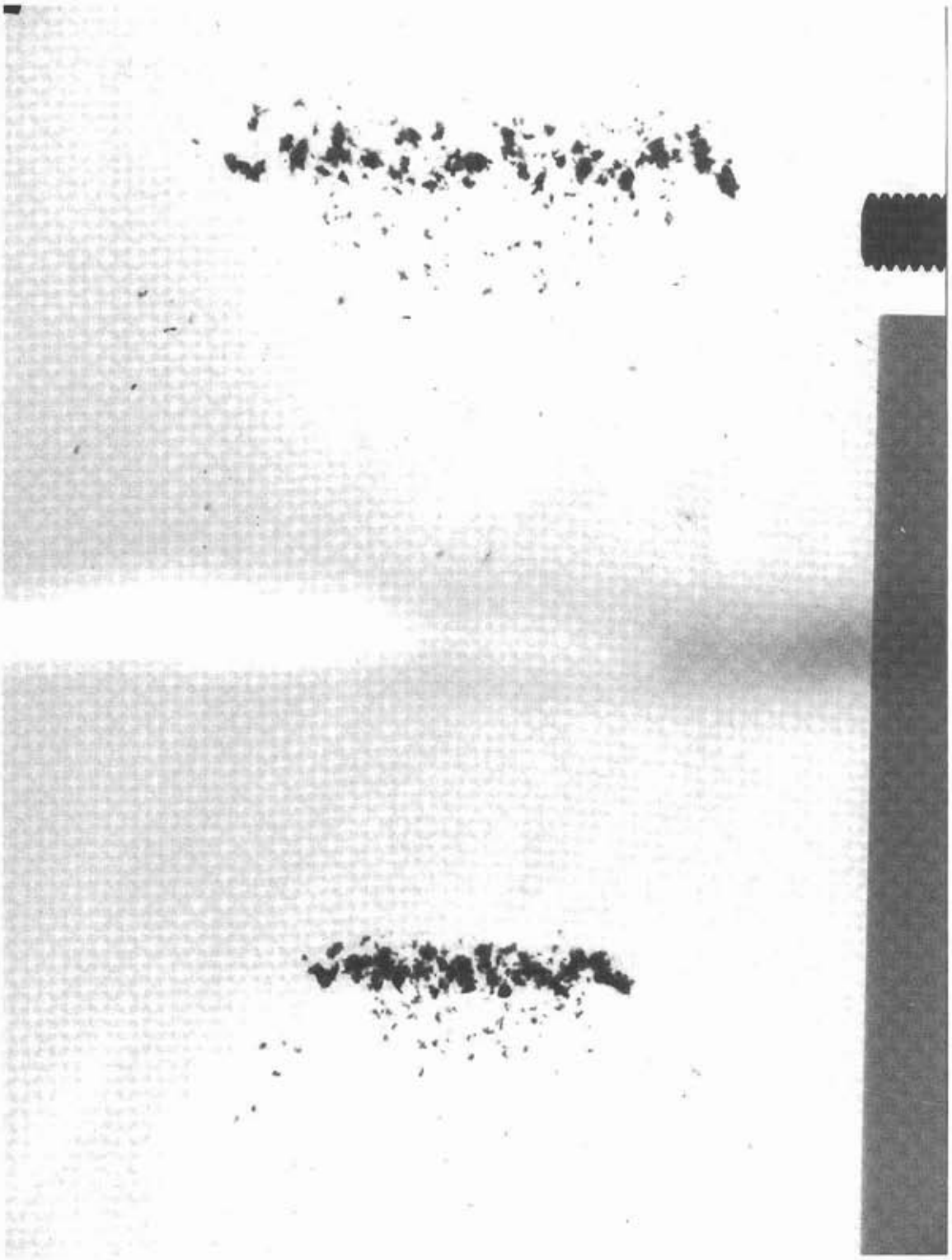

TEST CU-9

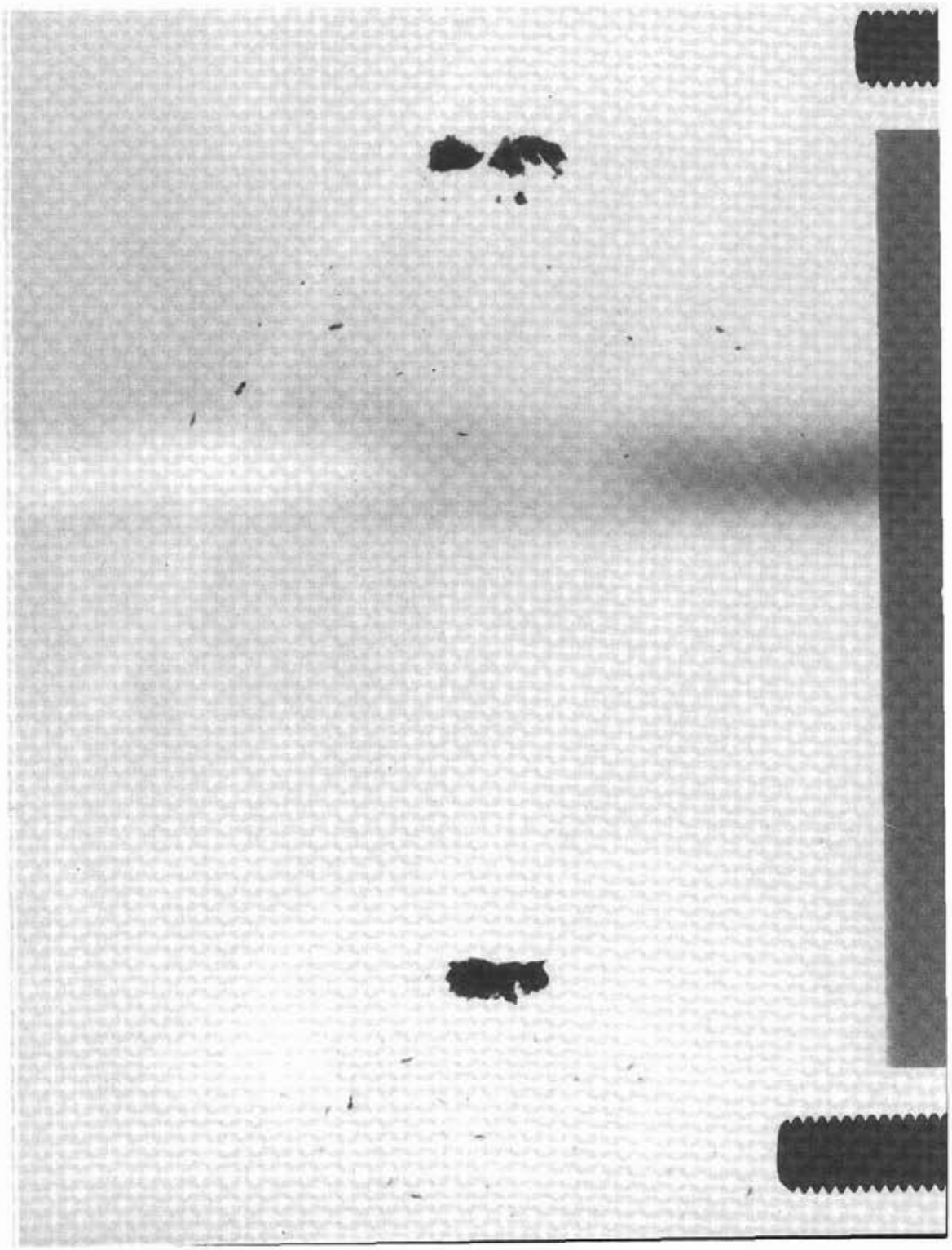

TEST CU-10

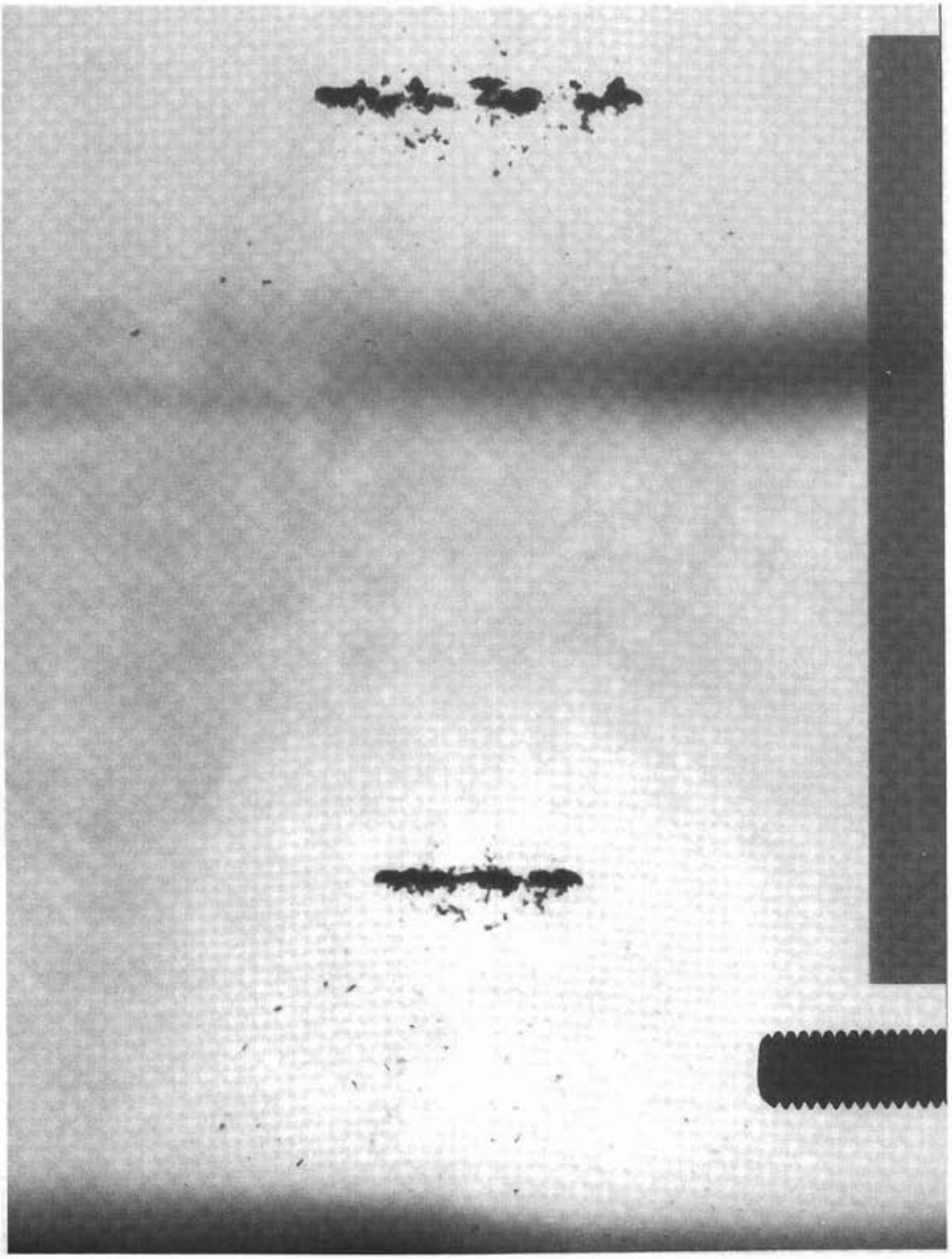

CU - Calibration

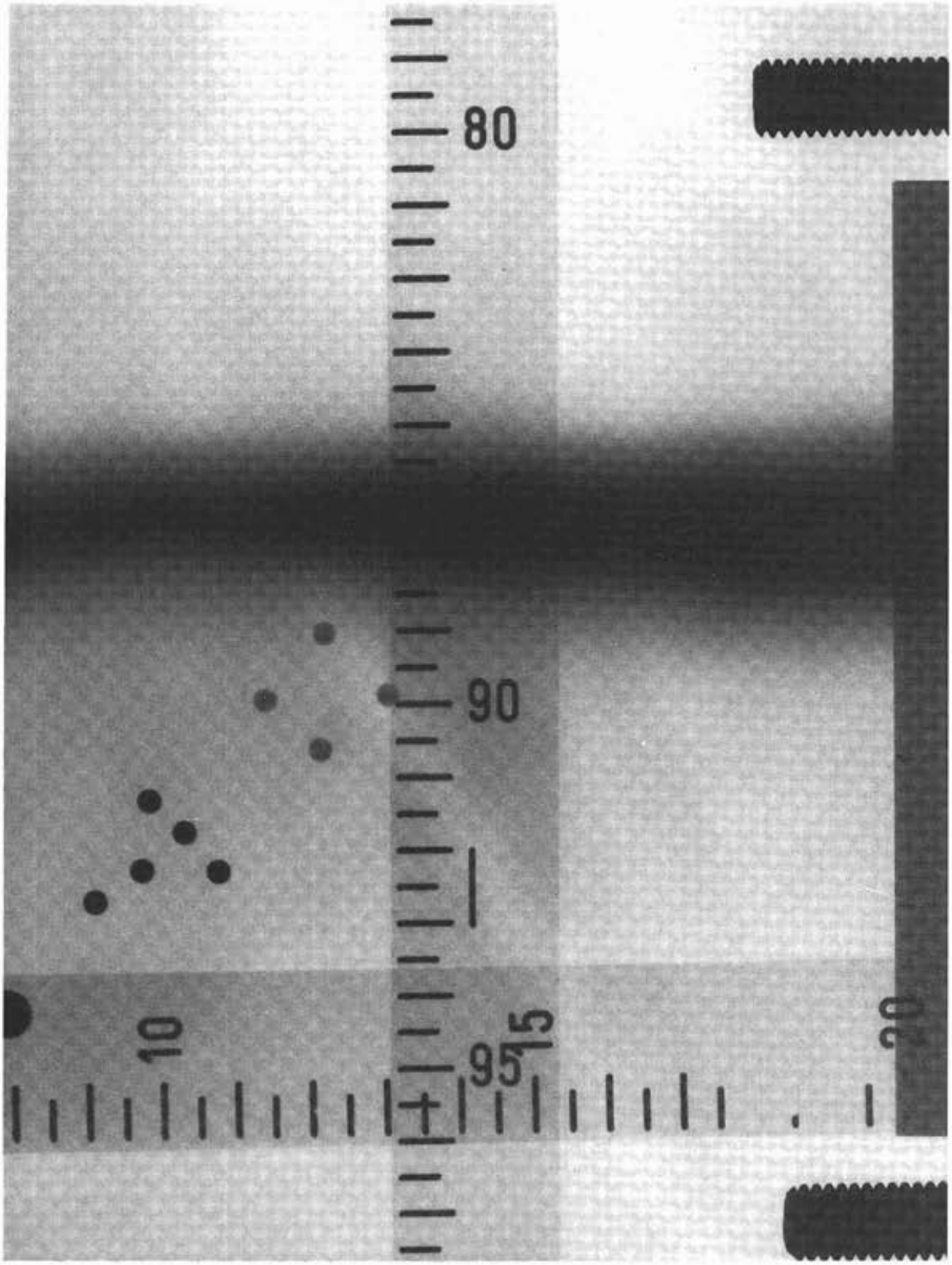

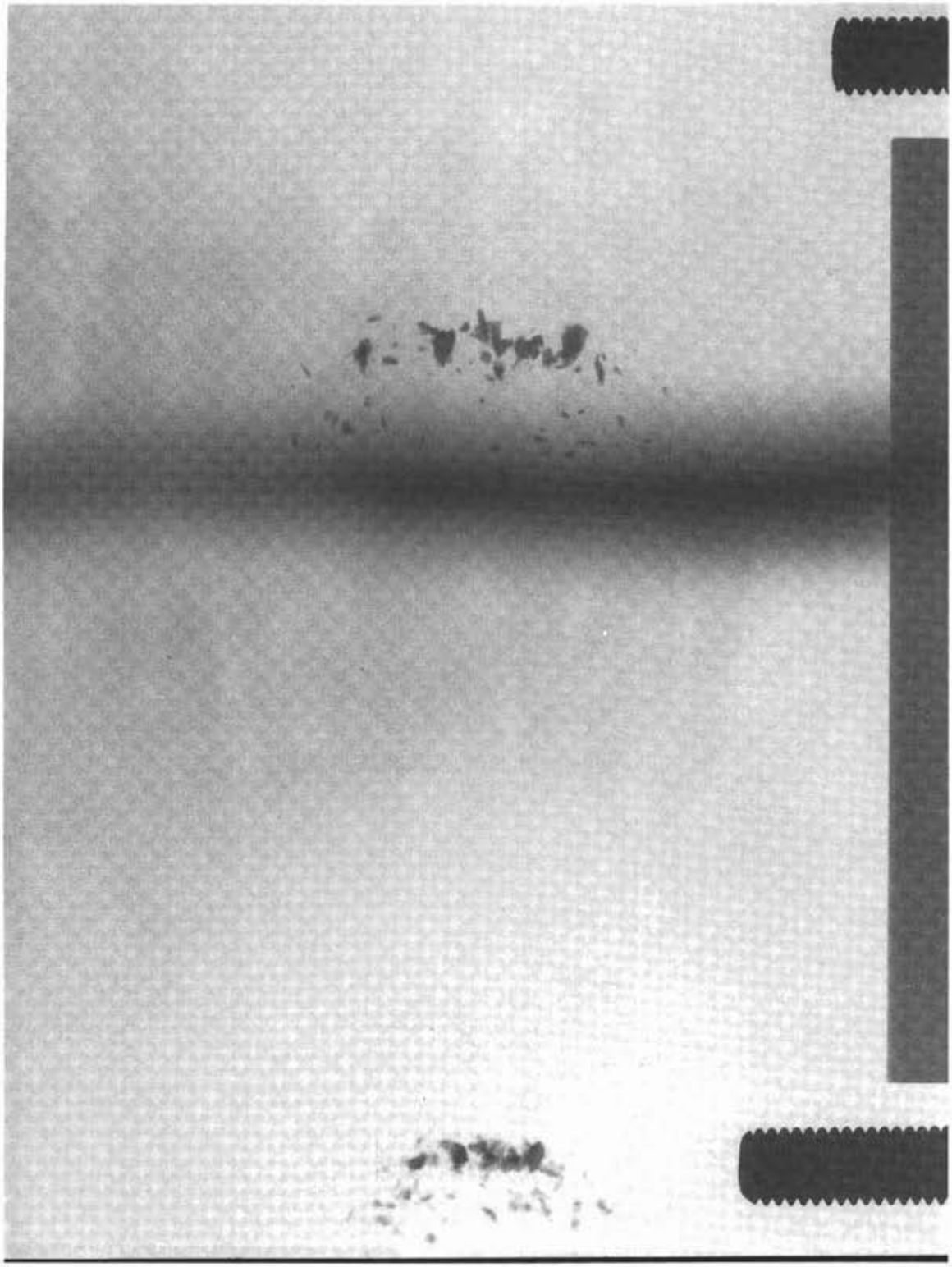

TEST AL-13

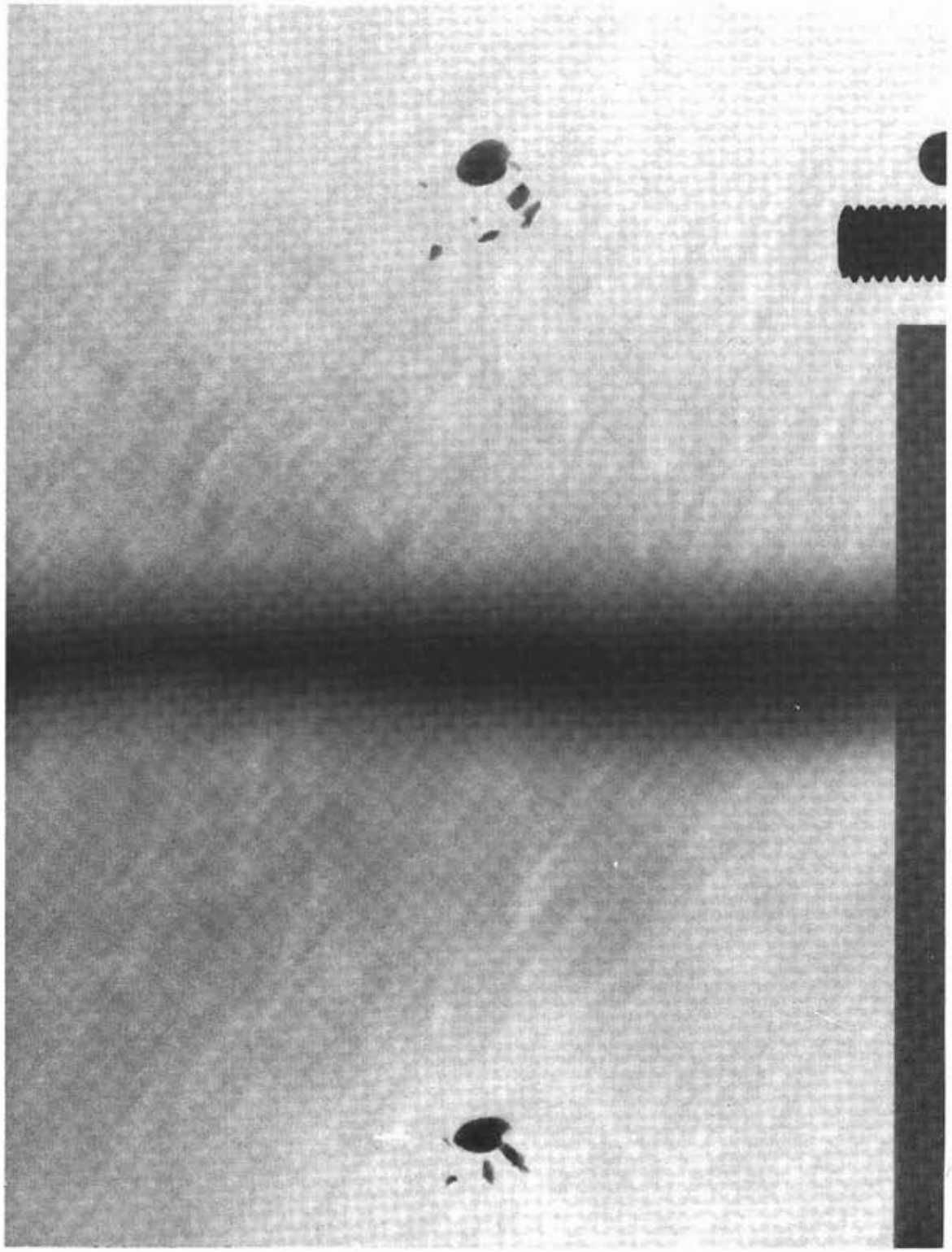

TEST AL-14

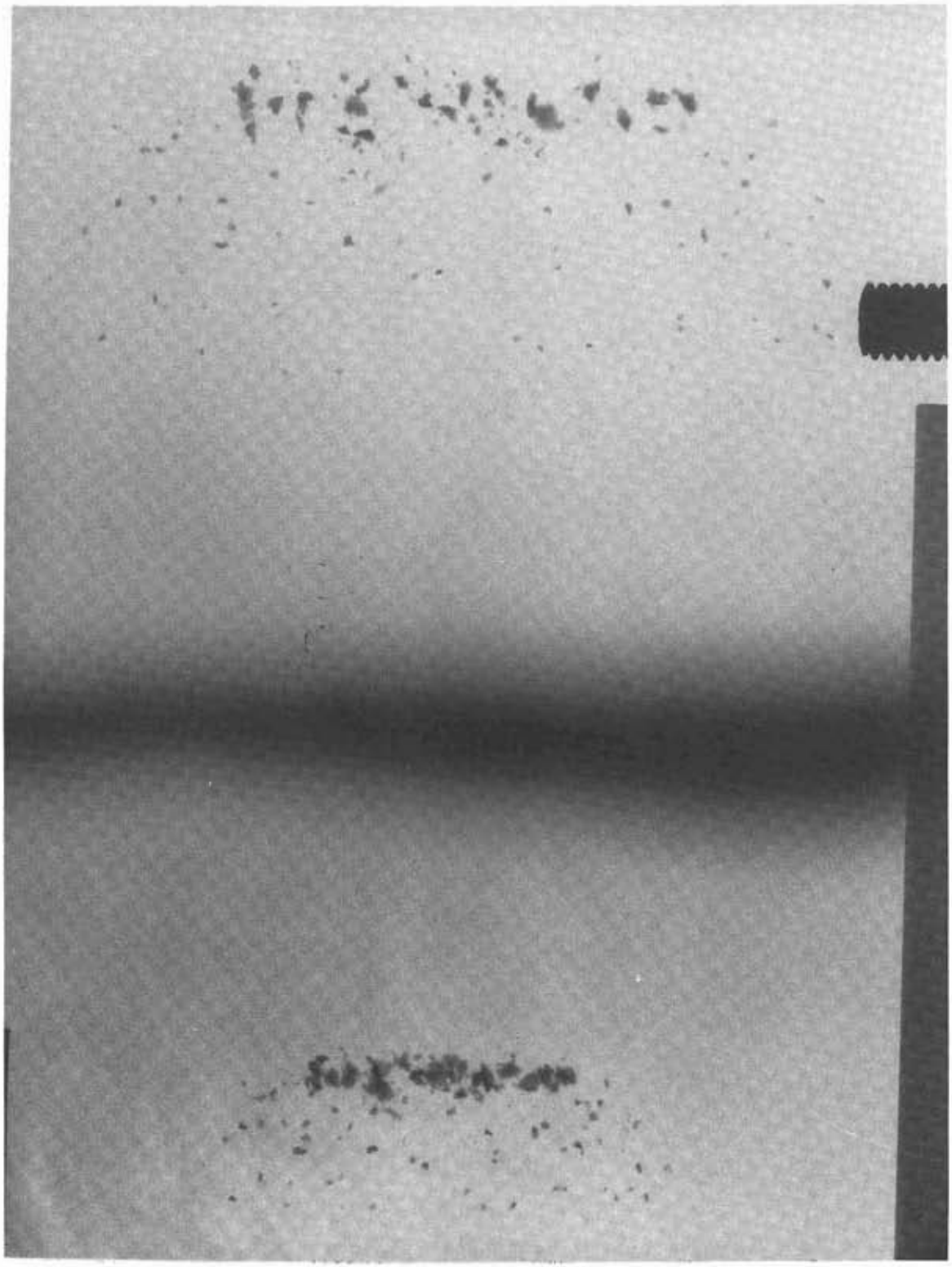

TEST AL-15

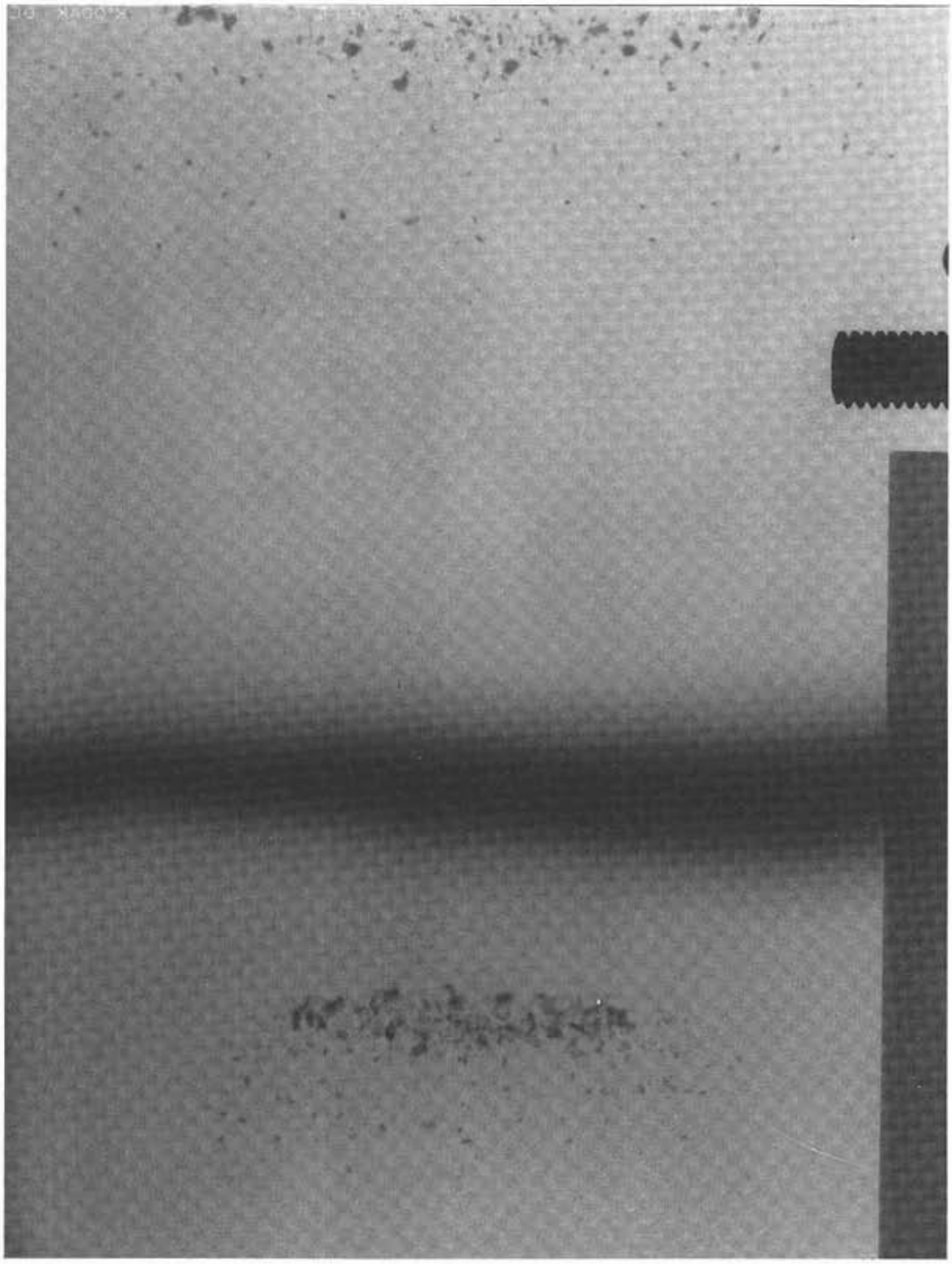

TEST AL-16

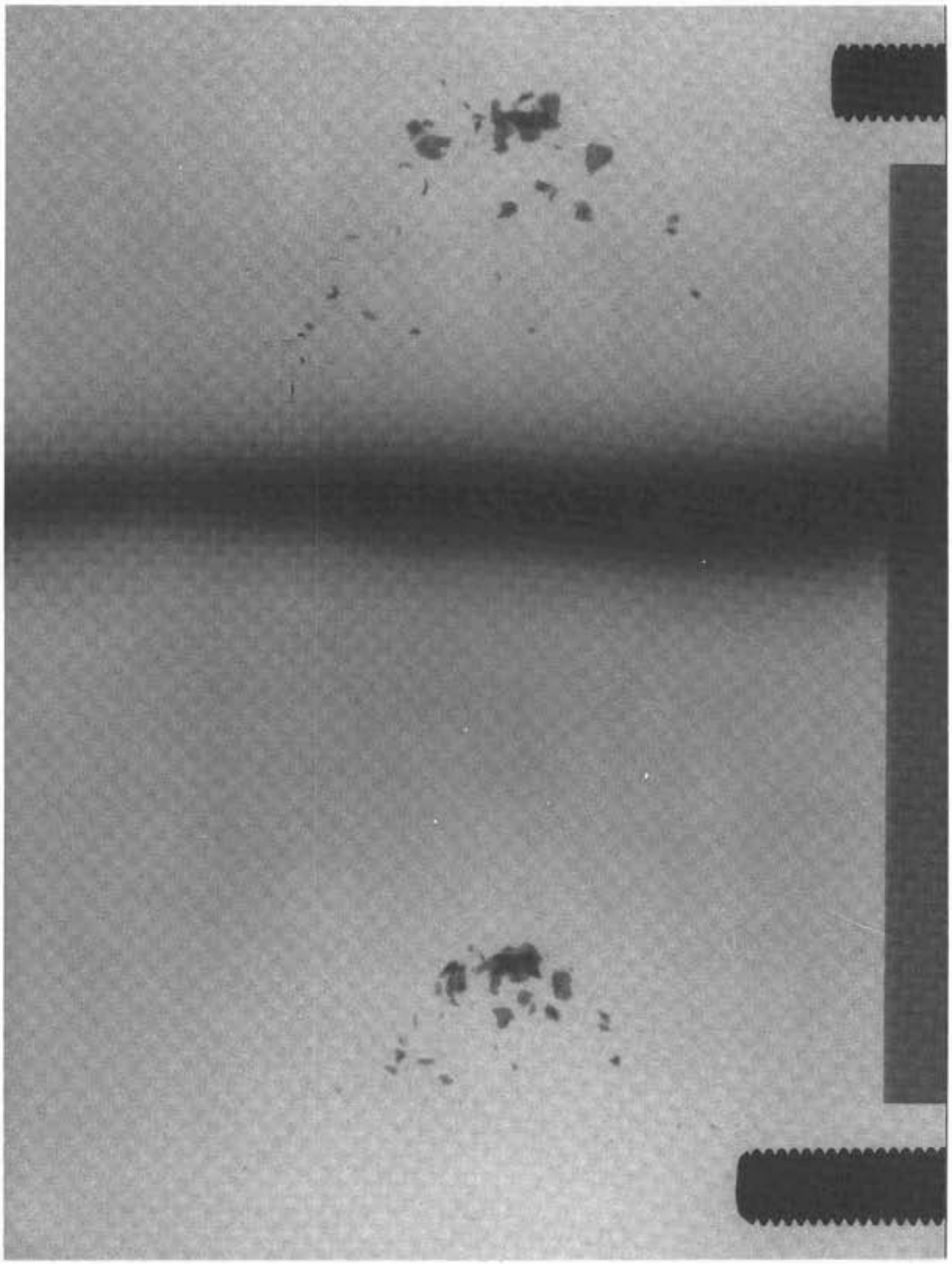

TEST AL-17

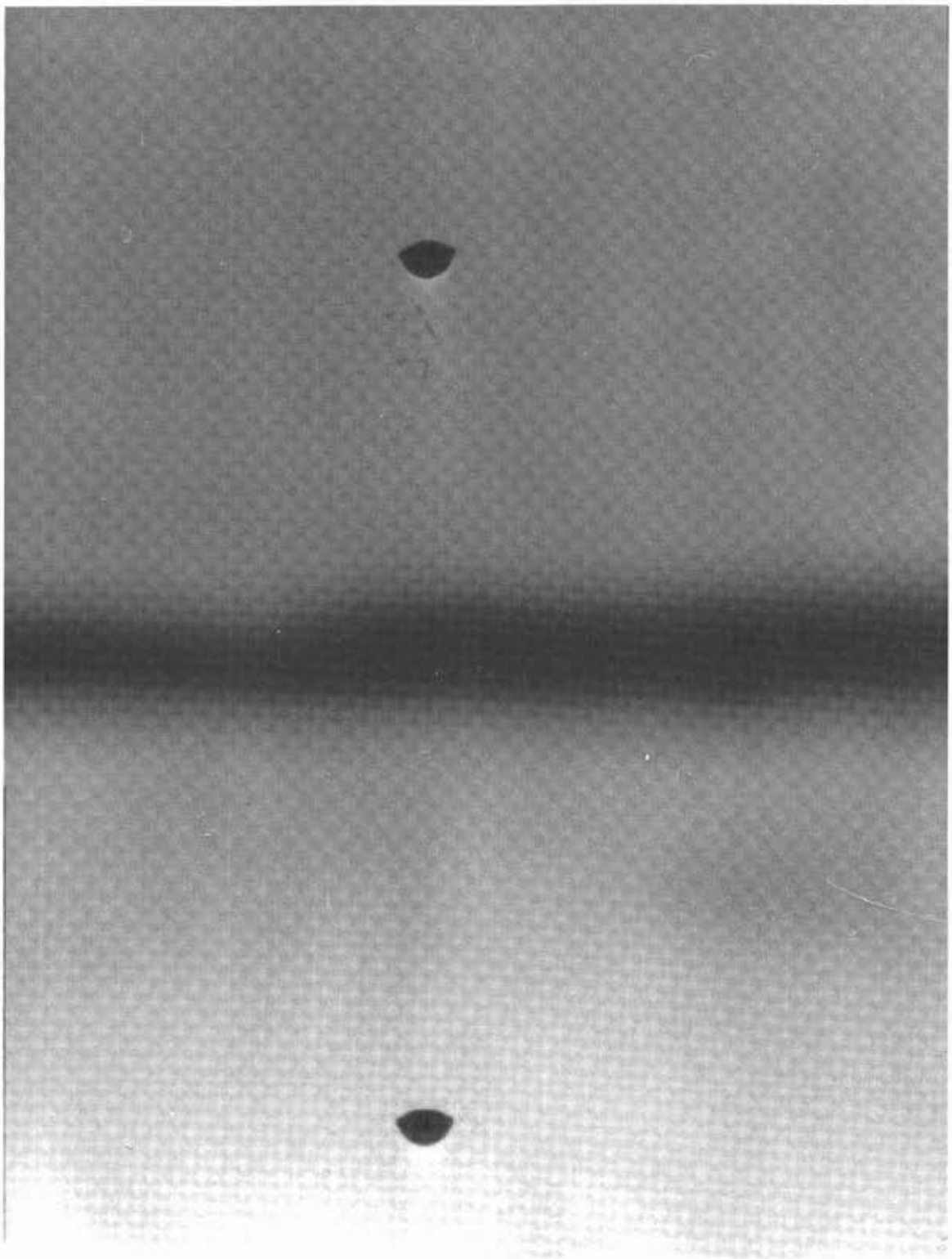

TEST AL-18

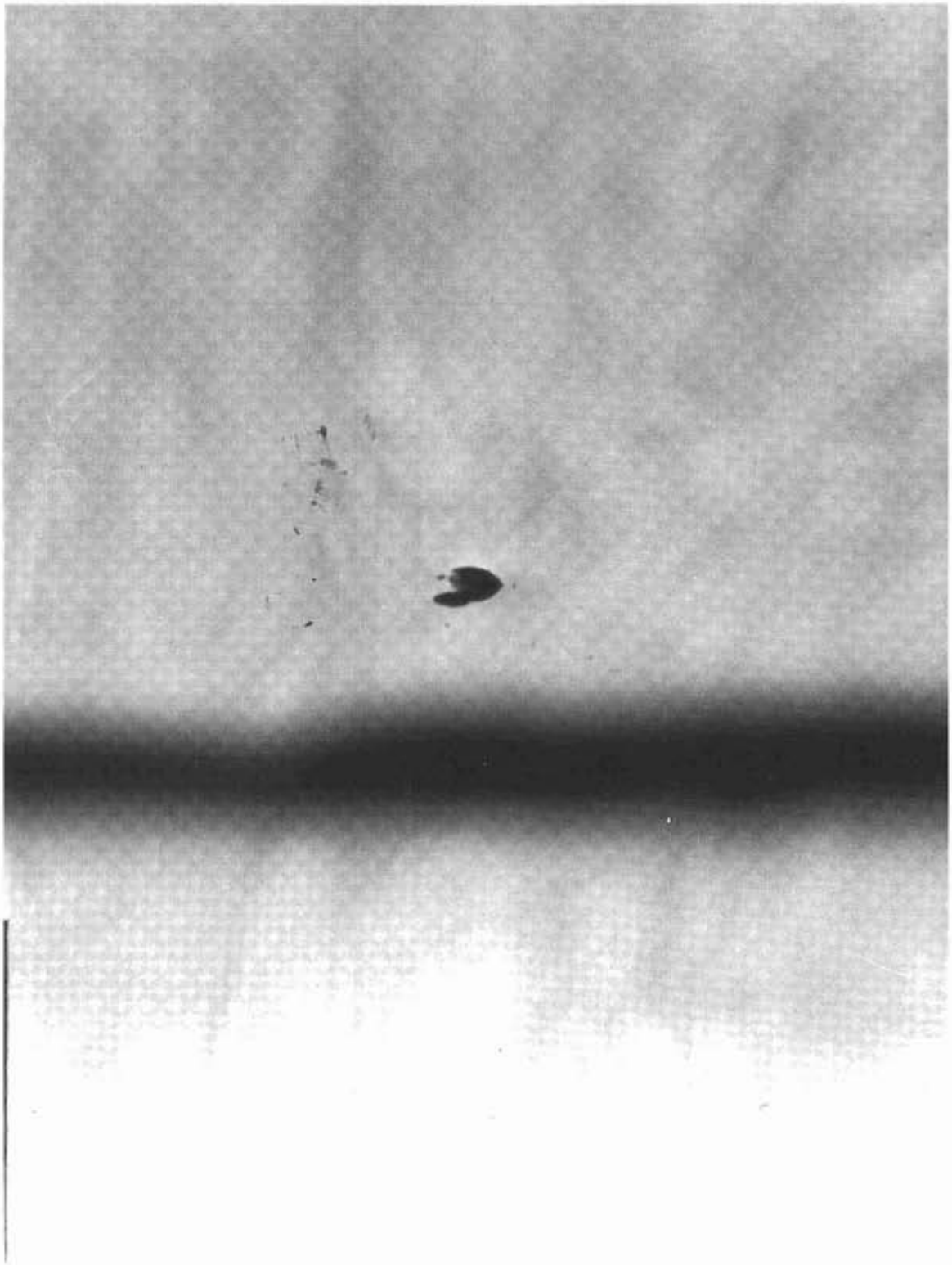

AL - Calibration

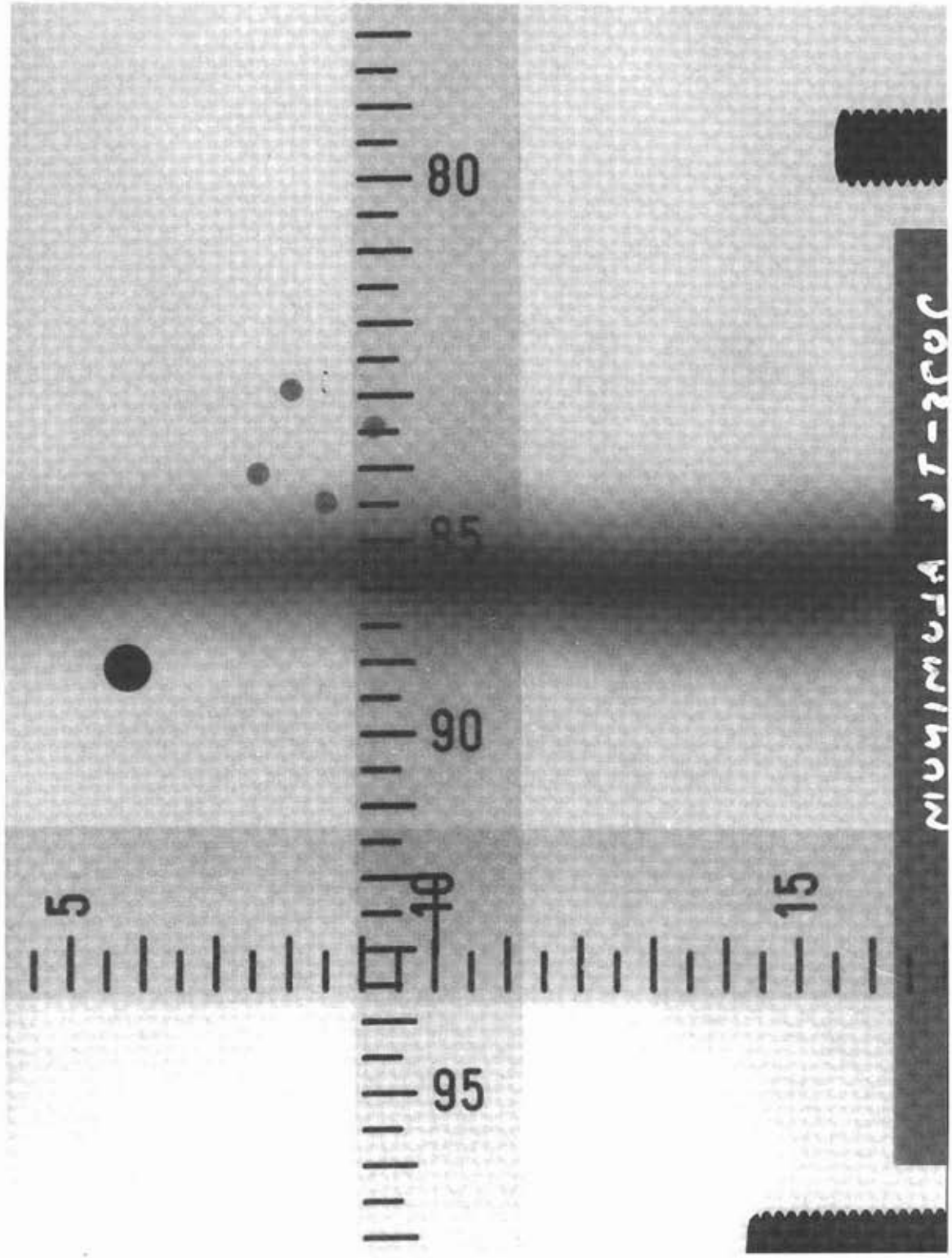

TEST AF-1

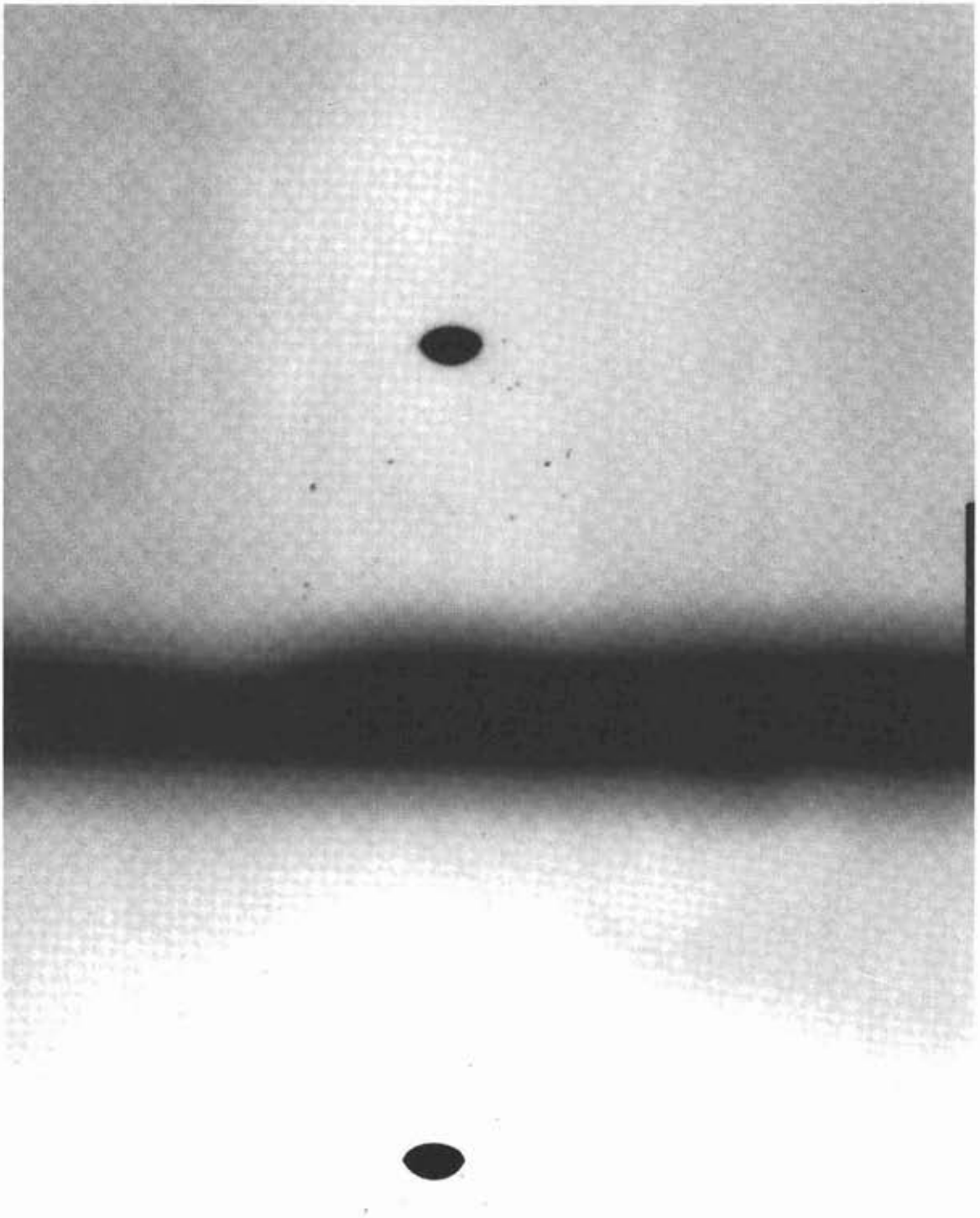

TEST AF-2

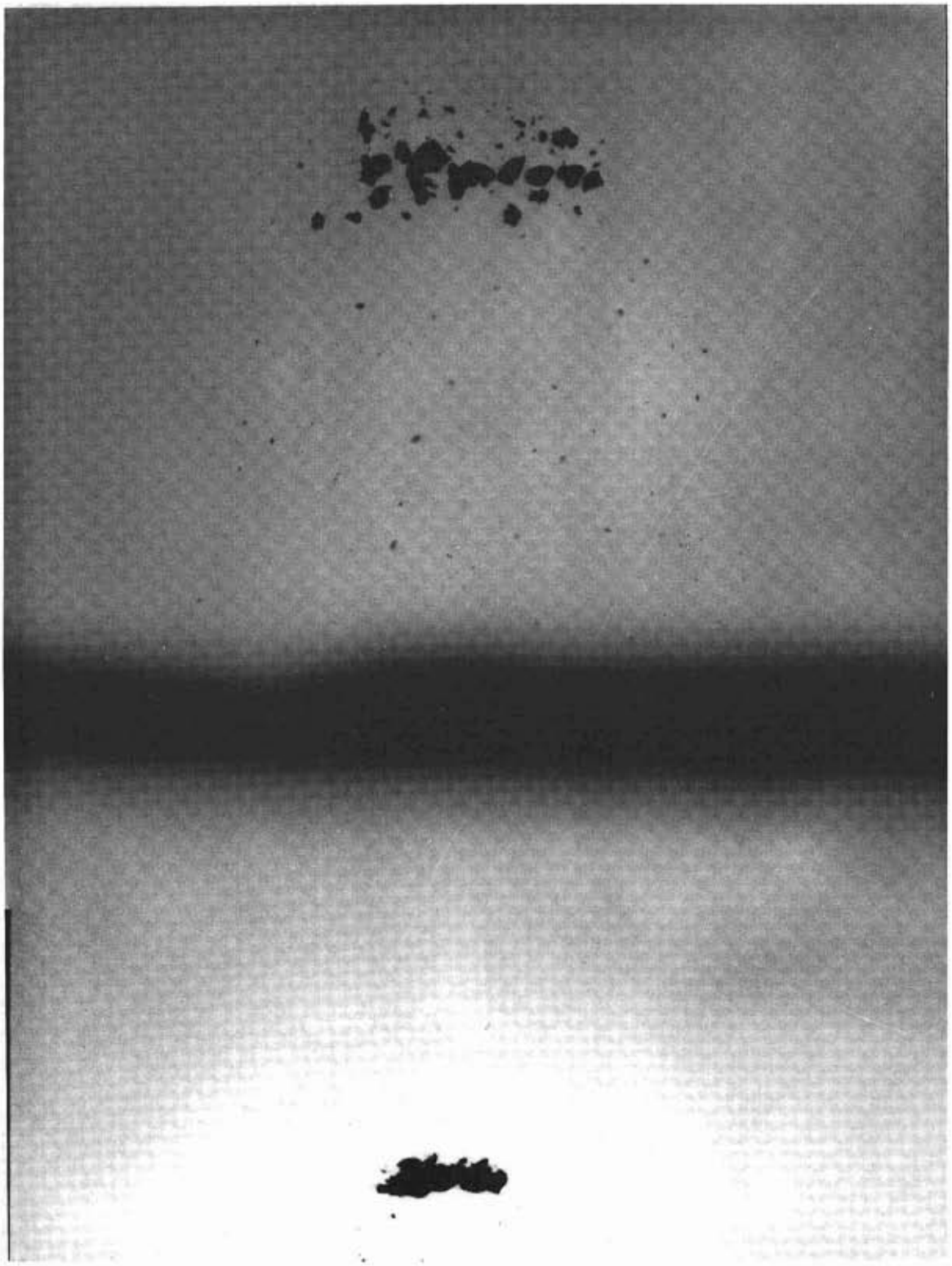

TEST AF-3

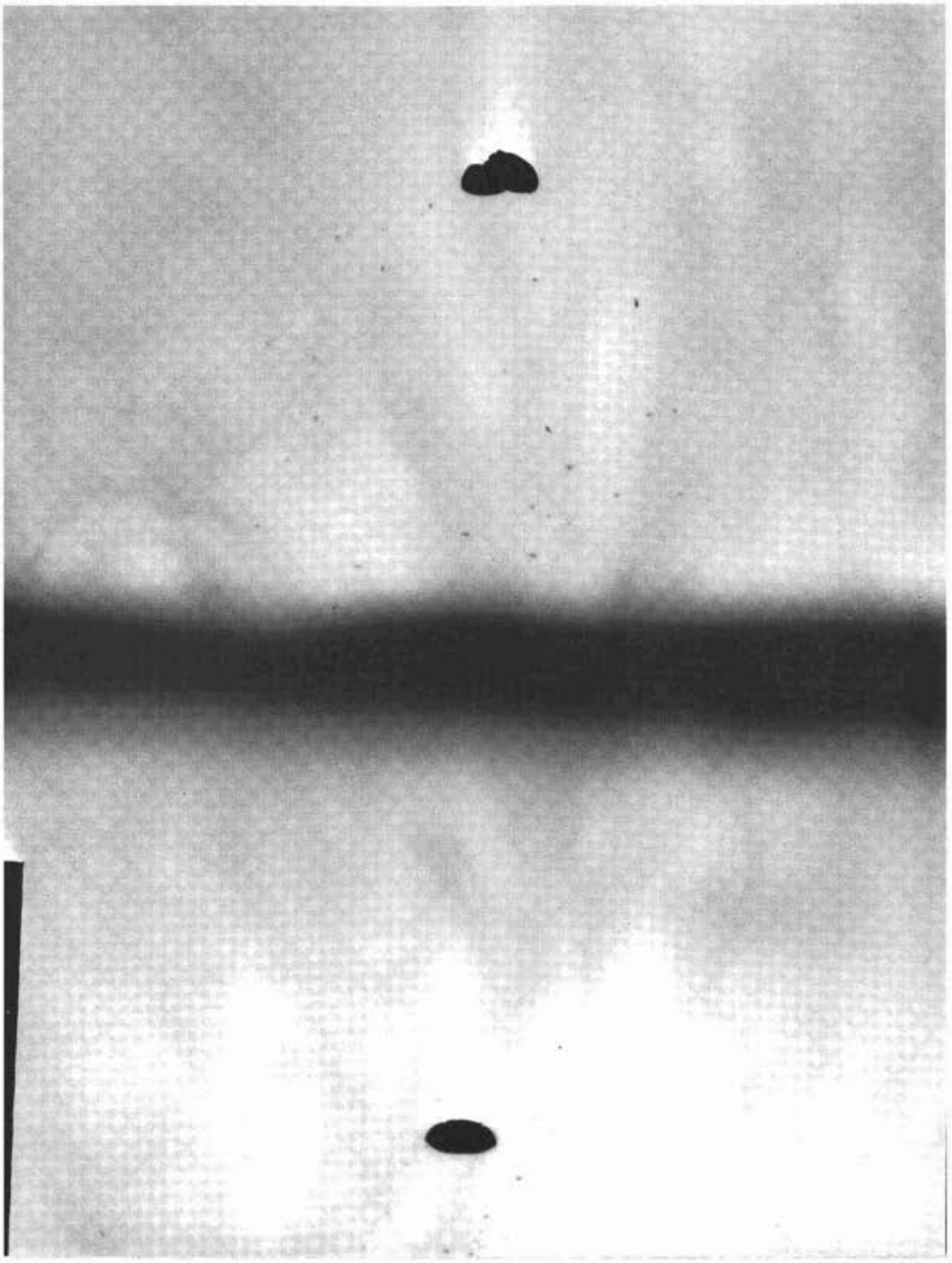

TEST AF-4

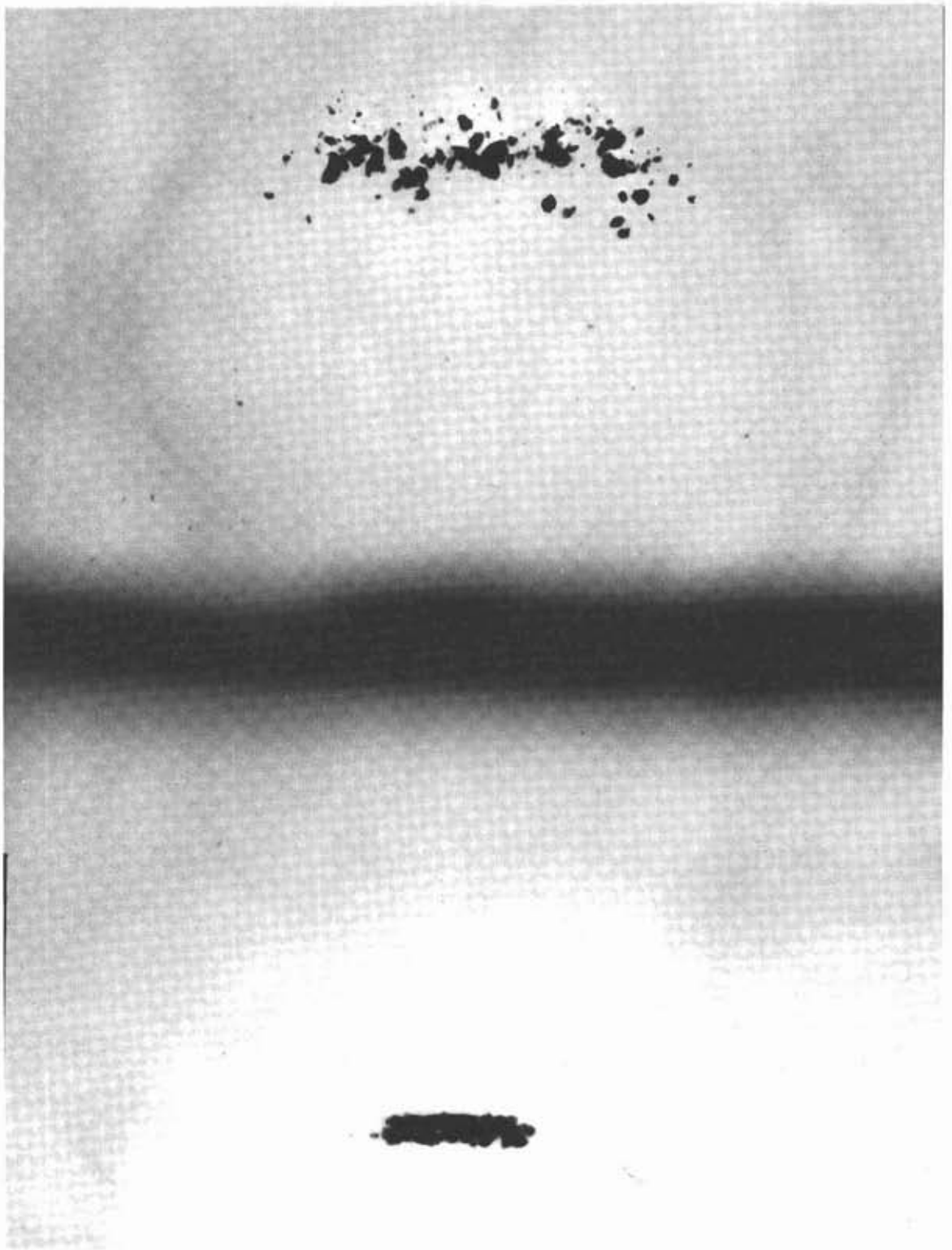

TEST AF-5

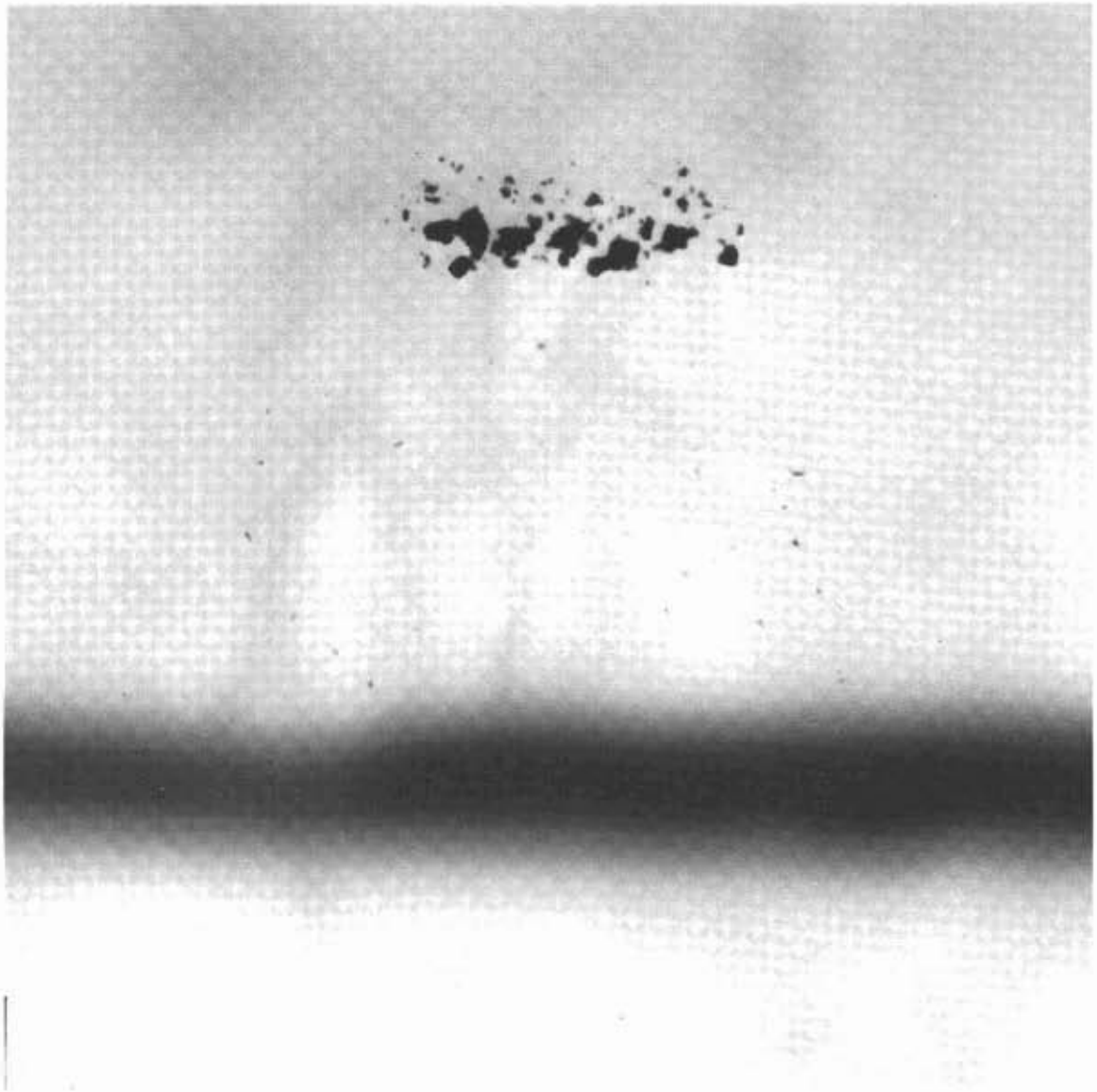

TEST AF-6

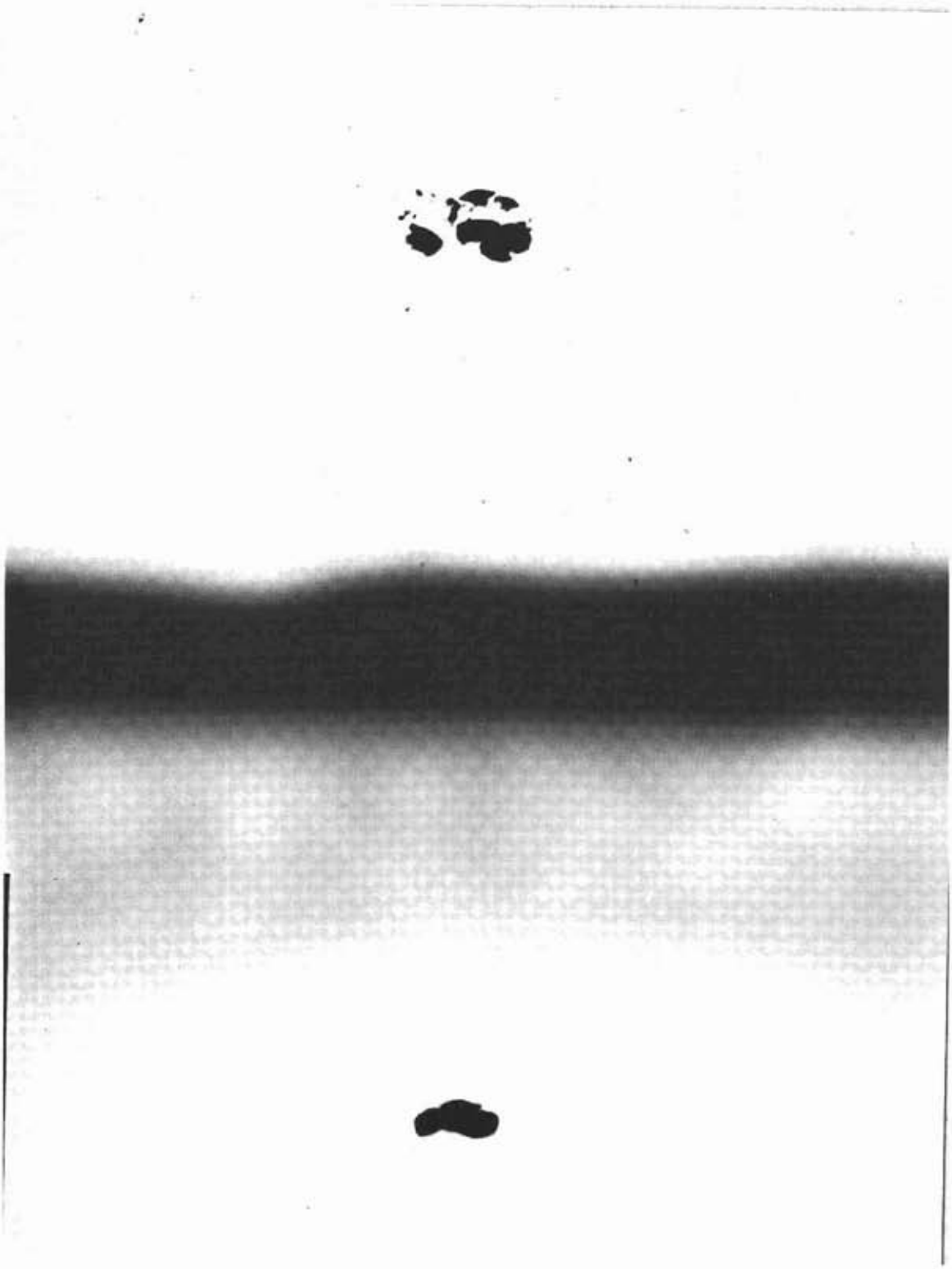

TEST AF-7

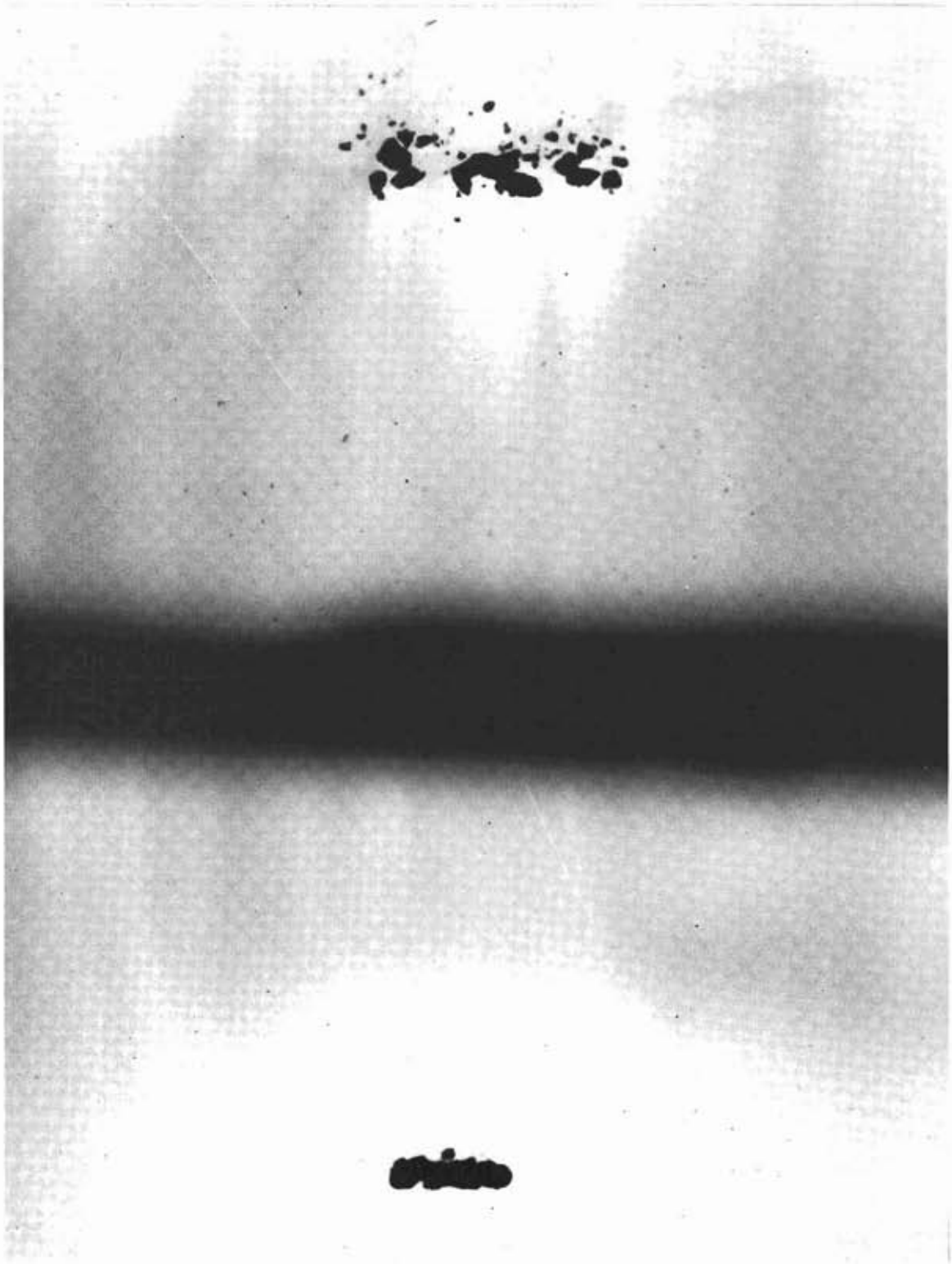

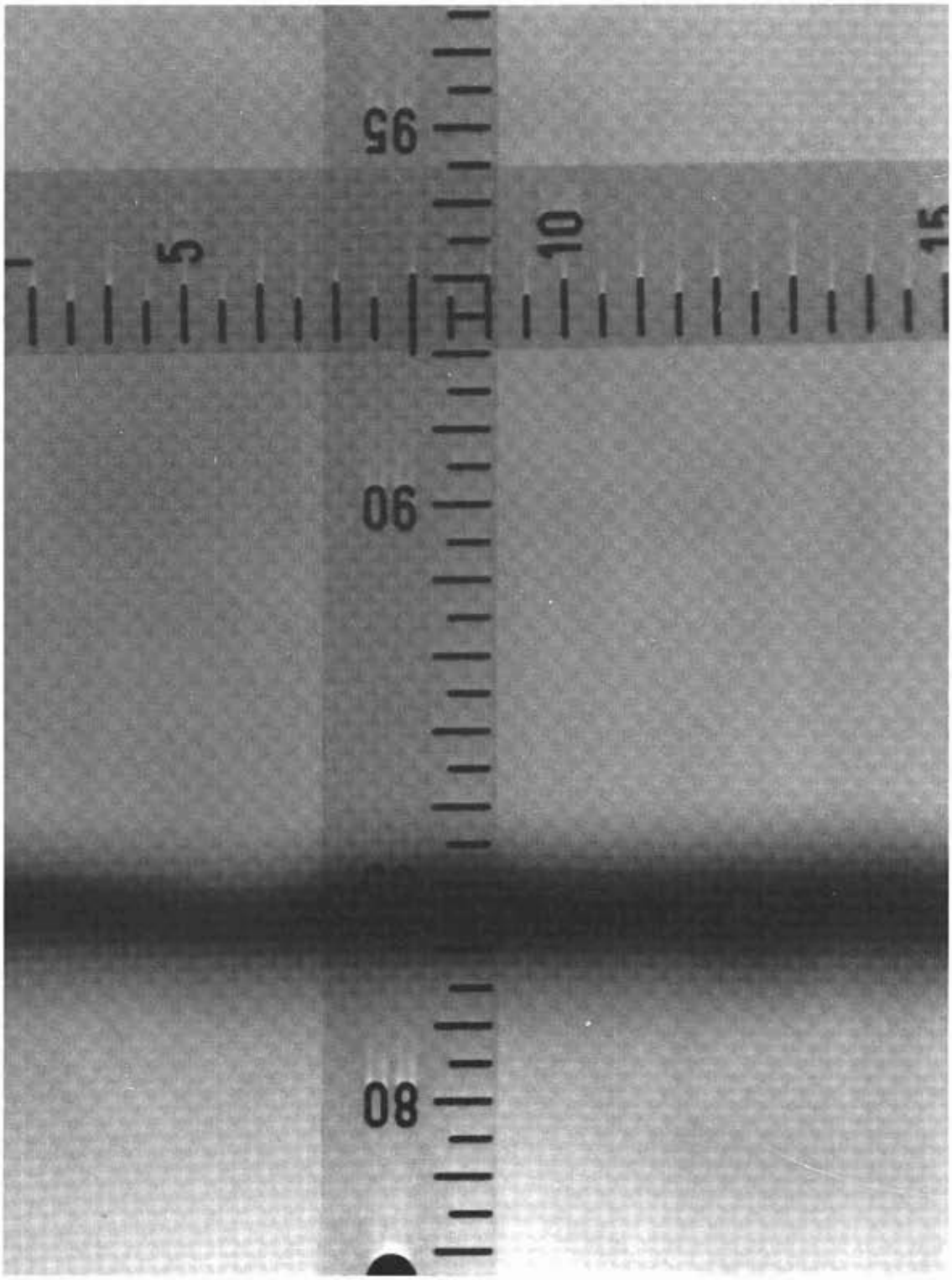
5
10
15
80
90
95

TEST D-1

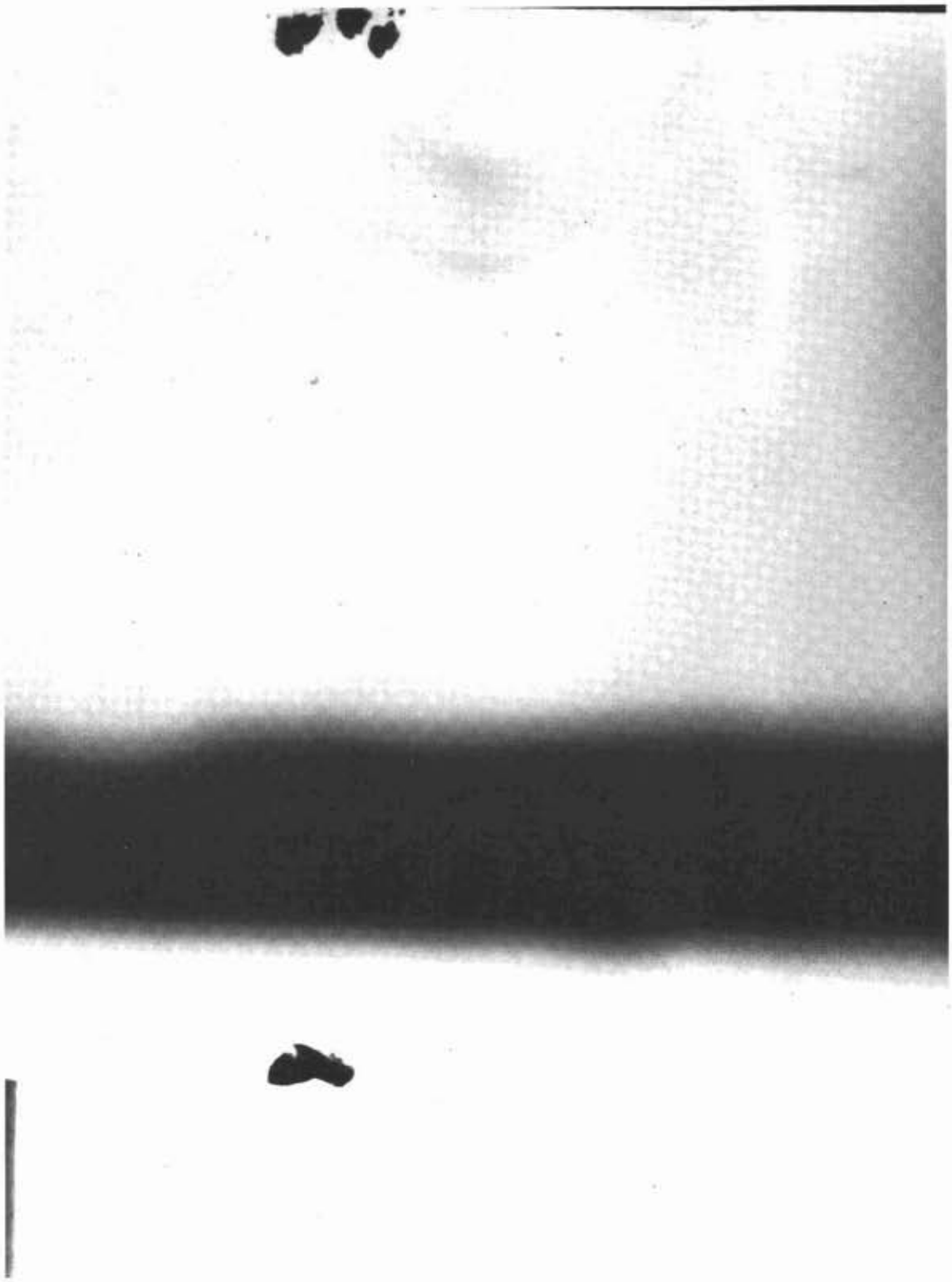

TEST D-3

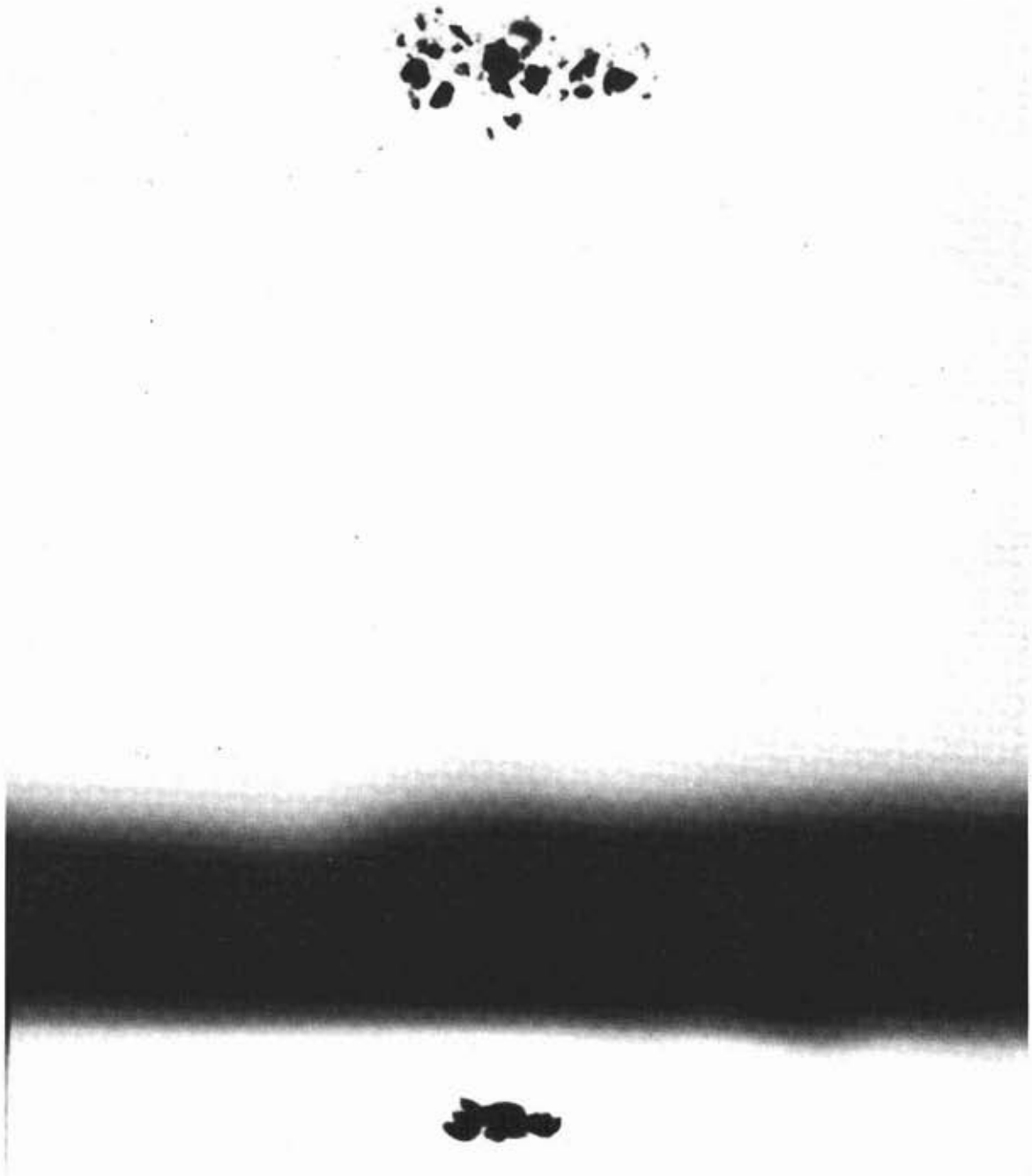

TEST D-4

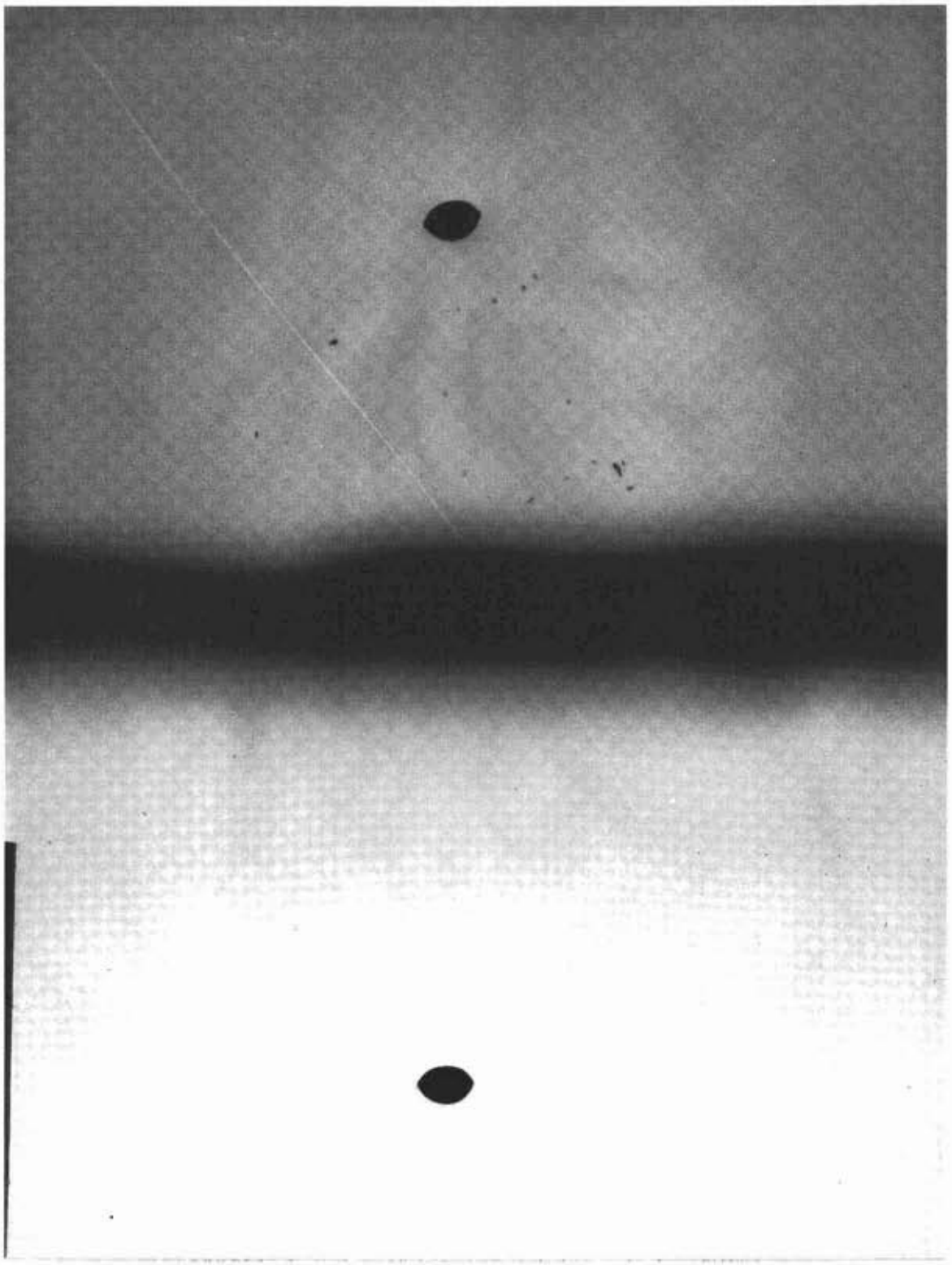

TEST D-5

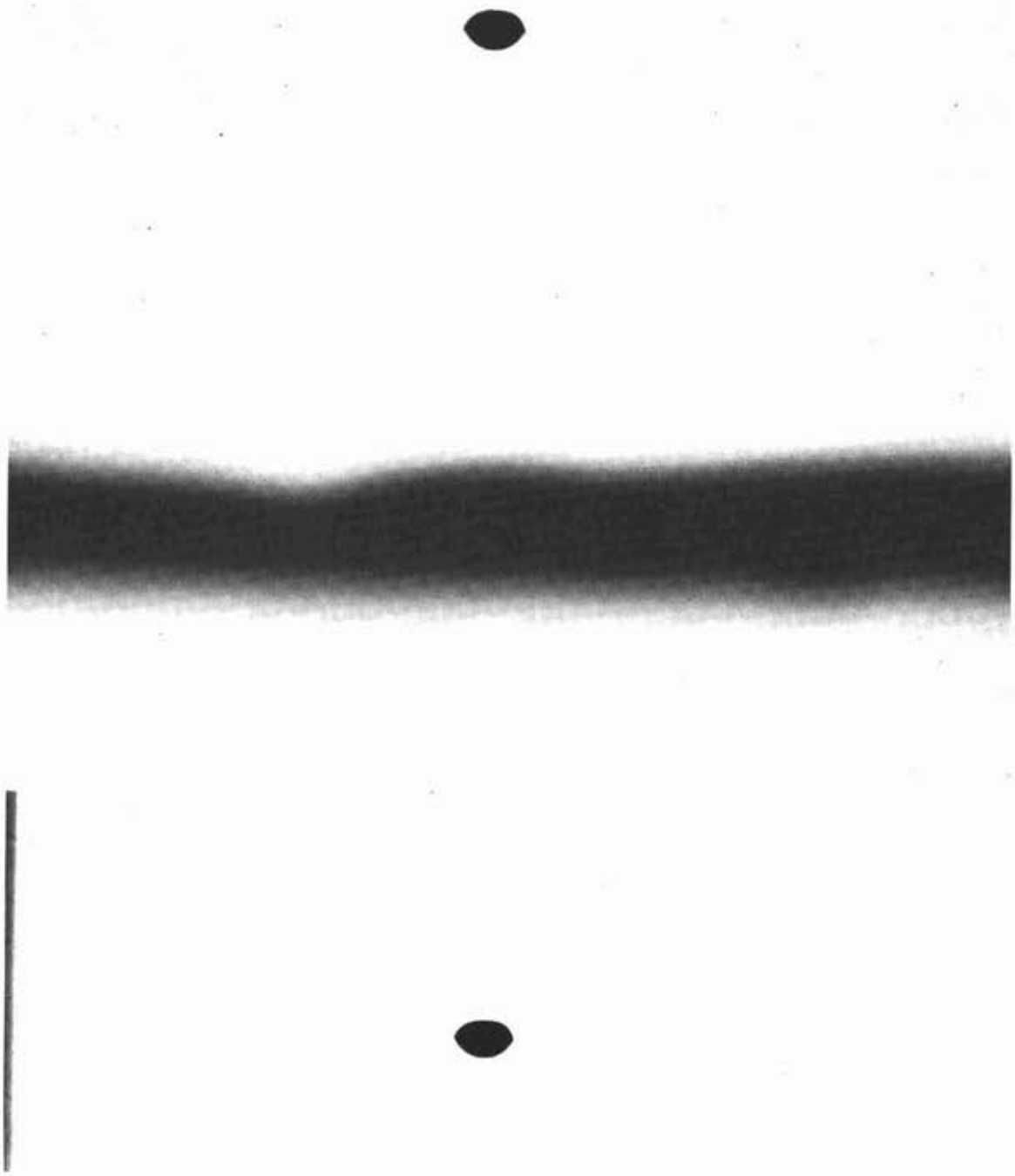

TEST D-6

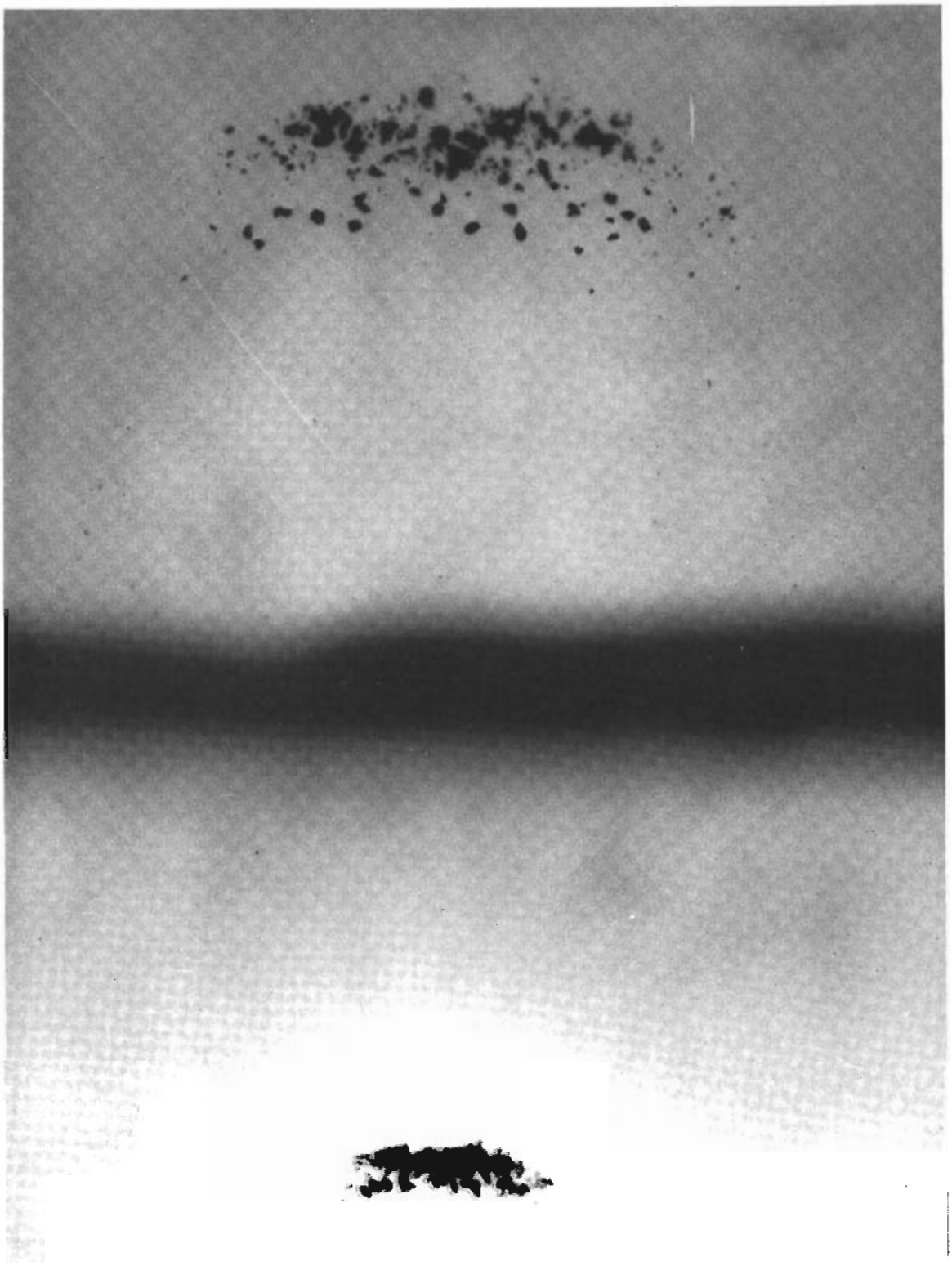

TEST D-7

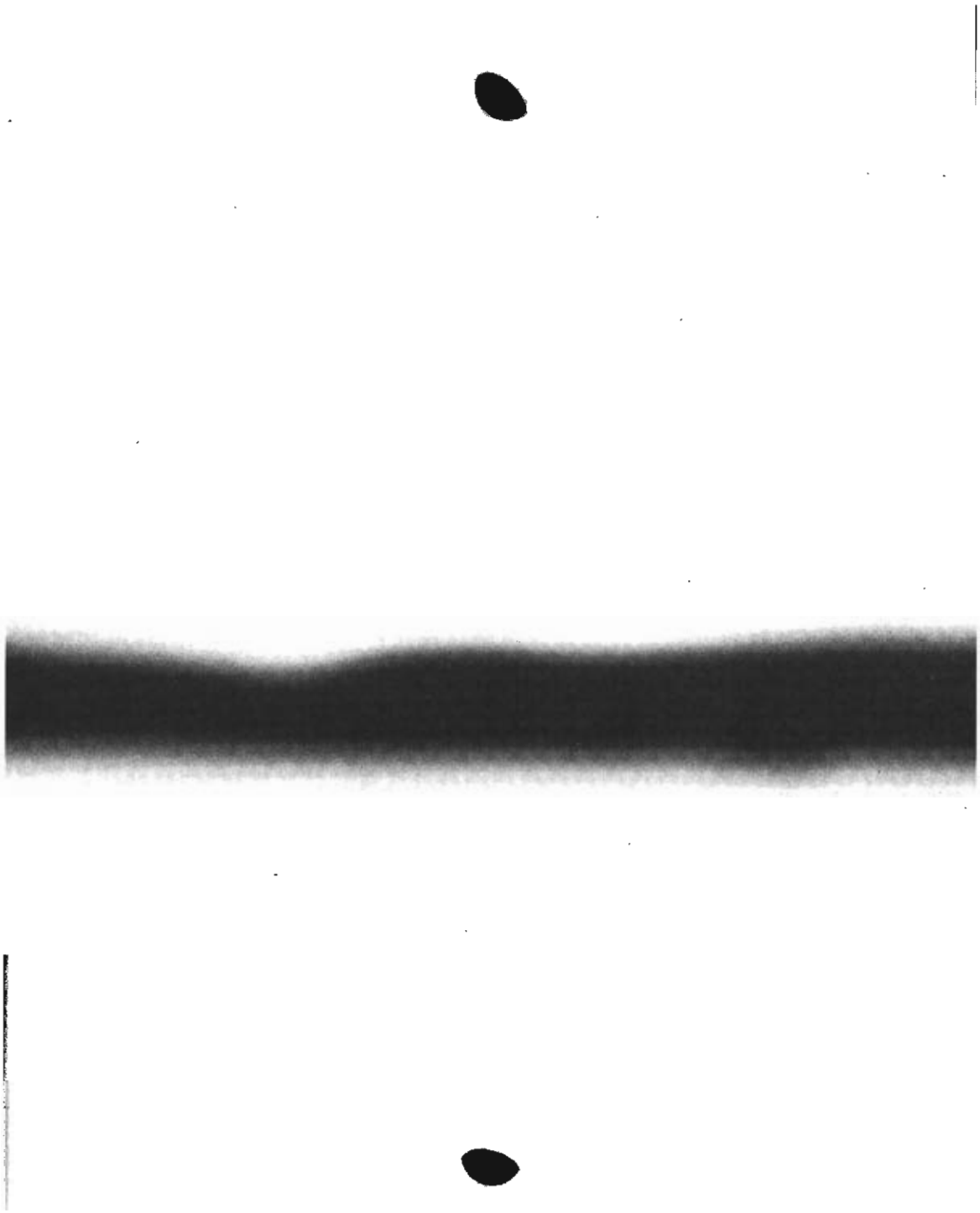

TEST D-8

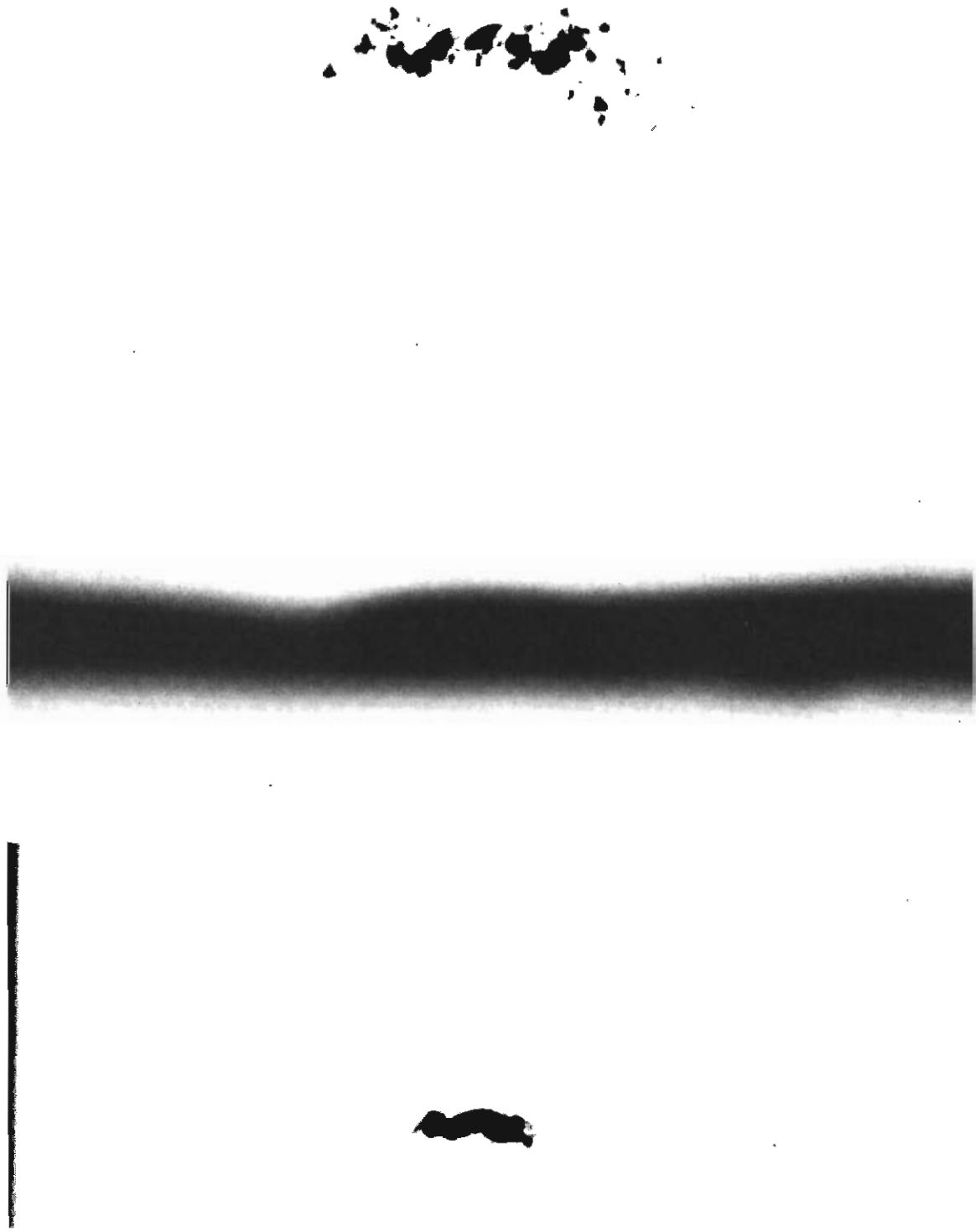

TEST D-9

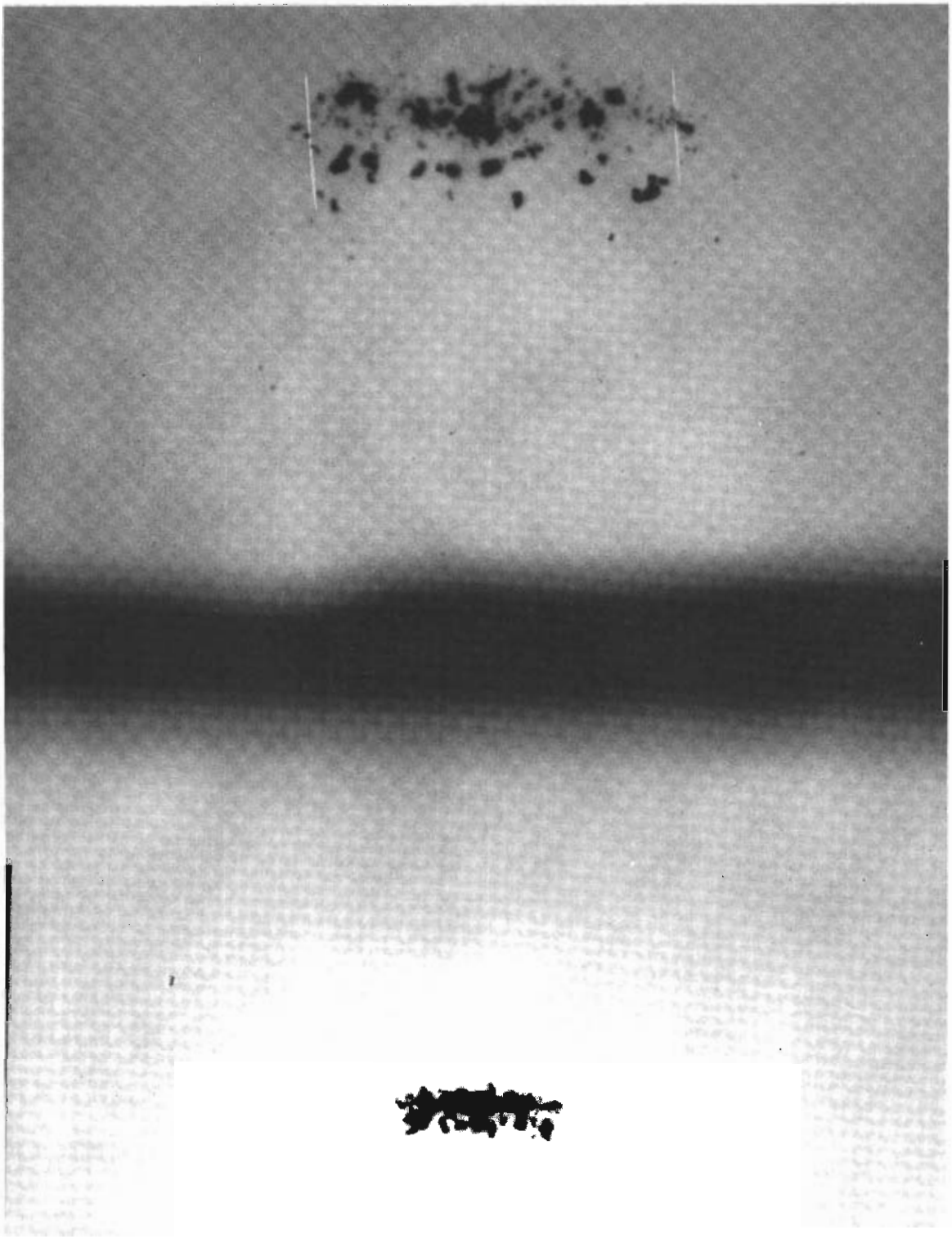

D - Calibration

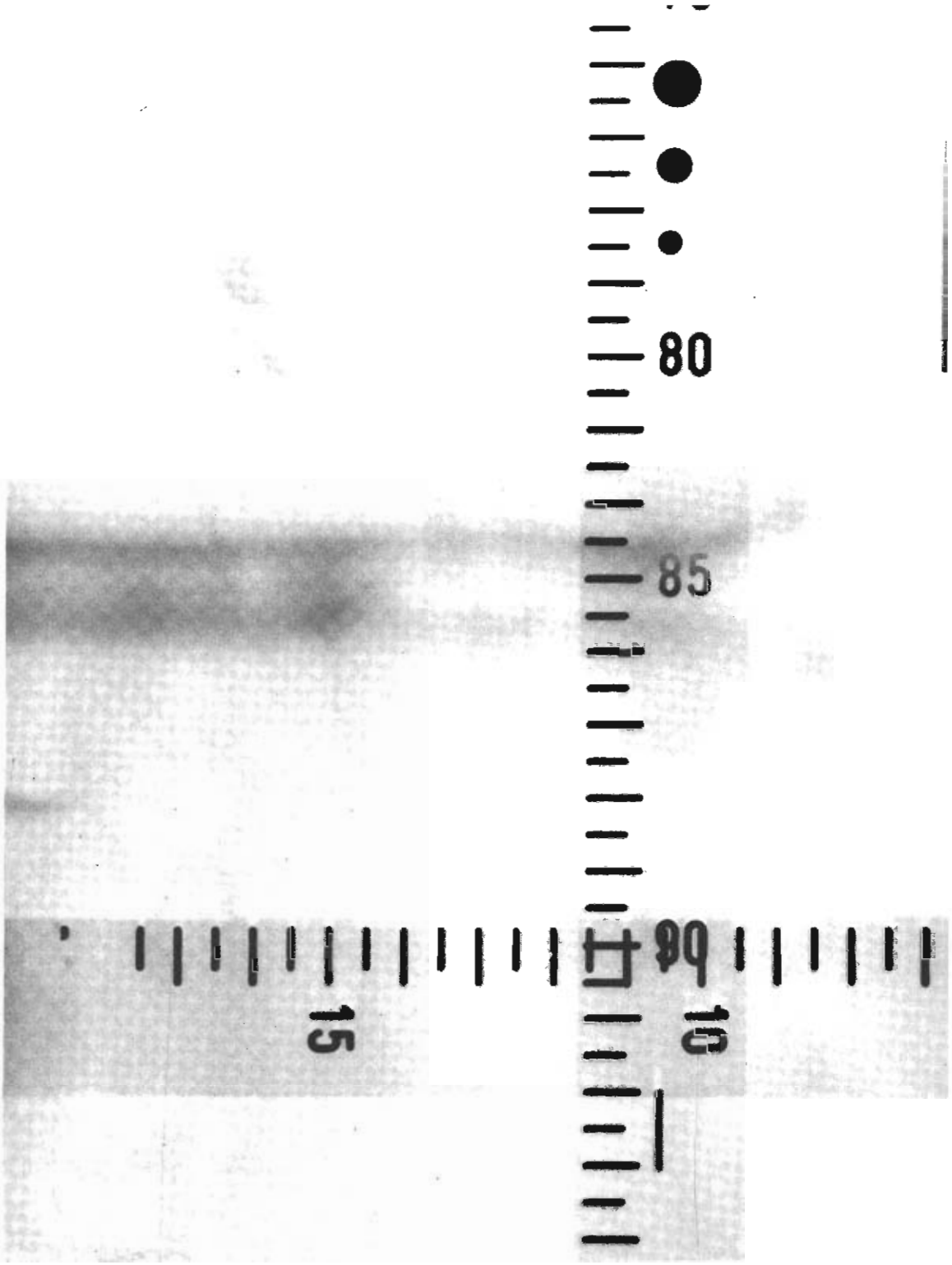

TEST AP-1

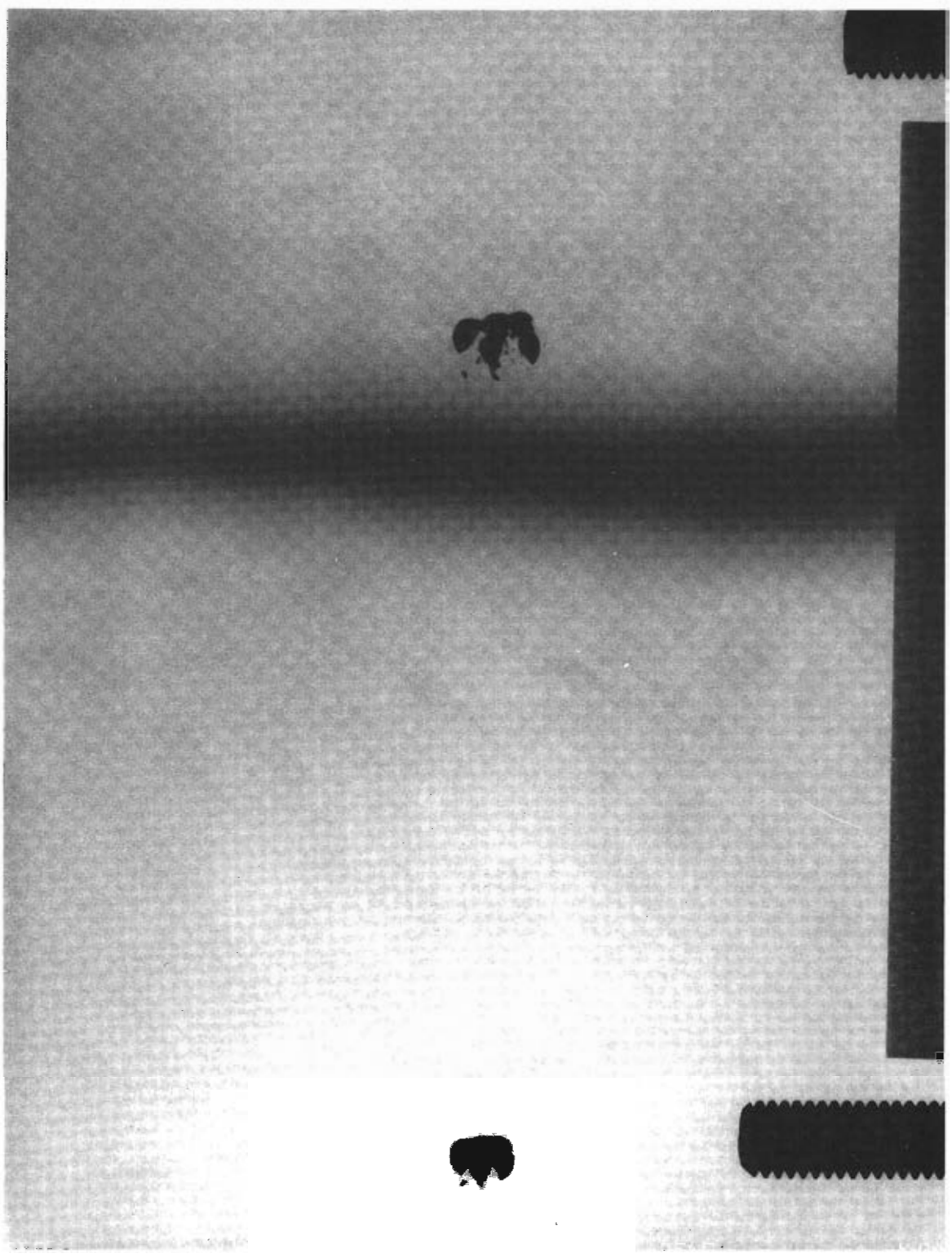

TEST AP-3

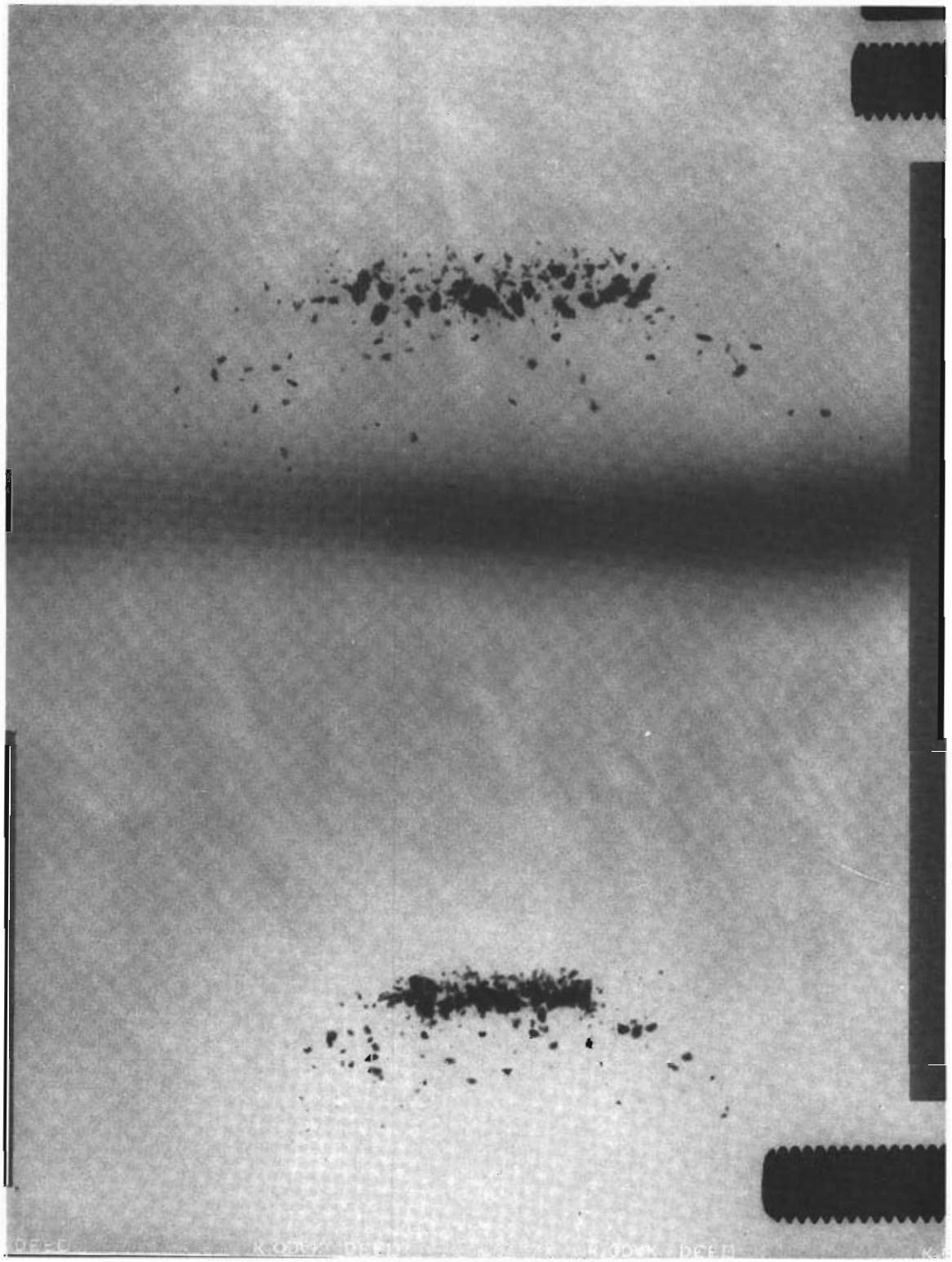

TEST AP-4

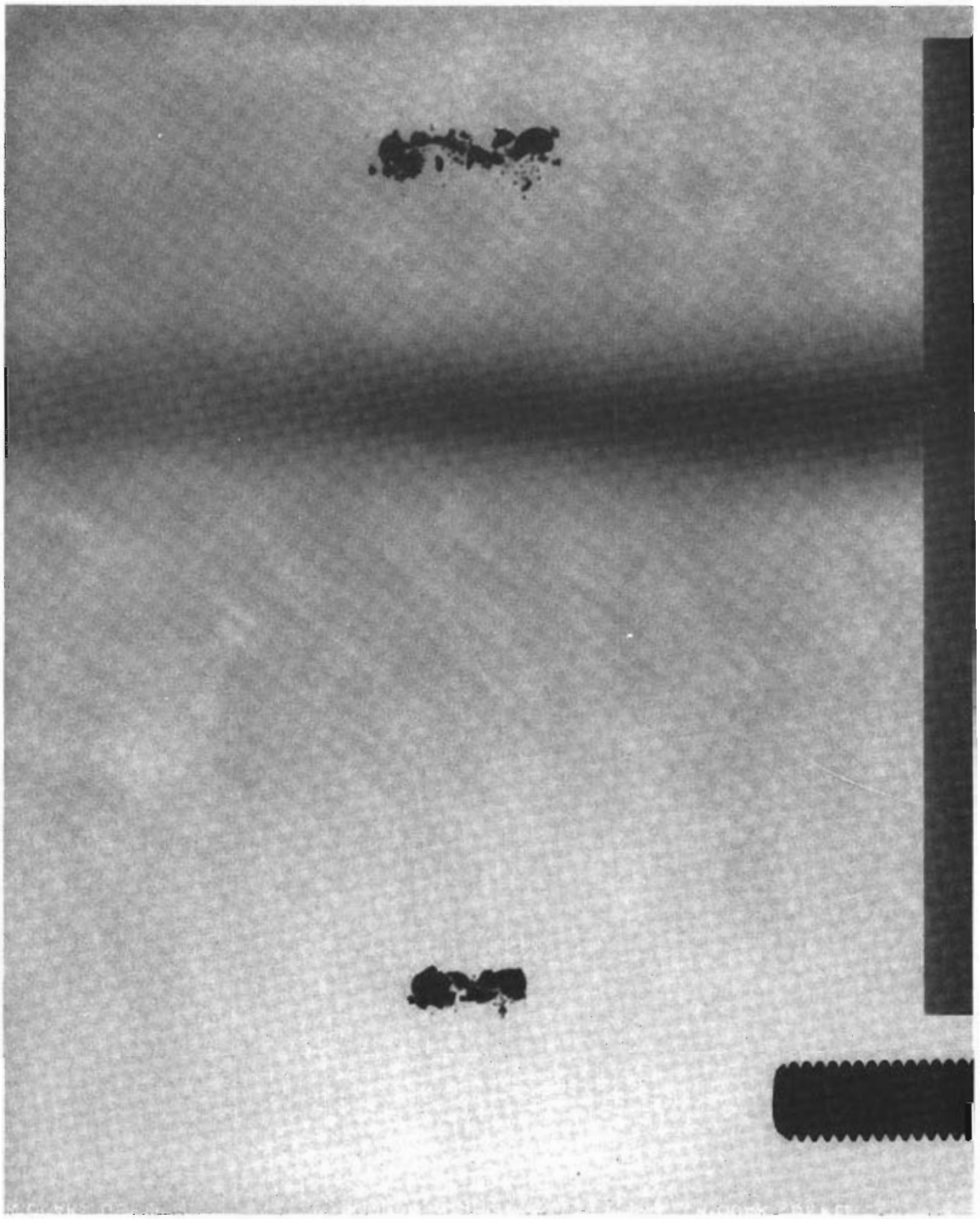

TEST AP-6

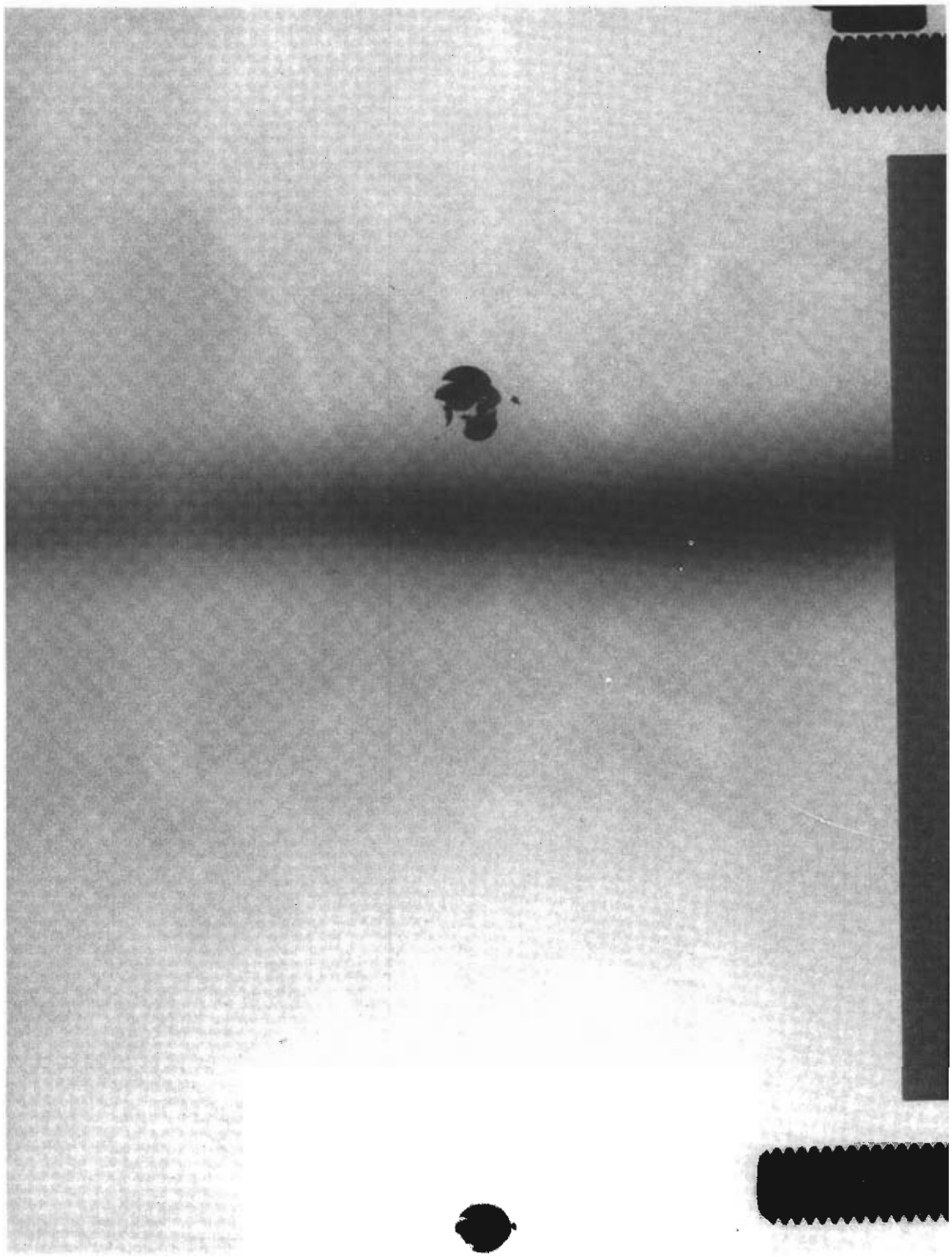

TEST AP-7

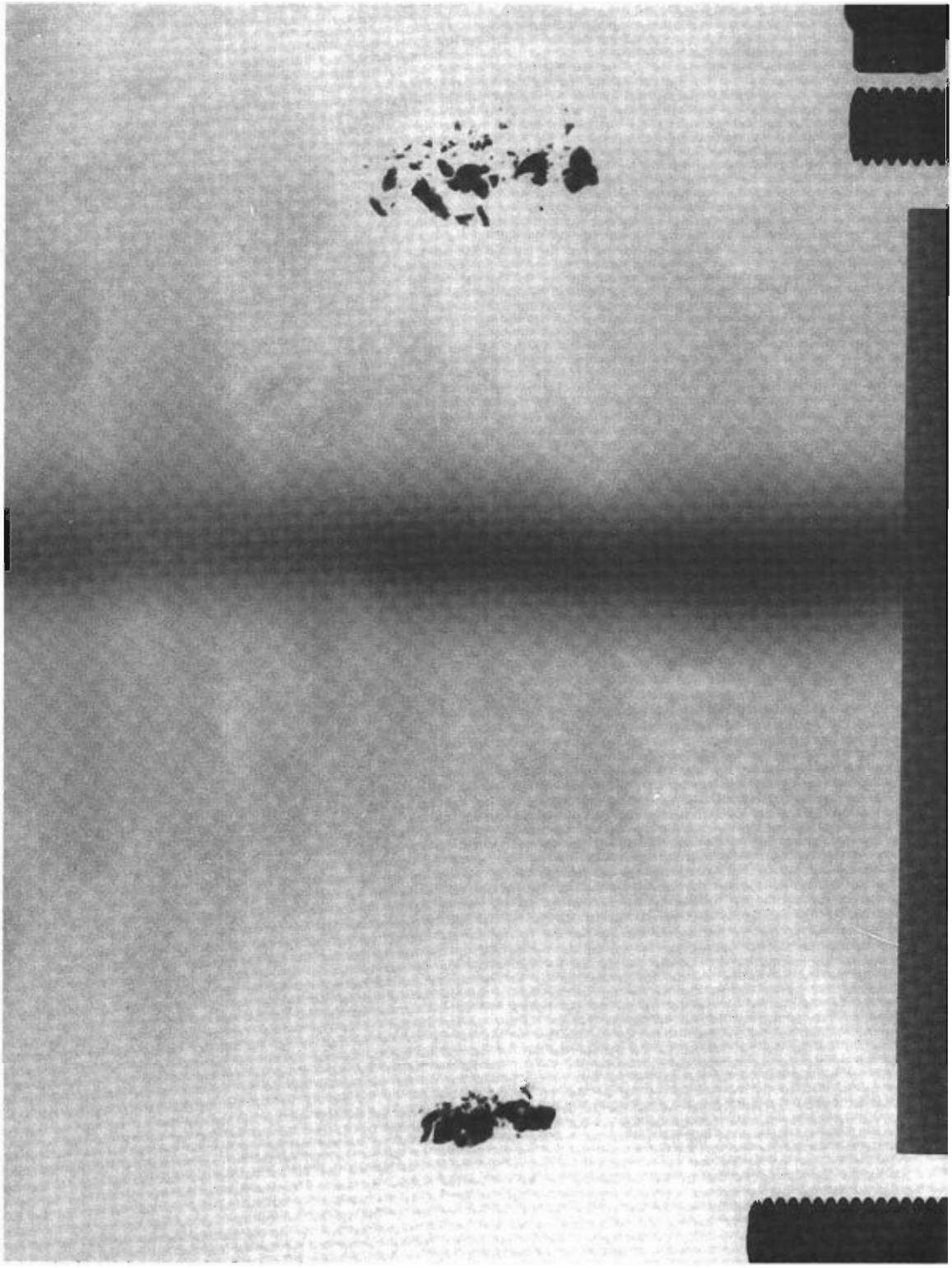

AP - Calibration

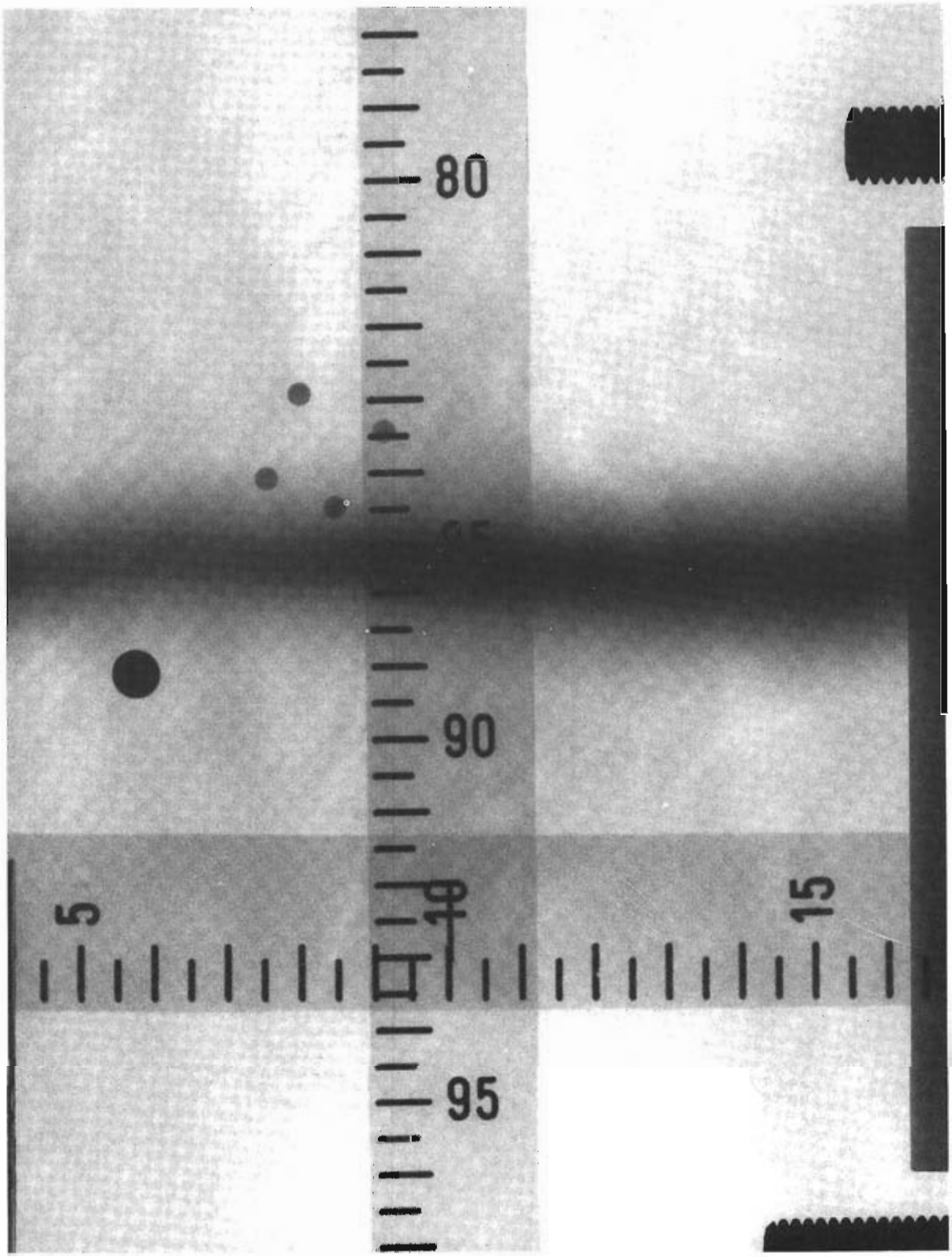

TEST SS-1

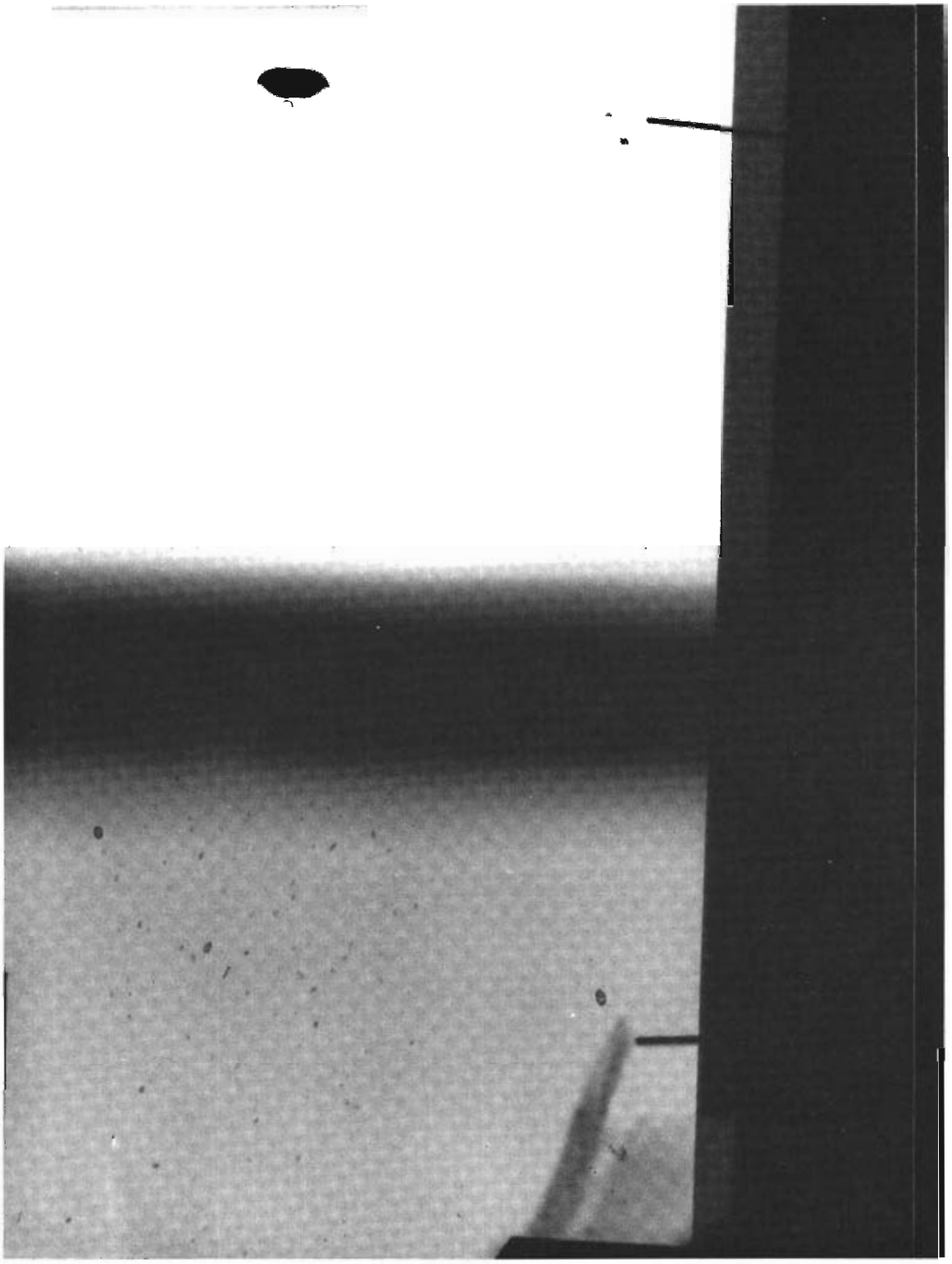

TEST SS-2

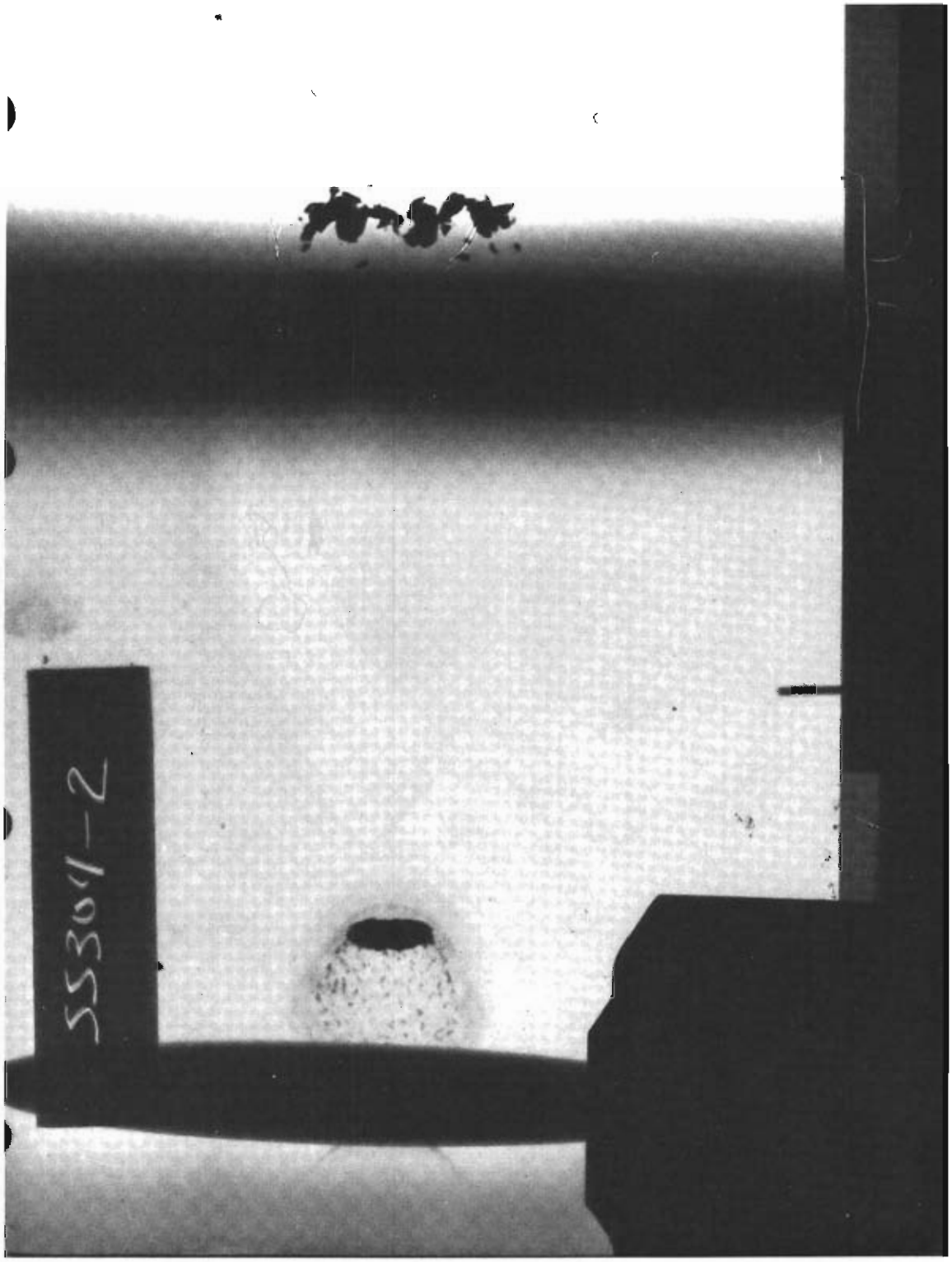

TEST SS-4

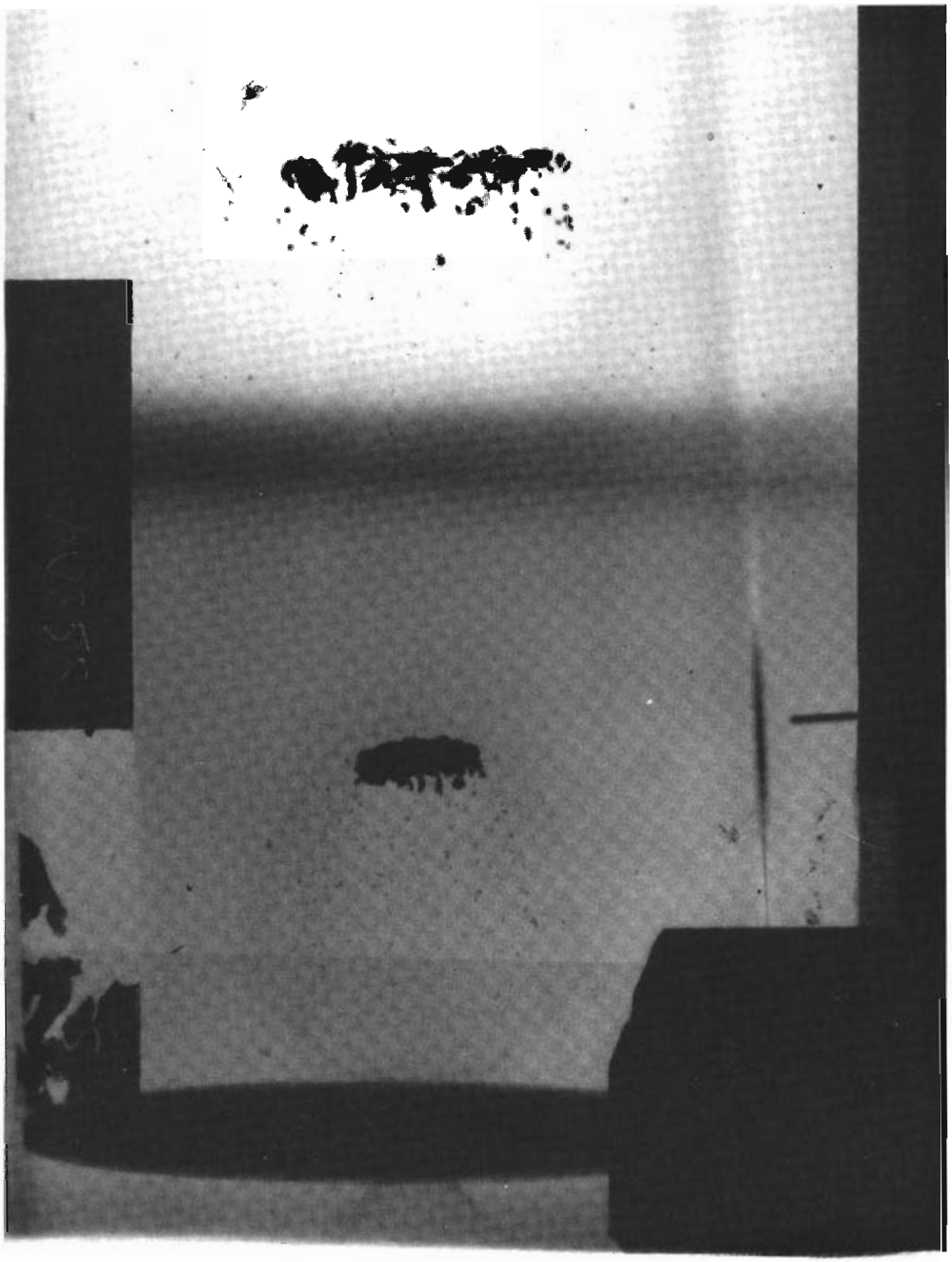

TEST SS-6

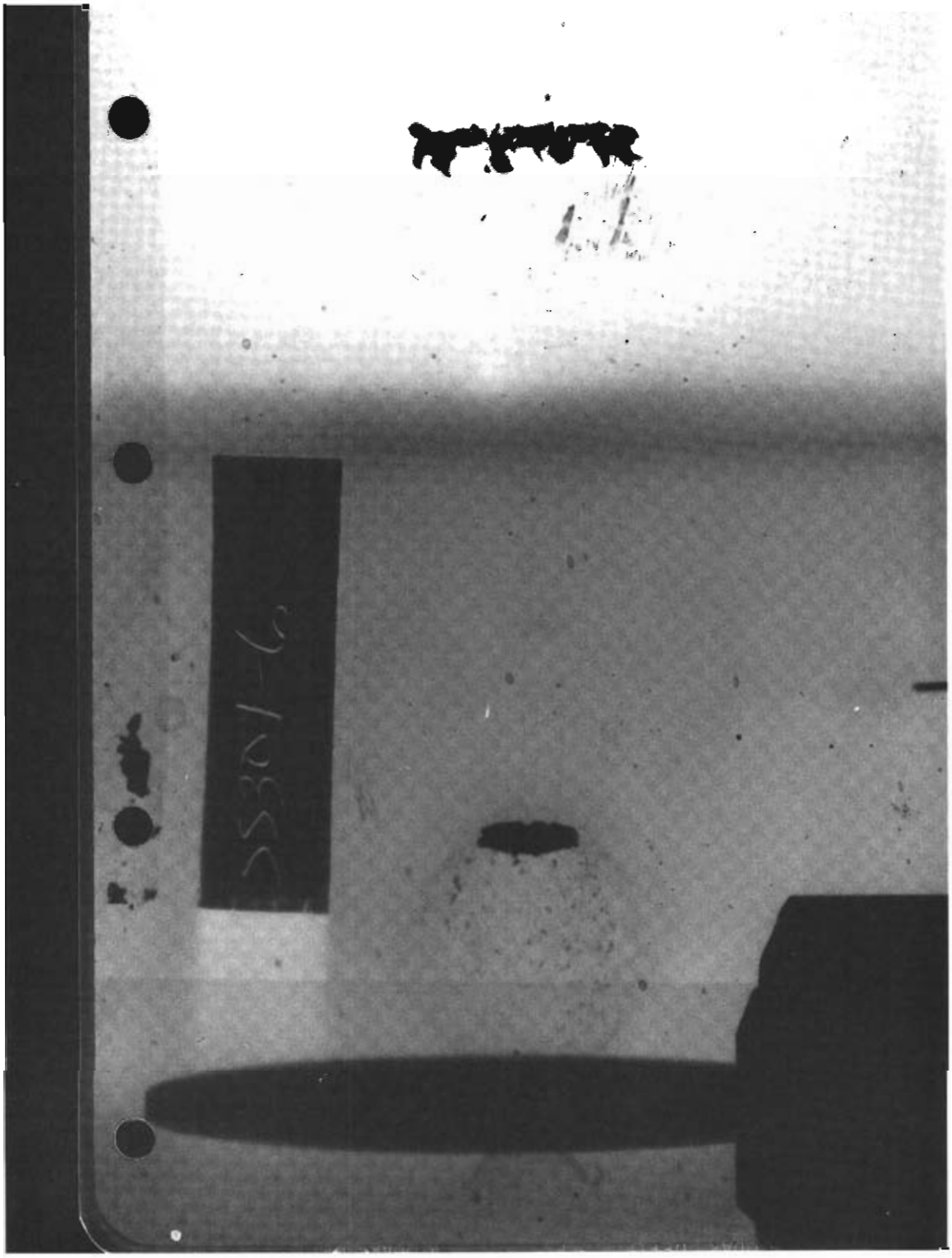

SS - Calibration

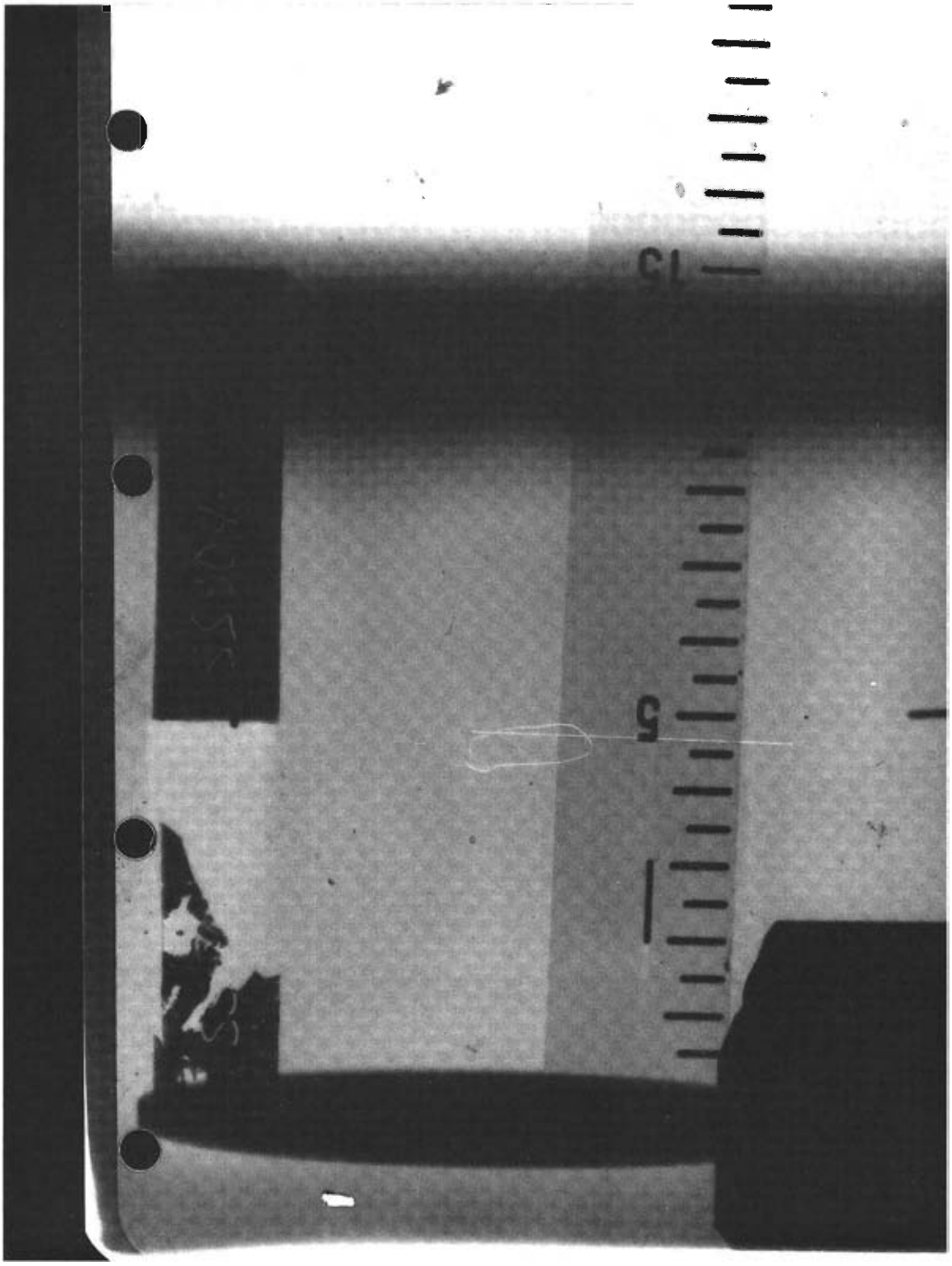

TEST TA-1

TEST TA-3

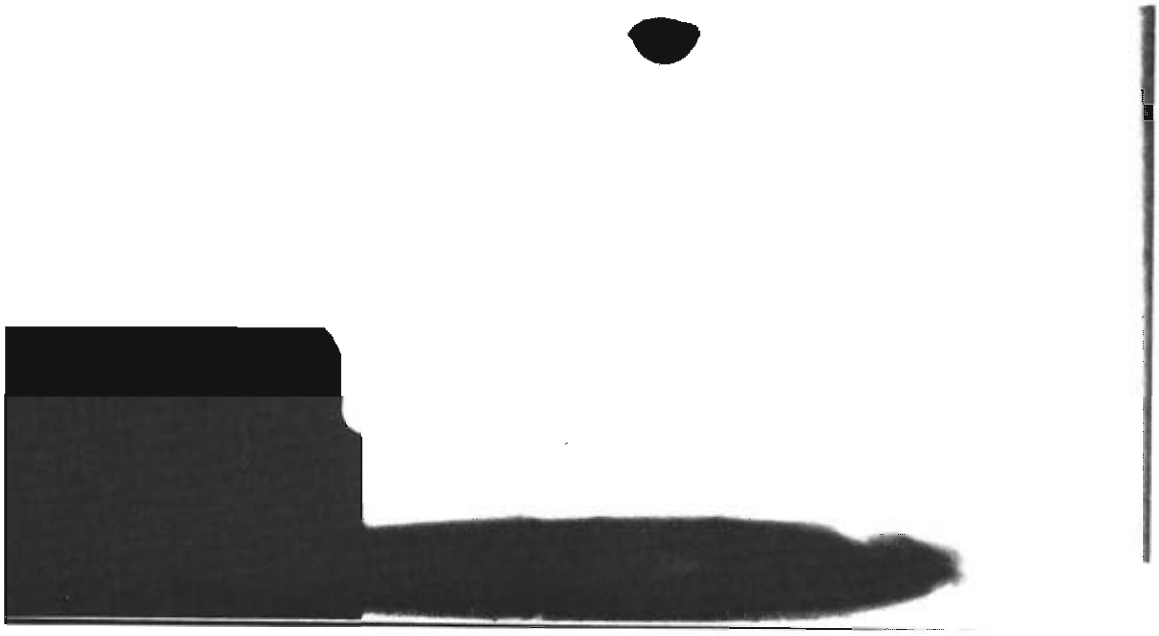

TEST TA-4

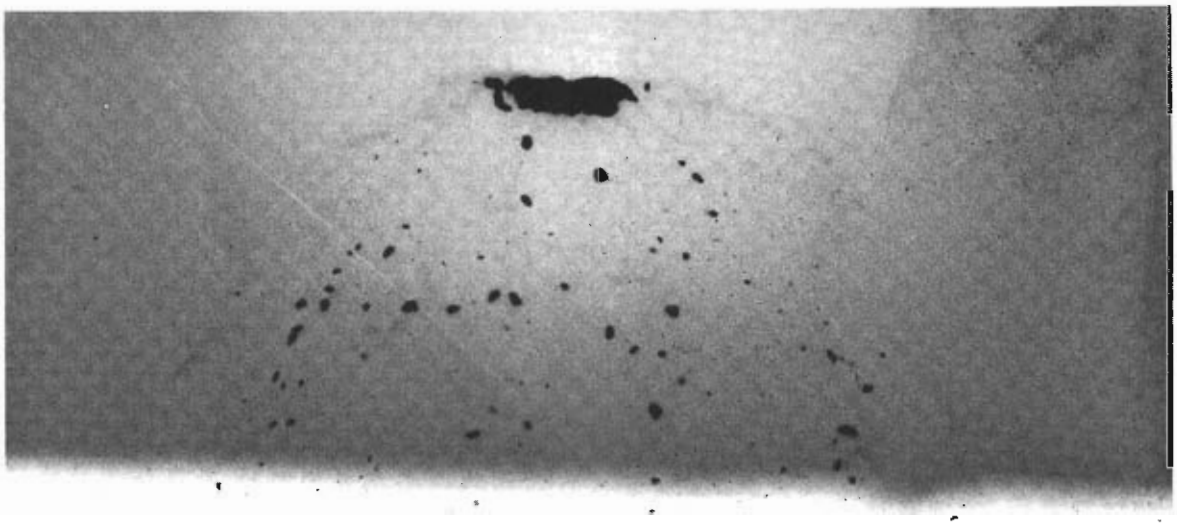

TEST TA-5

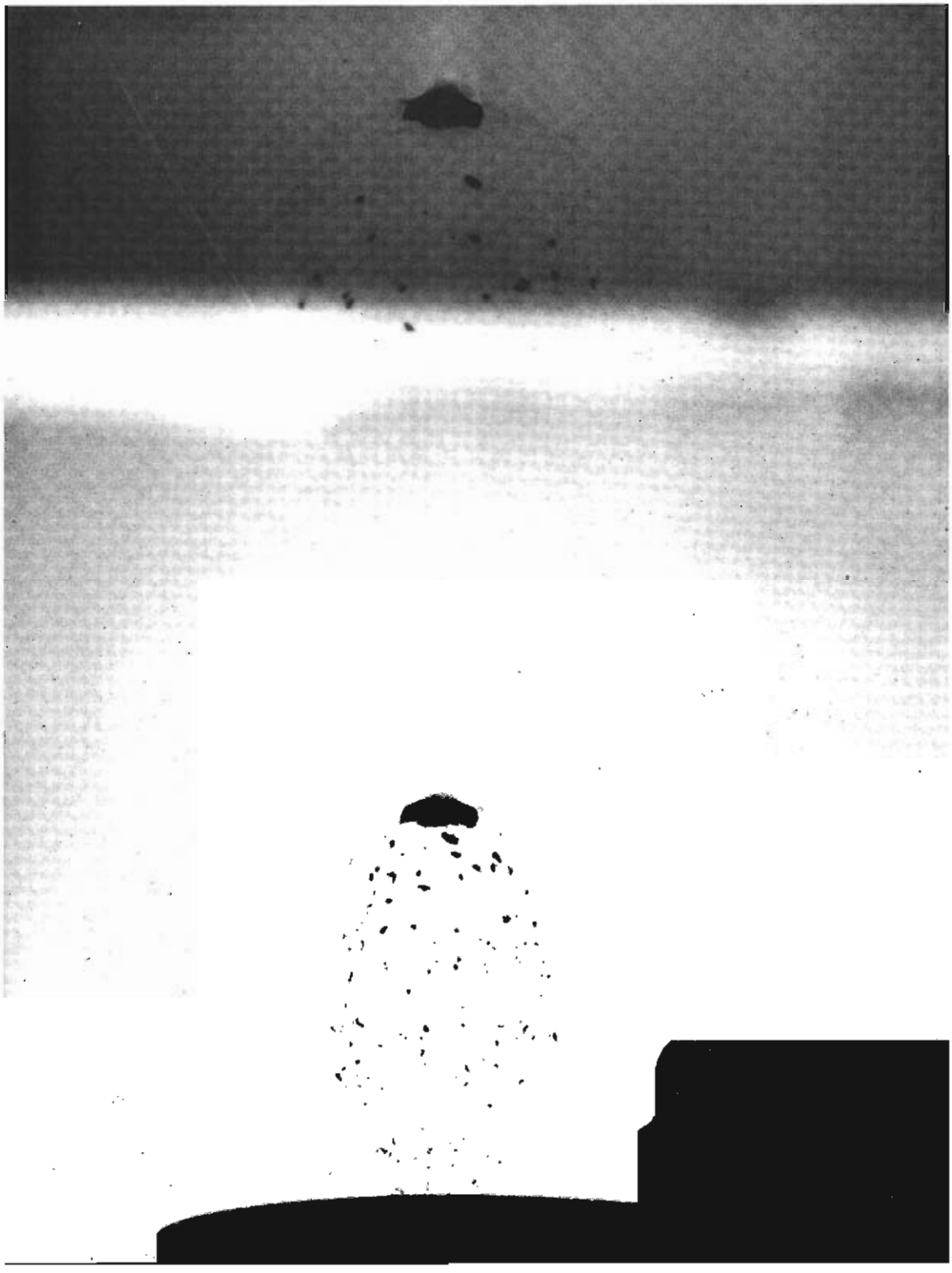

TEST TA-6

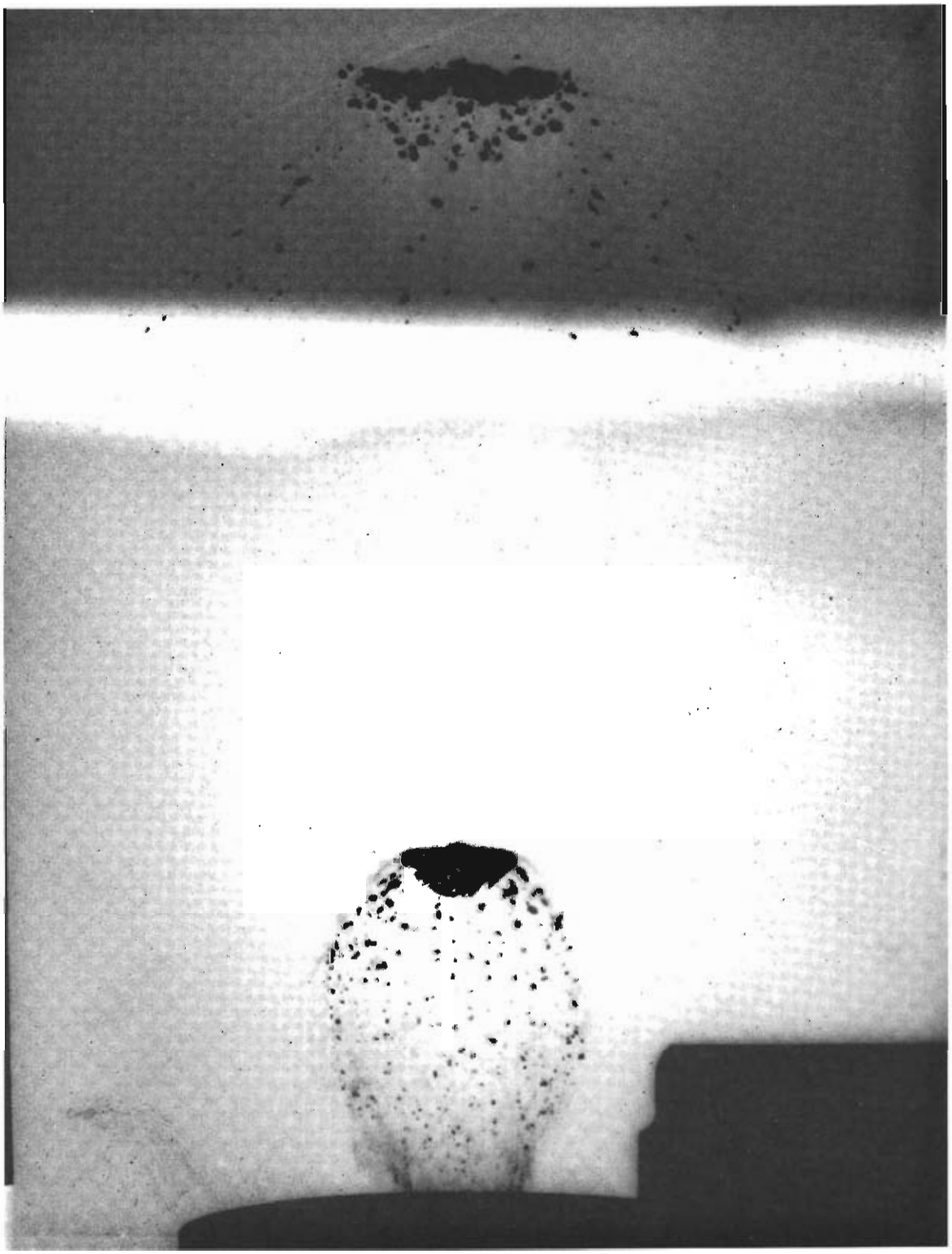

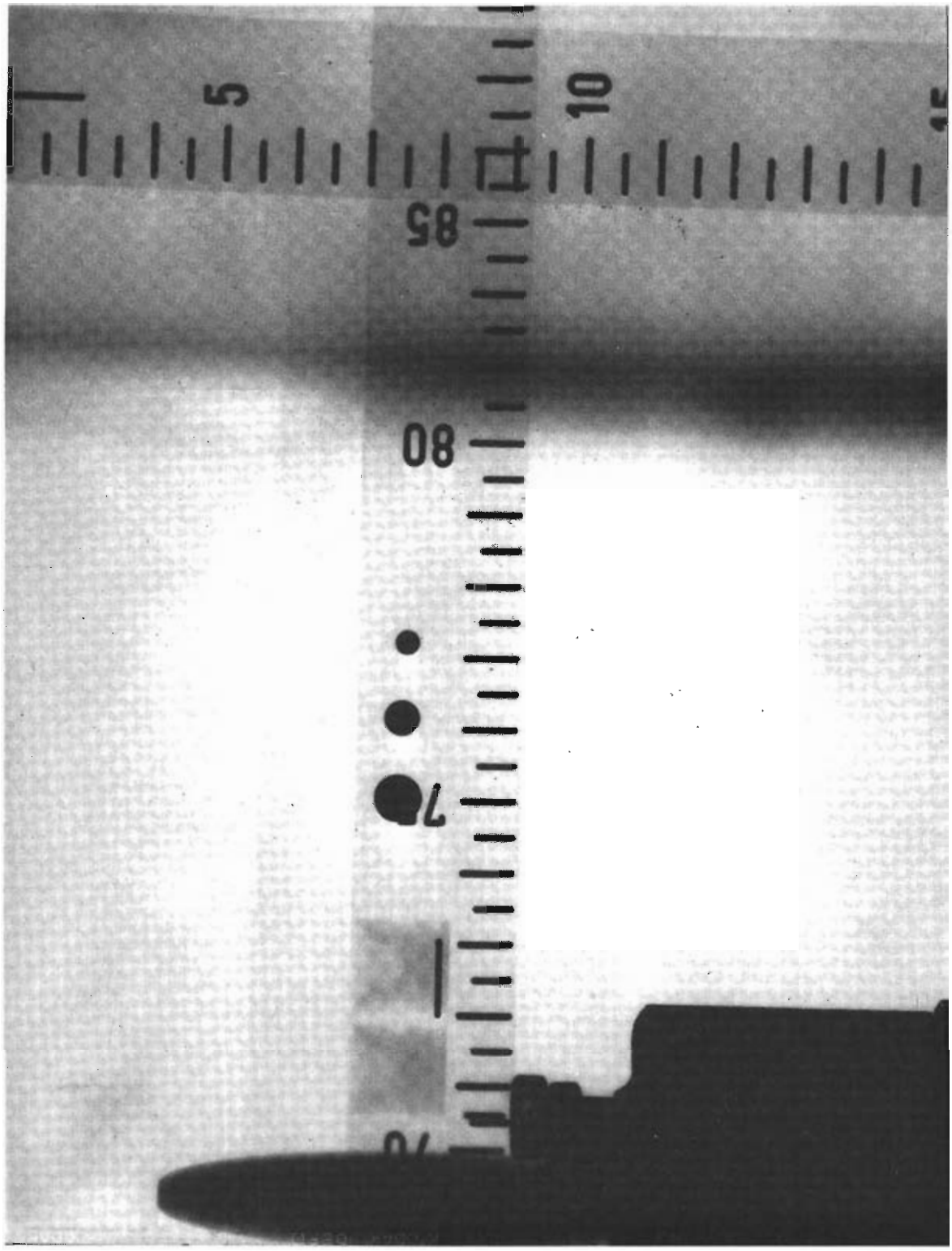
5
10
85
80
75

TEST TI-1

TEST TI-2

TEST TL-3

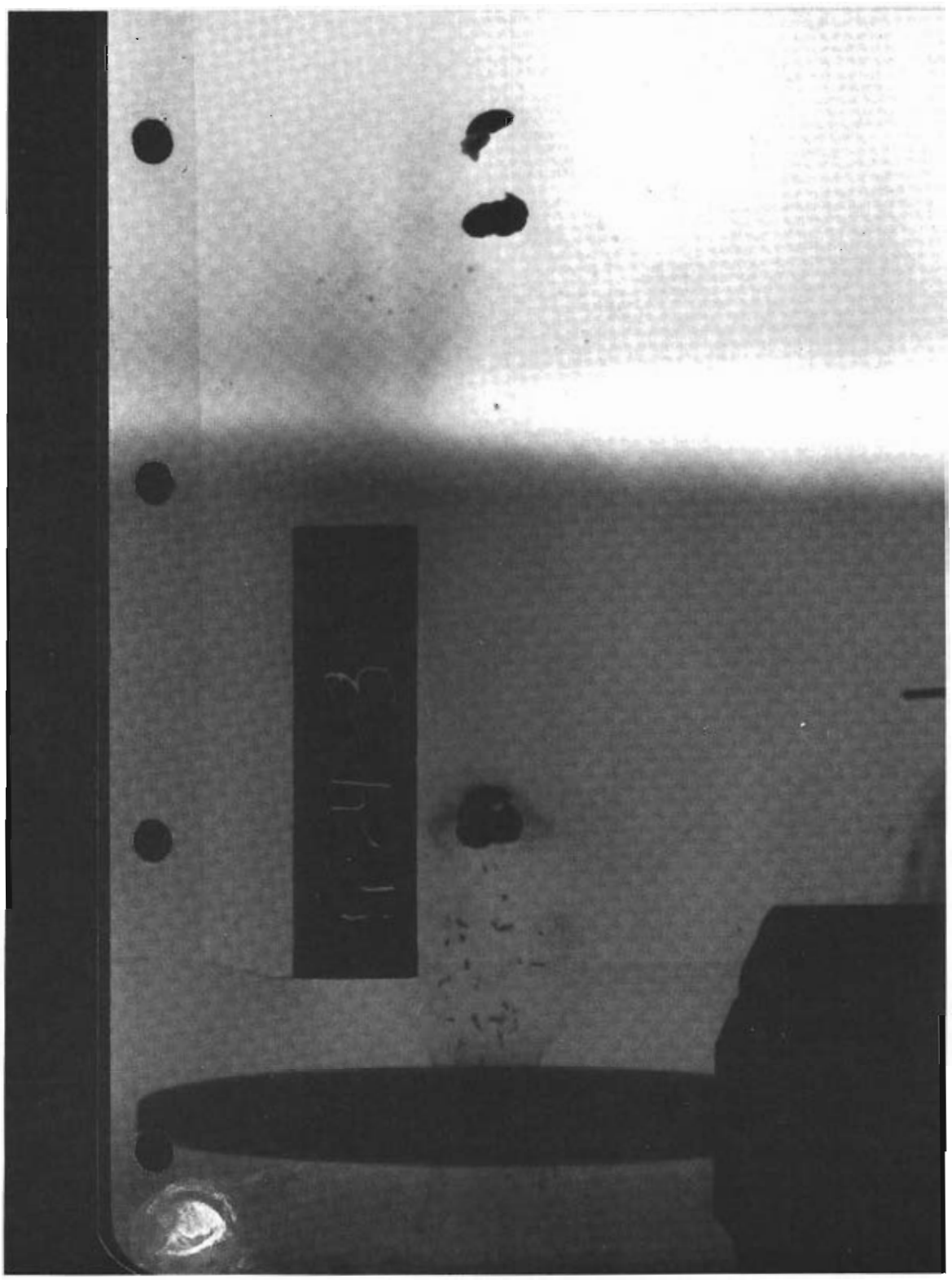

TEST TI-5

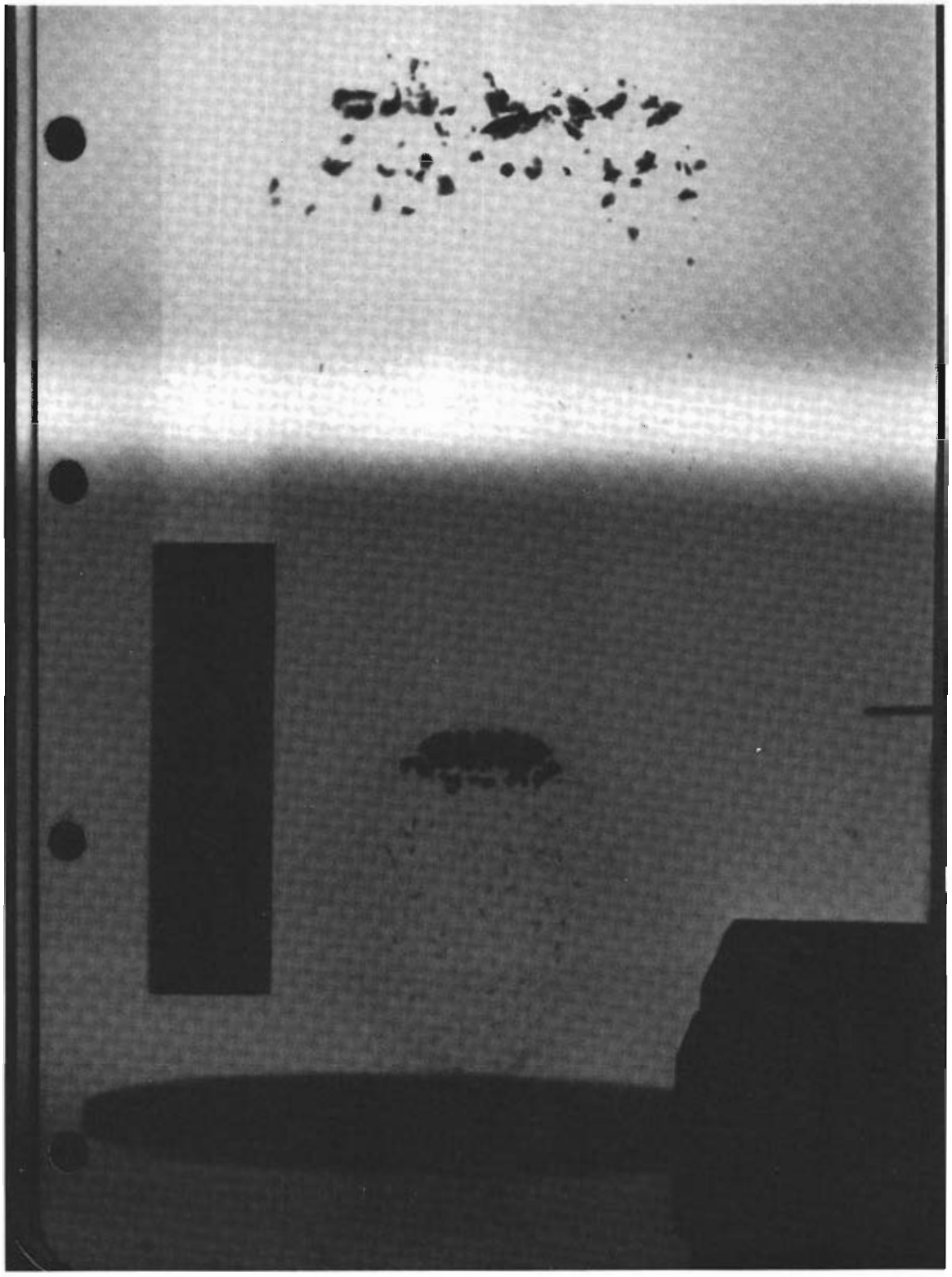

TEST TI-6

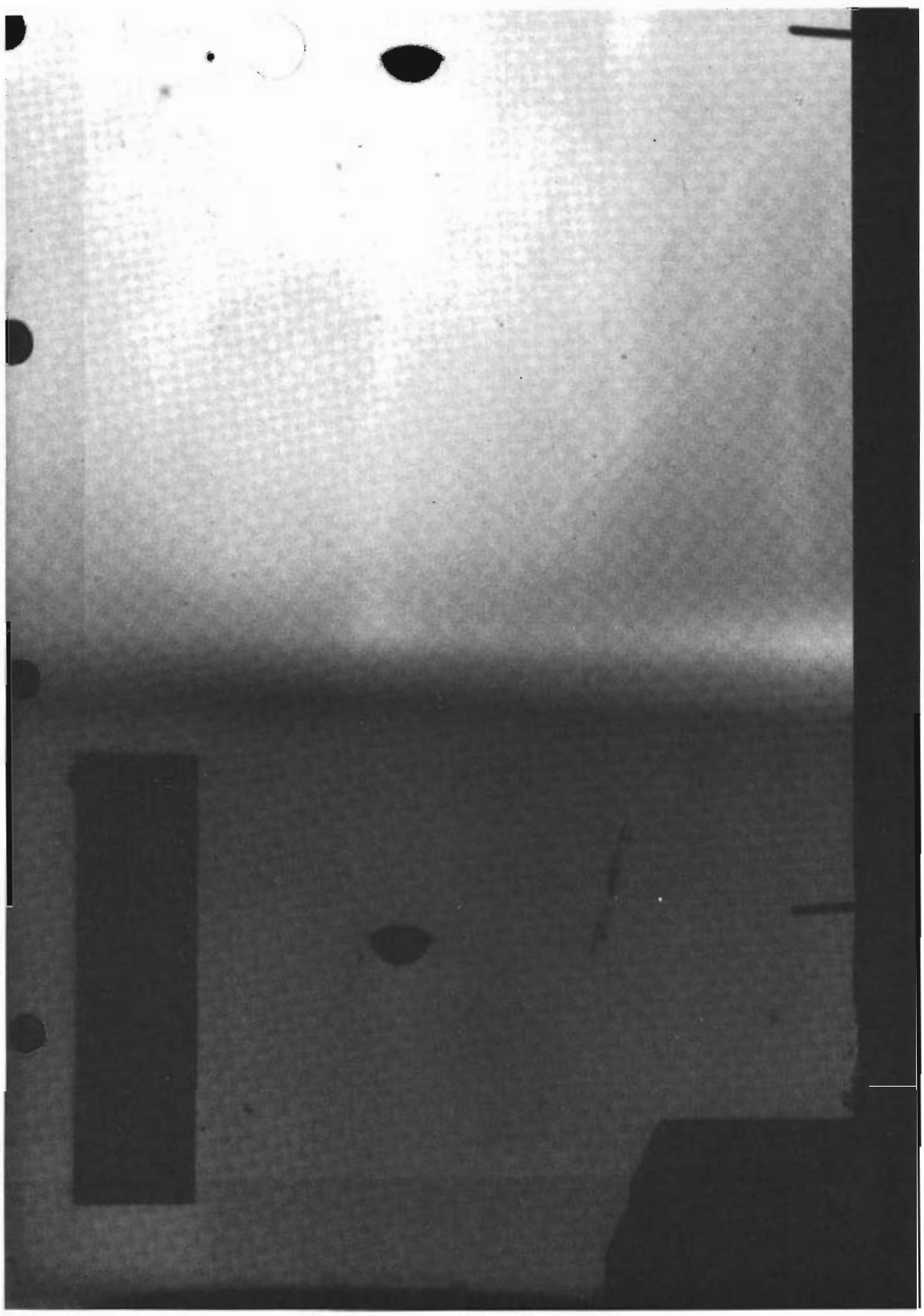

TI - Calibration

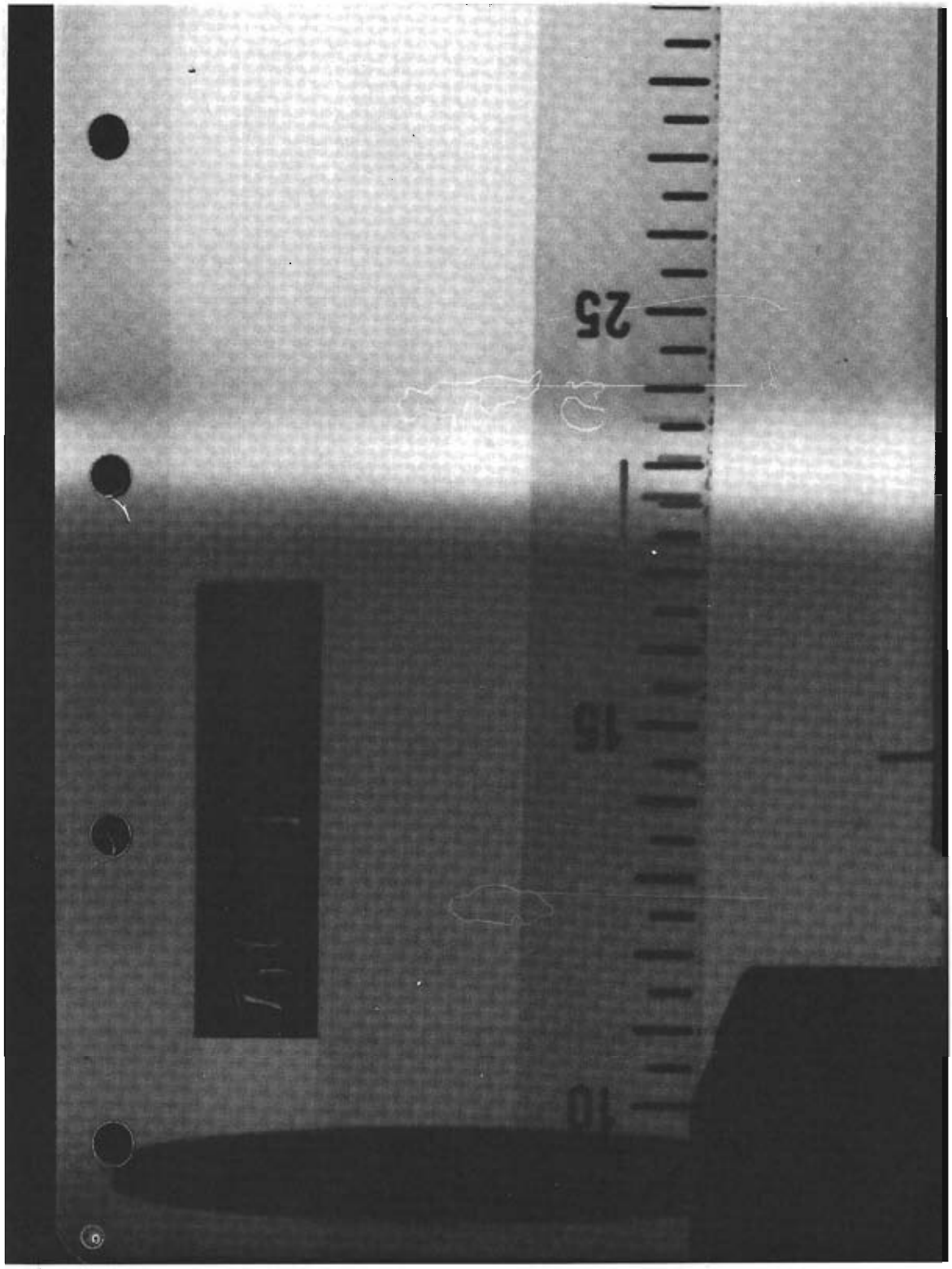

DISTRIBUTION:

INTERNAL

MS 0315 J. Hickerson, 2411
MS 0315 M. J. Forrestal, 2411
MS 0321 W. J. Camp, 9200
MS 0437 J. W. Swegle, 9117
MS 0819 J. S. Peery, 9231
MS 0819 D. E. Carroll, 9231
MS 0819 E. S. Hertel, 9231
MS 0819 T. G. Trucano, 9231
MS 0819 M. K. Wong, 9231
MS 0820 P. Yarrington, 9232
MS 0820 R. M. Brannon, 9232
MS 0820 H. E. Fang, 9232
MS 0820 M. E. Kipp, 9232 (15)
MS 0820 S. A. Silling, 9232
MS 0820 P. A. Taylor, 9232
MS 0820 D. A. Crawford, 9232
MS 0845 J. T. Hitchcock, 2503
MS 1181 J. R. Asay, 9575
MS 1181 L. C. Chhabildas, 9575
MS 1181 C. A. Hall, 9575

MS 0899 Technical Library, 4916 (2)
MS 9018 Central Technical Files, 8940-2
MS 0619 Review and Approval Desk, 12690, For DOE/OSTI (2)

EXTERNAL

T. J. Ahrens
Geophysics Division MS/252-21
California Institute of Technology
Pasadena, CA 91125

F. Allahdadi
Phillips Laboratory
PL/WSSD
Kirtland AFB, NM 87117-6008

M. L. Alme
102 Stevens Forrest Professional Center
9650 Santiago Road
Columbia, MD 21045

C. E. Anderson
Southwest Research Institute
6220 Culebra Road
San Antonio, TX 78284

E. Baker
Army ARDE Center
SMCAR-AEE-WW
Picatinny Arsenal, NJ 07806-5000

D. W. Baum
L-35
Lawrence Livermore National Laboratory
Livermore,CA 94550

D. Belk
U.S. Air Force Armament Laboratory
AD/MNW
Eglin Air Force Base, FL 32542-5434

S. J. Bless
Institute for Advanced Technology
4030-2 W. Braker Lane
Austin, TX 78759-5329

N. Bourne
Cavendish Laboratory
Univ. Cambridge
Madlingley Road
Cambridge CB3 OHE, UK

W. J. Bruchey
Army Research Laboratory
Weapons Technology Directorate
AMSRL-WT
Aberdeen Proving Ground, MD
21005-5066

S. Chou
Army Research Laboratory
AMSRL-MA-F
Aberdeen Proving Ground, MD
21005-5066

E. L. Christiansen
NASA Johnson Space Center
Mail Code SN3
Houston, TX 77058

R. Clifton
Brown University
Division of Engineering
Providence, RI 02912

J. Cogar
Naval Surface Warfare Center
Code G 24
Dahlgren, VA 22448-5000

J. Coltman
Simula Inc.
10016 South 51st Street
Phoenix, AZ 85044

J. L. Crews
NASA Johnson Space Center
Mail Code SN3
Houston, TX 77058

D. Curran
SRI International
333 Ravenswood Avenue
Menlo Park, CA 94025

D. Dandekar
Army Research Laboratory
AMSRL-MA-F
Aberdeen Proving Ground, MD
21005-5066

D. Dickensen
Naval Surface Warfare Center
Code G 24
Dahlgren, VA 22448-5000

J. C. Foster, Jr.
U.S. Air Force Armament Laboratory
AD/MNW
Eglin Air Force Base, FL 32542-5434

K. Frank
Army Research Laboratory
Weapons Technology Directorate
AMSRL-WT-TD
Aberdeen Proving Ground, MD
21005-5066

W. Gillich
Army Research Laboratory
Weapons Technology Directorate
AMSRL-WT-TA
Aberdeen Proving Ground, MD
21005-5066

L. A. Glenn
L-200
University of California
Lawrence Livermore National Laboratory
Livermore, CA 94550

W. Gooch
Army Research Laboratory
Weapons Technology Directorate
AMSRL-WT-TA
Aberdeen Proving Ground, MD
21005-5066

D. E. Grady (15)
Applied Research Associates
4300 San Mateo Blvd. NE
Suite A-220
Albuquerque, NM 87110

Y. Gupta
Washington State University
Department of Physics
Pullman, WA 99163

G. T. Gray
Los Alamos National Laboratory
Los Alamos, NM 87545

W. Hacker
Applied Research Associates
4300 San Mateo Blvd., A-220
Albuquerque, NM 87110

T. Holmquist
Alliant Techsystems, Inc.
7225 Northland Drive
Brooklyn Park, MN 55428

W. Holt
Naval Surface Warfare Center
Code G 24
Dahlgren, VA 22448-5000

Y. Horie
North Carolina State University
Dept. of Civil Engineering
Raleigh, NC 27607

Friedrich Horz
NASA Johnson Space Center
2101 NASA Rd. 1
Houston, TX 77058

K. Iyer
U.S. Army Research Office
P. O. Box 12211
Research Triangle Park, NC 27709

Z. Jaegar
Dept. of Physics
Boston University
590 Commonwealth Ave.
Boston MA 02215

G. Johnson
Alliant Techsystems, Inc.
7225 Northland Drive
Brooklyn Park, MN 55428

J. N. Johnson
Los Alamos National Laboratory
MS B221
Los Alamos, NM 87545

K. Kimsey
Army Research Laboratory
Weapons Technology Directorate
AMSRL-WT
Aberdeen Proving Ground, MD
21005-5066

D. Lassila
L-35
Lawrence Livermore National Laboratory
Livermore,CA 94550

D. Lovelace
Army Missile Command
AMSMI-RD-ST-WF
Redstone Arsenal, AL 35898-5240

F. Maestas
Applied Research Associates
4300 San Mateo Blvd., A-220
Albuquerque, NM 87110

D. Mandell
Los Alamos National Laboratory
MS F663
Los Alamos, NM 87545

H. W. Meyer
Army Research Laboratory
Weapons Technology Directorate
AMSRL-WT-TA
Aberdeen Proving Ground, MD
21005-5066

M. Meyer
Univ. of Calif. at San Diego
Dept. of Applied Mech. & Eng. Sciences
La Jolla, CA 92093

B. Milligan
U.S. Air Force Armament Laboratory
AD/MNW
Eglin Air Force Base, FL 32542-5434

Natalie H. Murray
Shock Physics,
PCS Group
Cavendish Laboratory
Madingley Road
Cambridge
CB3 0HE, U.K.

S. Nemat-Nasser
Univ. of Calif. at San Diego
Dept. of Applied Mech. & Eng. Sciences
La Jolla, CA 92093

T. Nicholas
Air Force Wright Aeronautical Labs.
Air Force Systems Command
Materials Laboratory
Wright-Patterson AFB, OH 45433

Greg Olsen
ED52
Marshall Space Flight Center
AL 35812

Andy Piekutowski
SPC1941
University of Dayton Research Institute
300 College Park Ave.
Dayton, OH 45469-0182

M. Raftenberg
Army Research Laboratory
Weapons Technology Directorate
AMSRL-WT
Aberdeen Proving Ground, MD
21005-5066

P. Randles
DSWA/FCTTS
1680 Texas St. SE
Kirtland AFB, NM 87117-5669

E. Rapacki
Army Research Laboratory
Weapons Technology Directorate
AMSRL-WT-TA
Aberdeen Proving Ground, MD
21005-5066

A. M. Rajendran
Army Research Laboratory
AMSRL-MA-F
Aberdeen Proving Ground, MD
21005-5066

G. Ravichandran
Graduate Aeronautical Laboratories
California Institute of Technology
MS 105-50
Pasadena, CA 91125

M. Scheidler
Army Research Laboratory
Weapons Technology Directorate
AMSRL-WT
Aberdeen Proving Ground, MD
21005-5066

William Schonberg
Civil Engineering Dept.
Univ. Alabama in Huntsville
Huntsville, AL 35899

L. Schwalbe
Los Alamos National Laboratory
MS F663
Los Alamos, NM 87545

Prof. Peter H. Schultz
Brown University
Department of Geological Science
Box 1846
Povidence, RI 02912

S. Segletes
Army Research Laboratory
Weapons Technology Directorate
AMSRL-WT
Aberdeen Proving Ground, MD
21005-5066

J. Thompson
U.S. Army Tank-Automotive Command
AMSTA-RSS
Warren, MI 48397-5000

D. J. Viechniki
Army Research Laboratory
Materials Directorate
AMSRL-MA
Watertown, MA 02172-0001

Joel Williamsen
University of Denver Research Institute
2050 East Iliff Ave.
Denver, CO 80208

L. Wilson
Naval Surface Warfare Center
Code G 22
Dahlgren, VA 22448-5000

N. Winfree
Applied Research Associates
4300 San Mateo Blvd., A-220
Albuquerque, NM 87110

C. Wingate
Los Alamos National Laboratory
MS F663
Los Alamos, NM 87545

T. Wright
Army Research Laboratory
Weapons Technology Directorate
AMSRL-WT
Aberdeen Proving Ground, MD
21005-5066